

Selective laser melting of high-performance titanium alloys: Process, microstructure and properties

by

Xing Zhang

A dissertation submitted to the graduate faculty
in partial fulfillment of the requirements for the degree of

DOCTOR OF PHILOSOPHY

Major: Industrial Engineering

Program of Study Committee:
Yiliang Liao, Major Professor
Hantang Qin
Matthew Frank
Beiwen Li
Shan Jiang

The student author, whose presentation of the scholarship herein was approved by the program of study committee, is solely responsible for the content of this dissertation. The Graduate College will ensure this dissertation is globally accessible and will not permit alterations after a degree is conferred.

Iowa State University

Ames, Iowa

2022

Copyright © Xing Zhang, 2022. All rights reserved.

TABLE OF CONTENTS

	Page
LIST OF FIGURES	iv
LIST OF TABLES	vi
ACKNOWLEDGMENTS	vii
ABSTRACT	viii
CHAPTER 1. GENERAL INTRODUCTION	1
Selective Laser Melting	1
Titanium and Titanium Alloys	3
Pure Ti	3
Alloying elements	4
Alloy classification and applications	5
SLM of Ti Alloys: Microstructure and Properties	7
Microstructure evolution during SLM of Ti alloys	7
Mechanical properties of SLM-produced Ti alloys	9
Motivation	10
Research Objectives	13
Structure of the Dissertation	13
References	14
CHAPTER 2. IN-SITU SYNTHESIS OF Ti_5Si_3 -REINFORCED TITANIUM MATRIX NANOCOMPOSITE BY SELECTIVE LASER MELTING: QUASI-CONTINUOUS REINFORCEMENT NETWORK AND ENHANCED MECHANICAL PERFORMANCE	20
Abstract	20
Introduction	21
Experimental Details	24
Materials preparation	24
SLM process	24
Microstructure characterization	24
Mechanical properties testing	25
Results	26
Parametric study of SLM	26
Microstructural analysis and phase identification	27
Mechanical properties	34
Discussion	39
Formation of quasi-continuous network	39
Strengthening mechanism	42
Conclusion	44
References	46

CHAPTER 3. SELECTIVE LASER MELTING OF GRAPHENE OXIDE-REINFORCED TI-48AL-2CR-2NB: IMPROVED MANUFACTURABILITY AND MECHANICAL STRENGTH.....	51
Abstract.....	51
Introduction	51
Methods	54
Fabrication of GO/Ti-4822 mixed powders	54
SLM process.....	54
Microstructure characterization and hardness tests.....	55
Results and Discussion	55
Characterization of the powders.....	55
Improved manufacturability	56
Enhanced mechanical strength	60
Conclusion	65
References	65
 CHAPTER 4. UNRAVELLING THE HETEROGENEITIES IN SUB-GRAIN CELLULAR STRUCTURE AND MICROMECHANICAL RESPONSE OF SELECTIVE LASER MELTED TI-NB ALLOYS: AN INTEGRATED EXPERIMENTAL AND COMPUTATIONAL INVESTIGATION	 69
Abstract.....	69
Introduction	70
Experimental procedure.....	72
Computational Framework	73
Thermal modeling for solidification conditions.....	74
Phase-field modeling for grain growth.....	76
Crystal plasticity modeling for local mechanical response	78
Results and Discussion	81
Site-specific solidification microstructure.....	81
Heterogeneous microstructure as affected by processing parameters.....	88
Heterogeneity in micromechanical response.....	94
Conclusion	100
Reference	101
 CHAPTER 5. GENERAL CONCLUSION	 106

LIST OF FIGURES

	Page
Figure 1.1: Schematic illustrations of (a) SLM machine and (b) processing parameters.....	2
Figure 1.2: Schematic illustrations of (a) unit cell of α -Ti and (b) unit cell of β -Ti.....	3
Figure 1.3: Categorization of Ti alloys as a function of β stabilizers concentration	5
Figure 1.4: The influence of temperature gradient and solidification velocity on the microstructure evolution during additive manufacturing	8
Figure 1.5: Grain structures of SLM-produced (a) Ti-6Al-4V, (b) Ti-24Nb-4Zr-8Sn and (c) Ti-45Al	9
Figure 2.1: Parametric study of SLM of TMNCs with 5 wt.% nano-SiC	27
Figure 2.2: SEM images showing microstructure of TMNCs fabricated at a moderate energy input of laser power 150 W and scanning velocity 20 mm/s.....	29
Figure 2.3: SEM images showing microstructure of TMNCs fabricated at a high energy input of laser power 200 W and scanning velocity 20 mm/s	30
Figure 2.4: XRD patterns of TMNC-0 and TMNC-5.....	31
Figure 2.5: TEM analysis results	32
Figure 2.6: EBSD analysis results	34
Figure 2.7: Vickers hardness of TMNCs as affected by the amount of nano-SiC.....	36
Figure 2.8: Indentation stress-strain curves of TMNC-0 and TMNC-5.	37
Figure 2.9: Tribological properties of SLM-fabricated TMNCs	38
Figure 2.10: SEM images of worn surfaces.....	39
Figure 2.11: Schematic illustration of mechanism responsible for the formation of quasi- continuous Ti_5Si_3 network.....	40
Figure 3.1: An illustration of adopted zigzag scanning strategy.	55
Figure 3.2: Photograph and images showing the absorption process of GO sheets onto the Ti-4822 powders.....	56

Figure 3.3: BSE images showing the macro-morphologies of the cross-sections in the single-track SLM	58
Figure 3.4: BSE images showing the cross-sections of SLM-fabricated multi-layer samples	60
Figure 3.5: The Vickers hardness values of SLM-fabricated Ti-4822 samples with different wt. % of GO sheets.	61
Figure 3.6: EBSD and BSE images showing the grain and sub-grain refinement	62
Figure 4.1: Schematic illustration of the proposed computational framework.....	74
Figure 4.2: BSE images showing the spatial variations in the solidification microstructure of Ti-35Nb fabricated by SLM.....	82
Figure 4.3: PF modeling of the evolution of sub-grain cellular structure, given a cooling rate of 6.9×10^5 K/s and a temperature gradient of 1.4×10^6 K/m.....	84
Figure 4.4: Modeling of thermal profiles during SLM of Ti-35Nb at a laser power of 210 W and a scanning velocity of 200 mm/s	86
Figure 4.5: The spatial variation in the sub-grain microstructure during SLM of Ti-35Nb with a laser power of 210W and a scanning velocity of 200 mm/s.....	87
Figure 4.6: Melt pool dimensions under four groups of processing parameters	89
Figure 4.7: The calculated site-specific cooling rate V and temperature gradient G as affected by laser processing parameters during SLM of Ti-35Nb	91
Figure 4.8: Variations in the sub-grain size λ across the melt pool under different SLM parameters.....	93
Figure 4.9: Experimental results of microhardness as affected by the sub-grain size.....	95
Figure 4.10: Simulated micromechanical response as affected by the sub-grain size λ	95
Figure 4.11: Micromechanical fields for different sub-grain cellular structures	96
Figure 4.12: Mircorhardness distribution as affected by processing parameters.....	98

LIST OF TABLES

	Page
Table 3.1: The average chemical composition (at.%) of SLM-fabricated 0.3 wt.% GO/Ti-4822 sample at different regions	59
Table 4.1: Material properties and SLM processing parameters for the thermal modeling	76
Table 4.2: Material parameters used for the PF modeling	78
Table 4.3: Calibrated parameters for the CP modeling	81

ACKNOWLEDGMENTS

I would like to express my sincere gratitude to my advisor, Dr. Yiliang Liao, for his patience, support and guidance in my PhD study. His emphasis on scientific knowledge and logical thinking is a great help to my research and even my future career. In addition, I would also like to thank him for granting me the freedom and financial support on trying different ideas and learning various skills.

I would like to acknowledge Dr. Hantang Qin, Dr. Matthew Frank, Dr. Beiwen Li, and Dr. Shan Jiang for serving as my PhD committee members. I really appreciate their valuable inputs in my research.

I want to reserve my deepest thanks to Dr. Yufeng Zheng for his guidance and insightful discussions during my PhD study. I am grateful to the help from his group on the microstructure characterization for my research. My thank also goes to Dr. Leslie Mushongera, who helped me gain the fundamental understanding of solidification process and taught me computational skills for simulating microstructure and mechanical properties for my research.

I wish to express special thanks to Dr. Qiong Nian, Dr. Dong Lin, Dr. Yan Wang, Dr. Pradeep Menezes, for all their guidance and suggestions during our collaborations. I am also grateful to my colleagues and friends for their help and support in my work and life. I must also thank my parents for their support and encouragement in the past five years.

ABSTRACT

Selective laser melting (SLM) of titanium (Ti) alloys has increasingly been used in aerospace and automotive applications. However, current studies have been mainly focused on SLM of α and $\alpha+\beta$ Ti alloys, especially the widely commercialized Ti-6Al-4V. These alloys possess a relatively low hardness, poor wear performance, and insufficient high-temperature stability, restricting their applications in harsh environment. To address these issues, SLM of Ti-based matrix nanocomposite (TMNCs) or new alloys such as γ -TiAl alloys have received considerable attentions in the past few years.

TMNCs reinforced with nano-ceramics such as TiB, TiC, and Ti₅Si₃ are designed to enhance strength, corrosion and wear resistance, and high-temperature durability of Ti alloys. Especially, TMNCs with a quasi-continuous distribution network of nano-Ti₅Si₃ have become one of the most promising high-temperature and wear-resistant material due to the high strength, good high-temperature stability and outstanding oxidation resistance. Nevertheless, manufacturing such TMNCs via SLM has rarely been reported due to the presence of SLM-induced large columnar grains and/or the coarsening of reinforcements. In this study, we propose a nanoparticle-mediated approach to in-situ fabricate such TMNCs by selective laser melting (SLM) of Ti powders and SiC nanoparticles. It is hypothesized that a minor amount of nano-SiC could restrict grain growth during SLM via pinning effect and promote columnar-to-equiaxed grain transition, and contribute to the formation of Ti₅Si₃ network via eutectic reaction. Results show that the desired TMNC can be fabricated with the optimal SiC amount and laser energy input. The microstructure characterization is performed by SEM, EBSD, TEM, and STEM, with a focus on phase constituents and distribution as well as the grain size. The improved mechanical properties of TMNCs are evaluated in terms of surface hardness, indentation properties and wear

performance. The underlying mechanisms responsible for the microstructure evolution and strengthening effect of TMNCs are discussed.

On the other hand, the rapid growth of SLM technique has shed light on new high-performance Ti alloys that cannot be easily fabricated by conventional processes. Particularly, γ -TiAl alloys have gained significant attention as next-generation lightweight materials to replace heavy Ni-/Fe-based superalloys for aircraft engines. However, SLM of γ -TiAl alloys has been suffering from the severe cracking issue, which is ascribed to the spatter formation due to the intensive laser-matter interaction, poor room-temperature ductility of intermetallic alloys, and the large thermal residual stress due to the rapid cooling during SLM. In this study, we propose a facile and effective manufacturing strategy to fabricate crack-sensitive γ -TiAl alloys by SLM. This strategy introduces tough graphene oxide sheets onto the metal powder surface via the electrostatic attraction, which is expected to reduce SLM-induced defects by alleviating the spattering phenomenon during SLM and refining microstructure. The investigation is conducted with a focus on the effects of laser power and GO amount on the macromorphology of single-track processing. The microstructure characterization is performed by BSE and EBSD, showing that crack-free γ -TiAl alloy with refined grain structure can be successfully fabricated. The enhanced surface strength as affected by the amount of GO is evaluated and the strengthening mechanism is proposed.

Moreover, to facilitate the development of new Ti-based alloys for SLM, it is of specific importance to understand the process-microstate-property relationship. Previous efforts have been mainly focused on understanding SLM processing at the grain scale with a homogenous microstructure. However, SLM-produced parts are often consisted of hierarchical and heterogenous microstructure. In this study, we reveal the underlying mechanism responsible for

the heterogeneous sub-grain microstructure and associated micromechanical response via a novel computational framework. Such multi-scale multi-physics framework integrates a finite element thermal model, a phase-field grain growth model and a crystal plasticity micromechanical model. The results demonstrate the effects of process-induced thermal conditions on sub-grain cellular structure and micromechanical response. The heterogeneities within the melt pool are illustrated by the spatial distribution maps of sub-grain size and microhardness. The effectiveness of individual processing parameters on controlling sub-grain microstructure and micromechanical response are also evaluated.

CHAPTER 1. GENERAL INTRODUCTION

Selective Laser Melting

Selective laser melting (SLM) is an additive manufacturing (AM, also known as 3D printing) technology initially developed at the Fraunhofer Institute ILT in Aachen, Germany, for fabricating metal components from metallic powders. It is a powder bed fusion process that employs a high-energy laser beam to melt powder materials together and fabricate 3D solid parts layer by layer [1, 2]. SLM process starts with generating a computer-aided design (CAD) model that describes the geometrical features of the part. Subsequently, the 3D model is sliced into a stack of 2D layers by software, such as Magics, and loaded into the SLM equipment. At the beginning of the printing process, a thin layer of powder material is delivered onto a substrate via a powder supply system, as shown in Figure 1.1(a). After then, the powder material in a selected area is scanned by a high-energy laser beam and fused together according to the prescribed path from the loaded file. Once the scanning process is finished, the building platform is lowered by one-layer thickness and another thin layer of powder is spread on top of the previously processed layer, followed by laser scanning. By repeating the process for successive layers, the designed part can be fabricated in a layer-by-layer manner [3]. The layer thickness usually ranges from 20 to 100 μm for achieving a balance between fine resolution and good powder flowability. SLM process is usually conducted in a chamber filled with argon or nitrogen to prevent the oxidation of as-print materials. The optimization of SLM process is often achieved by adjusting a few processing parameters, including laser power, scanning velocity, layer thickness, and hatch spacing, as shown in Figure 1.1(b).

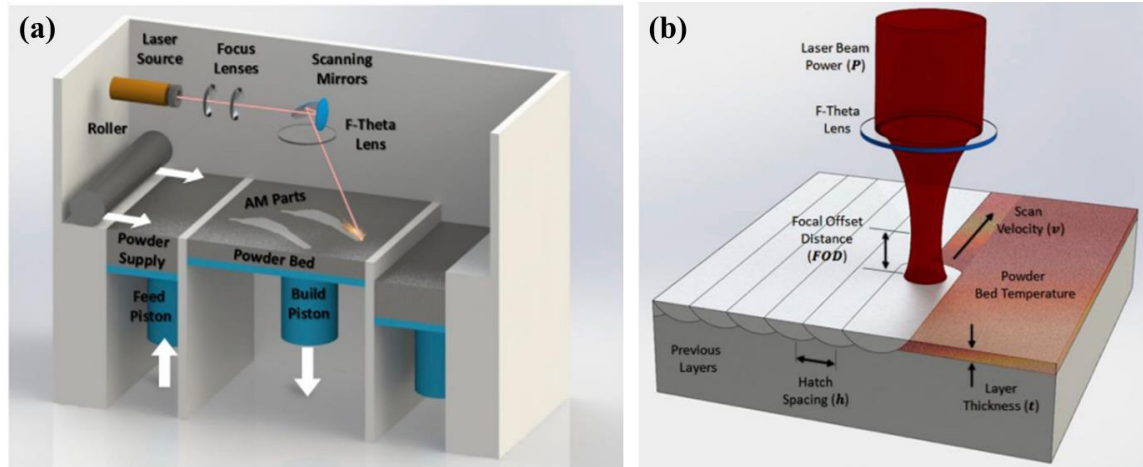


Figure 1.1: Schematic illustrations of (a) SLM machine and (b) processing parameters [3].

Compared to conventional manufacturing methods such as extrusion, forging, and casting, the most significant advantage of SLM is its design freedom that enables the fabrication of components with customized and/or complex geometry. In addition, SLM greatly reduces the lead time from design to testing and needs for assemblies [4]. Moreover, its capability of producing near-net shape components and recycling powders leads to waste minimization, making it cost-effective for certain products. Due to these advantages, there is currently a substantial thrust directed towards the development of SLM-produced components for aerospace, automotive, electronics, and biomedical applications. Wits et al. [5, 6] successfully manufactured a lightweight and high-pressure micropump for small satellite applications. Yakout et al. [6] utilized SLM to produce a 316L stainless steel-based airfoil blade. SLM has also been employed in fabricating electronics including heat sinks, circuit boards, and transparent conductors [7-9]. This technology has also been well adopted in medical fields for fabricating customized bioimplants [10, 11]. In recent years, SLM has also shown great potential in manufacturing novel materials such as functionally-graded materials [12, 13] and metal matrix nanocomposites [14, 15].

Titanium and Titanium Alloys

The element of titanium (Ti) was firstly discovered in 1791, with a density of 4.5 g/cm^3 and a melting point of $1668 \text{ }^\circ\text{C}$. It is the ninth most abundant element in earth's crust and can be alloyed with many other metallic elements (such as Fe, Al, V, Mo, Cr, etc.) to produce strong and lightweight alloys. Generally speaking, Ti alloys possess a high strength-to-weight ratio, good corrosion resistance, good fracture toughness, and excellent biocompatibility [16-18]. Due to these attractive characteristics, Ti alloys have been widely used in aerospace, automotive and bioimplant applications.

Pure Ti

Pure Ti has two allotropic forms, namely α -Ti and β -Ti. Below the β -transus temperature ($882 \text{ }^\circ\text{C}$), Ti presents a hexagonal closest packed (hcp) structured α -phase with lattice parameters of $a = 0.295 \text{ nm}$ and $c = 0.468 \text{ nm}$, as shown in Figure 1.2(a). Above this temperature, Ti presents a body-centered cubic (bcc) structured β -phase with a lattice parameter of $a = 0.332 \text{ nm}$, as shown in Figure 1.2(b) [19, 20].

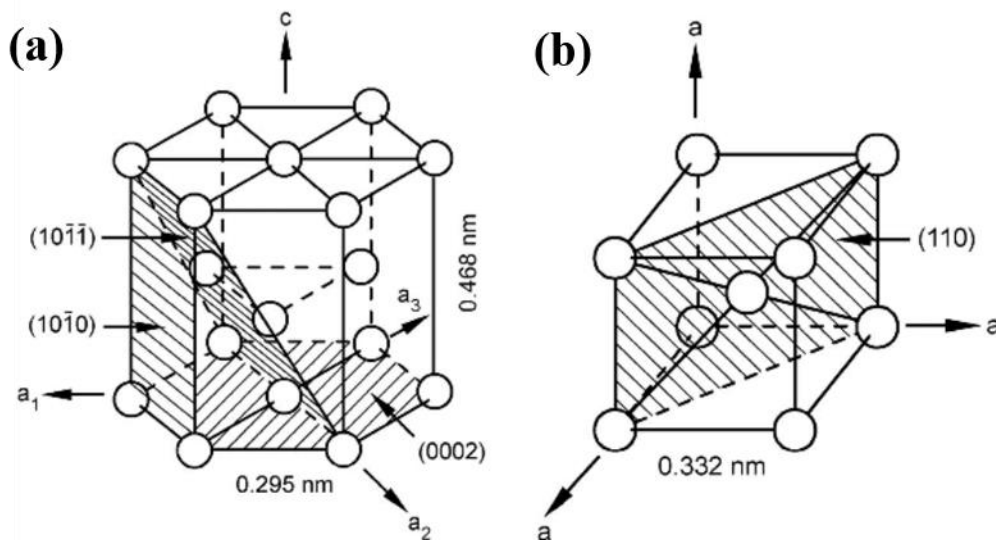


Figure 1.2: Schematic illustrations of (a) unit cell of α -Ti and (b) unit cell of β -Ti [21].

Alloying elements

The alloying elements in Ti alloys can be categorized based on their influences on the β -transus temperature as α stabilizers, β stabilizers, and neutral elements.

α stabilizer

This class of stabilizers is defined as the elements that could increase the β -transus temperature, i.e., increase the tendency of producing hcp α phase at room temperature. α stabilizers include substitutional elements (such as Al, B, Ga, La, Sc, etc.) and interstitial elements (such as C, N, O, etc.). Among various α stabilizers, Al is the most widely used one. In addition, Al equivalency is generally used to compare the effects of different stabilizers in multicomponent systems by:

$$[\text{Al}]_{\text{eq}} = [\text{Al}] + 10[\text{O} + \text{C} + 2\text{N}] + 0.17 [\text{Zr}] + 0.33[\text{Sn}].$$

β stabilizer

This class of stabilizers is defined as the elements that could decrease the β -transus temperature, i.e., increase the tendency of producing bcc β phase at room temperature. β stabilizers include eutectoid elements (such as Fe, Mn, Cr, Ni, Cu, Si, etc.) and isomorphous stabilizers (such as V, Nb, Mo, Ta, etc.). Among these elements, Mo and V are the most widely used ones. In addition, Mo equivalency is generally used to compare the effects of various stabilizers in multicomponent systems by: $[\text{Mo}]_{\text{eq}} = [\text{Mo}] + 0.2[\text{Ta}] + 0.28[\text{Nb}] + 0.4[\text{W}] + 0.67[\text{V}] + 1.25[\text{Cr}] + 1.25[\text{Ni}] + 1.7[\text{Mn}] + 1.7[\text{Co}] + 2.5[\text{Fe}]$.

neutral element

This class of elements, such as Zr and Sn, has a minor effect on the β -transus temperature, but they are commonly used to increase the strength of Ti alloys.

Alloy classification and applications

Depending on the alloying elements, Ti alloys are generally composed of α , $\alpha+\beta$, or β equilibrium phase. Thus, Ti alloys are classified according to the concentration of β stabilizers as α , $\alpha+\beta$, metastable β , and stable β alloys, as shown in Figure 1.3 [22, 23].

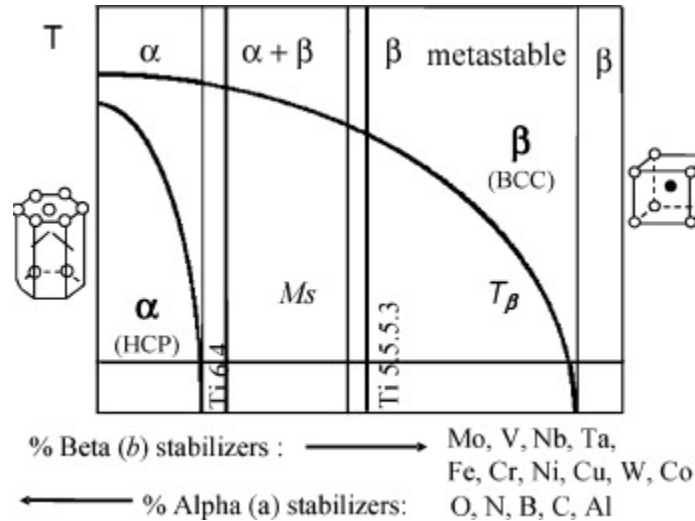


Figure 1.3: Categorization of Ti alloys as a function of β stabilizers concentration [23].

α alloy

This class of alloys contains minor amounts of β stabilizers (< 2 wt.%), leading to the presence of only α phase or the retention of small amounts of β phase (<10 vol.%) at room temperature. α alloys, such as Ti-5Al-2Sn and Ti-8Al-1Mo-1V, generally possess good weldability, high strength, and great creep resistance at an elevated temperature (up to 550 °C), thus have been used for airframe and jet engine parts.

$\alpha+\beta$ alloy

This class of alloys contains moderate amounts of β stabilizers (4 - 6 wt.%), allowing the presence of β phase (10 - 50 vol.%) at room temperature. The resulting $\alpha+\beta$ microstructure can be tuned by heat treatment or thermo-mechanical processing to obtain desired mechanical properties. $\alpha+\beta$ alloys exhibit good formability, high fracture toughness at room temperature, and

moderate strength at an elevated temperature, thus are currently the most widely used Ti alloys in structural applications. In particular, Ti-6Al-4V as the most commercialized Ti alloy occupies more than 50% of the global market of Ti products, owing to its well-balanced strength and ductility, excellent corrosion resistance, and superior biocompatibility [24]. Therefore, Ti-6Al-4V has been widely used for aircraft gas turbine disks, airframe structural forgings and fasteners, and bioimplants.

Metastable β alloy

This class of alloys contains high amounts of β stabilizers (10 -15 wt.%), allowing the presence of only metastable β phase at room temperature upon fast cooling. Metastable β alloys exhibit good weldability, great formability, and excellent hardenability. The hardening phenomenon is achieved by the precipitation of α -Ti upon aging treatment, leading to the high strength (>1400MPa) of Ti alloys. Therefore, metastable β alloys, such as Ti-5Al-5Mo-5V-3Cr and Ti-10V-2Fe-3Al, have been used for airframe components and landing gears.

Stable β alloy

This class of alloys contains very high amounts of β stabilizers (~30 wt.%), leading to the formation of only β phase at room temperature. Stable β alloys cannot be aging-hardened and have not been well commercialized yet. However, there is an increasingly interest in fabricating bioimplants with stable β alloys, due to their relatively low Young's modulus.

γ -TiAl alloys

In recent years, a novel class of intermetallic alloys has been developed by alloying Ti with large amount of Al, exhibiting a typical chemical composition of Ti-(42-49)Al-(0.1-10)X (at.%) [25], where X represents strengthening elements, such as Nb, Mo, Si, etc. The Al concentration range is optimized to produce a dual phase structure consisting of α_2 -Ti₃Al and γ -TiAl (Fig 2.2) [26].

This class of alloys, especially Ti-48Al-2Cr-2Nb, has been developed for high-temperature

applications such as lightweight aircraft engines. It has been demonstrated that γ -TiAl alloys exhibit remarkable mechanical properties at elevated temperatures, including high specific strength, high elastic modulus, and excellent creep and oxidation resistance, which are comparable to those of nickel-based superalloys [27, 28].

SLM of Ti Alloys: Microstructure and Properties

The low machinability of Ti alloys inevitably leads to high manufacturing cost, long lead time and severe material waste in traditional manufacturing processes [24]. SLM provides an ideal platform for manufacturing of Ti alloys, as its design and manufacturing freedoms enable the fabrication of near-net shape parts with complex structures. In the past few years, SLM has been successfully used to fabricate Ti-based components with complex geometries and attractive properties [29]. For instance, Titomic company has additively manufactured Ti-based aircraft components, including airframe, fastening and landing gear [30]. EOS has demonstrated the fabrication of combustion chambers and porous bioimplants by SLM of Ti alloys [31]. Beyond that, the recent market predictions show that Ti used in AM field will grow from a market value of \$518 million in 2022 to over \$1 billion by 2026 [32]. The subsections below briefly review the microstructure and mechanical properties of SLM-produced Ti alloys. The effects of post treatments (such as heat treatment and mechanical processing) on the microstructure and properties are not reviewed as those do not fall within the scope of this research.

Microstructure evolution during SLM of Ti alloys

The key microstructural features of SLM-produced parts include grain structures and phases. Generally, the dominate grain structure in the as-print parts is columnar grains formed via epitaxy grain growth along the temperature gradient direction, similar as the traditional welding process [33]. Additionally, these columnar grains may consist of cellular sub-grain structures, resulting from the high temperature gradient and solidification rate as well as

microsegregation of alloying elements, as shown in Figure 1.4 [34]. The phase constituents are highly dependent on the chemical compositions and thermal conditions. Besides the equilibrium α and β phases, owing to the high cooling rate, metastable phases could present in Ti alloys at room temperature via solid-state phase transformations, e.g., $\beta \rightarrow \alpha'$ or α'' martensitic transformation, $\beta \rightarrow w$ shuffle transformation, and $\beta \rightarrow \beta + \beta'$ phase separation.

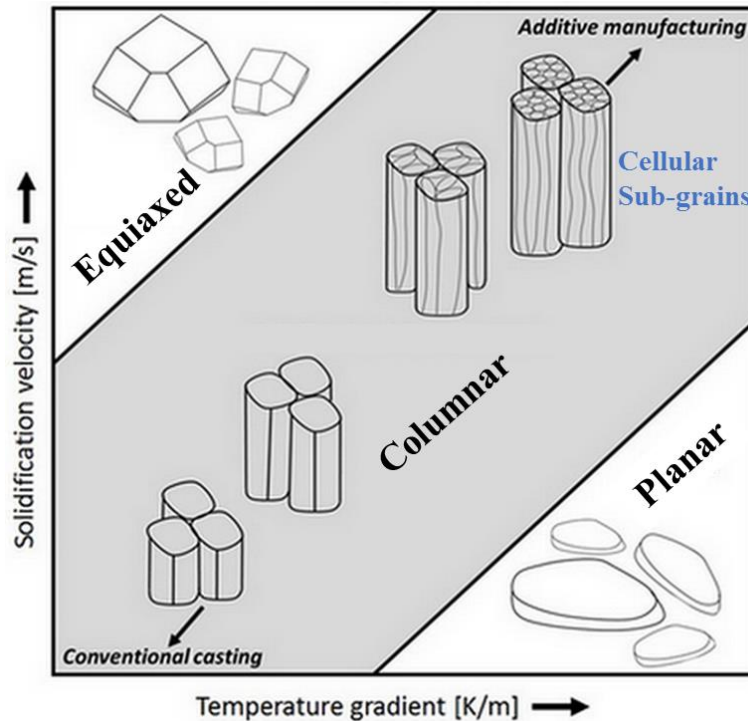


Figure 1.4: The influence of temperature gradient and solidification velocity on the microstructure evolution during additive manufacturing [34].

Current studies have been mainly focused on SLM of pure Ti, α Ti and $\alpha + \beta$ Ti alloys, which exhibit similar microstructure in the as-fabricated parts. Upon solidification, liquid Ti firstly transforms into solid β -Ti phase ($L \rightarrow \beta$), growing along the temperature gradient direction via epitaxial growth and forming large columnar grains. As the temperature continuously decrease to below the β -transus temperature, $\beta \rightarrow \alpha/\alpha'$ phase transformation occurs due to fast cooling. Consequently, acicular α/α' presents a basket-weave pattern inside the large columnar prior- β grains, as shown in Figure 1.5(a) [35]. The morphology, size, and distribution

of acicular α/α' phase are strongly dependent on local thermal conditions. In addition, a few attempts have been carried out to investigate the microstructure evolution during SLM of β Ti alloys, including Ti-24Nb-4Zr-8Sn, Ti-5Al-5Mo-5V-3Cr, Ti-10V-2Fe-3Al, and Ti-Nb alloys. The most typical microstructure is dominated by columnar β grains with cellular sub-grain structure, as shown in Figure 1.5(b) [36]. Metastable phase such as α' , α'' , ω could also be observed, depending on the alloy compositions. Precipitation of α -Ti could occur via in-situ heat treatment due to the repeated thermal cycles. SLM-produced γ -TiAl alloys also exhibit large columnar β grains with cellular sub-grain structure, as shown in Figure 1.5(c) [37]. The general phase transformation path follows $L \rightarrow \beta \rightarrow \alpha \rightarrow \alpha_2 + \gamma$ or $L \rightarrow \beta \rightarrow \alpha_2 + \gamma$. Upon solidification, microsegregation of Al occurs, leading to Al-rich regions within sub-grains and Al-lean regions between sub-grains. Consequently, α_2 -Ti₃Al is often observed inside the sub-grains with supersaturated Al, while γ -TiAl is mainly distributed at the sub-grain boundaries. Thermal cycles during SLM could lead to supersaturated $\alpha_2 \rightarrow \alpha_2 + \gamma$.

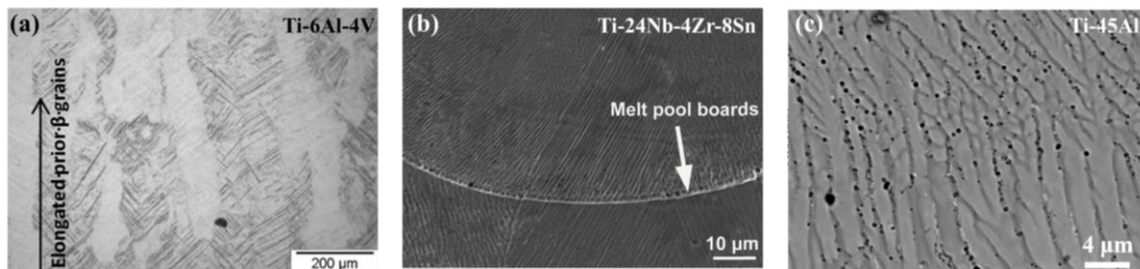


Figure 1.5: Grain structures of SLM-produced (a) Ti-6Al-4V [35], (b) Ti-24Nb-4Zr-8Sn [36] and (c) Ti-45Al [37].

Mechanical properties of SLM-produced Ti alloys

Due to the formation of acicular α/α' phases, SLM-produced pure Ti, α Ti and $\alpha+\beta$ Ti alloys usually present a slight enhancement in strength but a significant drop in ductility, as compared to Ti alloys produced by conventional manufacturing processes. For example, it was reported by Edwards et al. [38] that the SLM-produced Ti-6Al-4V showed an ultimate tensile strength (UTS) of 1035 MPa and an maximum elongation of 3.3%, whereas the wrought Ti-6Al-

4V typically has a UTS of 933 MPa and an maximum elongation of 13% [24]. Post heat treatment is necessary to improve the mechanical properties of as-fabricated parts by reducing or eliminating the acicular phases. In addition, SLM-produced parts exhibit anisotropic mechanical properties due to the presence of columnar grains. In the work of Wysocki et al. [39], it was found that the UTS values of as-fabricated Ti-6Al-4V were 1246 and 1421 MPa along longitudinal and horizontal directions, respectively.

SLM-produced β -Ti alloys generally show relatively low strength (UTS < 1000 MPa) and high ductility, as bcc- β grains dominate the microstructure. For instance, it was reported [40] that SLM-produced Ti-5Al-5Mo-5V-3Cr present an UTS of 800 MPa and a maximum elongation of 14%. For certain β Ti alloys, a higher strength can be obtained by achieving α -Ti precipitation hardening through the aging treatment. The mechanical properties of SLM-produced γ -TiAl alloys have rarely been reported due to its non-printable nature. The existing literatures [41, 42] have demonstrated that it is possible to achieve a high strength comparable to conventional γ -TiAl materials, however, the ductility still needs to be greatly improved.

Motivation

Despite aforementioned research and development efforts in SLM of Ti and its alloys, most existing studies have been devoted to SLM of α and $\alpha+\beta$ Ti alloys, especially the widely used Ti-6Al-4V. These Ti alloys suffer from a few drawbacks, including low hardness, poor tribological performance, and poor high-temperature stability (working temperature < 550°C), which restricts their applications in the harsh environment, especially for aerospace applications. Recent studies have proposed manufacturing strategies of developing nanoparticle-reinforced metal matrix nanocomposites (MMNCs) or new alloy systems, to pursue improved mechanical properties and elevated working temperature of Ti alloys.

Ti-based MMNCs, or TMNCs, reinforced with nano-ceramics (e.g., TiB, TiC, Ti₅Si₃, La₂O₃, etc.) exhibit high specific strength, good corrosion and wear resistance, and high-temperature durability, and thus play an increasingly important role in fabricating structural components under severe friction and heavy loading-conditions [43-45]. Especially, TMNCs with a quasi-continuous distribution network of Ti₅Si₃ have received considerable attention as one of the most promising high-temperature and wear-resistant material due to the high strength, good high-temperature stability and outstanding oxidation resistance [46, 47]. Despite that such TMNCs have been successfully produced by conventional manufacturing process such as casting and sintering, their fabrication by SLM has rarely been reported due to the SLM-induced large columnar grains and/or the reinforcement coarsening. Recent studies [48-50] have shown that TMNCs with Ti₅Si₃ reinforcements can be obtained by the in-situ reaction between Ti and micro-sized SiC (>10 wt.%) during laser processing. Nevertheless, the lack of quasi-continuous network and the formation of micro-scale Ti₅Si₃ and TiC could lead to the extreme brittleness in the as-fabricated composites. Until now, it remains a technical challenge in fabricating TMNCs with quasi-continuously distributed nano-Ti₅Si₃ by SLM, and further investigations are required to elucidate the roles of ceramic additives on the microstructure evolution during SLM of Ti alloys and the corresponding mechanical properties of SLM-fabricated TMNCs.

On the other hand, the development of new Ti-based alloy systems has shed light on AM of high-performance Ti alloys. Particularly, γ -TiAl alloys have received considerable attentions as a promising candidate to replace heavy Ni-/Fe-based superalloys as the next-generation lightweight materials for aircraft components. However, SLM of γ -TiAl alloys has been suffering from the severe cracking issue, which is ascribed to the spatter formation due to the intensive laser-matter interaction, poor room-temperature ductility of intermetallic alloys, and the large

thermal residual stress due to the rapid cooling during SLM. Such cracking issue cannot be simply solved by adjusting SLM processing parameters. To date, a few attempts have been carried out to address this challenge. It has been demonstrated that pre-heating substrates (up to $\sim 800^{\circ}\text{C}$) could benefit the fabrication of crack-free γ -TiAl components by SLM [41, 51].

However, this approach suffers from its high cost, energy-consuming, and safety concerns. In a recent work, it has been proved that the addition of elemental Y could reduce the formation of cracks during SLM of a Ti-43Al-4Nb-1Mo-0.1B (at.%) alloy. Nevertheless, the SLM processing window was greatly narrowed down and several micro-sized pores formed in the as-print parts [52]. Therefore, it is of specific importance to design novel manufacturing strategy for SLM of crack-free γ -TiAl alloys.

For SLM of new Ti-based alloy systems, in addition to the aforementioned manufacturability challenge, experimental trials for alloy design and process optimization are extremely cost- and time-consuming. On the other hand, computational modeling has proved its exceptional capability of bridging the process-microstructure-property relationship. In recent years, numerous modeling strategies, e.g., heat conduction model [53] and computational fluid dynamics (CFD) model [54] for temperature field, cellular automaton (CA) model [55] and phase-field (PF) model [56] for microstructure evolution, crystal plasticity (CP) model [57] and data-driven model [58] for mechanical properties, have been developed to investigate SLM of metallic materials. However, previous efforts have been mostly devoted to understanding SLM processing at the grain scale with a homogenous microstructure. During SLM, the unique sub-grain microstructure also significantly affects mechanical properties of as-fabricated parts including strength, fracture toughness, and fatigue performance. More importantly, the sub-grain microstructural features vary at different locations, leading to the spatial variation in local

micromechanical properties. Such heterogeneities in sub-grain microstructure and micromechanical response can significantly affect the global mechanical performance of as-fabricated components. Currently, a knowledge gap remains in understanding the process-microstructure-property relationship with the consideration of the heterogeneous sub-grain microstructure and micromechanical response in SLM of Ti and its alloys.

Research Objectives

The aim of this study is to open new avenues and provide guidance for fabricating high-performance Ti alloys by SLM. As motivated by aforementioned challenges, several research objectives are proposed below: (a) to fabricate ultrahigh-strength TMNC with a novel quasi-continuous nano-Ti₅Si₃ network architecture and advance the understanding in the role of nano-additives during SLM; (b) to overcome the existing limit in SLM of non-printable γ -TiAl alloys and develop facile and effective manufacturing strategy in fabricating crack-free γ -TiAl alloys by SLM; (c) to reveal the fundamental mechanisms responsible for the heterogeneities in the sub-grain microstructure and micromechanical properties and establish site-specific process-microstructure-property relationship for SLM-produced Ti alloys. These objectives contribute to the AM process/alloy design for successfully fabricating TMNCs and γ -TiAl alloys with desired microstructures and properties towards harsh environmental applications. The knowledge gained in this study, such as the effect of nano-additives on microstructure/properties and the formation principle of heterogenous microstructure, will be applicable to a wide variety of high-performance AM-produced alloys and will benefit the understanding of the effects of hierarchical and heterogeneous microstructure on the global mechanical performance.

Structure of the Dissertation

This dissertation is structured as follows. (1) In Chapter 2, an ultrahigh-strength TMNC coating with Ti₅Si₃ quasi-continuous network is fabricated by SLM, using ball-milled Ti and

nano-sized SiC. The optimal microstructure is obtained by adjusting the weight percentage of SiC and laser energy input. The microstructure characterization and phase identification are performed by scanning electron microscopy (SEM) and transmission electron microscopy (TEM). The ultrahigh mechanical strength is evaluated by surface hardness, nanoindentation properties, and wear performance. (2) In Chapter 3, a manufacturing strategy that introduces graphene oxide onto the metal powder is developed to improve the manufacturability/printability of SLM of a Ti-48Al-2Cr-2Nb alloy. The resulting crack-free microstructure is characterized by backscattered electron (BSE) imaging and electron backscattered diffraction (EBSD). The enhanced mechanical strength is measured and analyzed. (3) In Chapter 4, a computational framework, that integrates a finite element thermal model, a phase-field grain growth model and a crystal plasticity micromechanical model, is proposed to establish the process-microstructure-property relationship at the sub-grain scale for SLM. A Ti-35Nb alloy is used for both modeling and experimental efforts. The mechanisms responsible for the spatial variations in the sub-grain cellular structure and micromechanical response are investigated. The effects of processing parameters on these variations are analyzed. (4) Chapter 5 summarizes this dissertation.

References

- [1] X. Zhang, C.J. Yocom, B. Mao, Y. Liao. Microstructure evolution during selective laser melting of metallic materials: A review. *Journal of Laser Applications*, 31(3), (2019), p. 031201.
- [2] C.Y. Yap, C.K. Chua, Z.L. Dong, Z.H. Liu, D.Q. Zhang, L.E. Loh, S.L. Sing. Review of selective laser melting: Materials and applications. *Applied Physics Reviews*, 2(4), (2015), p. 041101.
- [3] H. Shipley, D. McDonnell, M. Culleton, R. Lupoi, G. O'Donnell, D. Trimble. Optimisation of process parameters to address fundamental challenges during selective laser melting of Ti-6Al-4V: A review. *International Journal of Machine Tools and Manufacture*, (2018),
- [4] E. Yasa. *Selective laser melting: principles and surface quality*. Addit. Manuf., Elsevier (2021), pp. 77-120.

- [5] W.W. Wits, S.J. Weitkamp, J. van Es. Metal additive manufacturing of a high-pressure micro-pump. *Procedia CIRP*, 7, (2013), pp. 252-257.
- [6] M. Yakout, M. Elbestawi, S.C. Veldhuis. On the characterization of stainless steel 316L parts produced by selective laser melting. *The International Journal of Advanced Manufacturing Technology*, (2017), pp. 1-22.
- [7] S. Hou, S. Qi, D.A. Hutt, J.R. Tyrer, M. Mu, Z. Zhou. Three dimensional printed electronic devices realised by selective laser melting of copper/high-density-polyethylene powder mixtures. *Journal of Materials Processing Technology*, 254, (2018), pp. 310-324.
- [8] M. Wong, I. Owen, C.J. Sutcliffe. Pressure loss and heat transfer through heat sinks produced by selective laser melting. *Heat Transfer Engineering*, 30(13), (2009), pp. 1068-1076.
- [9] M. Zenou, O. Ermak, A. Saar, Z. Kotler. Laser sintering of copper nanoparticles. *Journal of Physics D: Applied Physics*, 47(2), (2014), p. 025501.
- [10] T. Hayashi, K. Maekawa, M. Tamura, K. Hanyu. Selective laser sintering method using titanium powder sheet toward fabrication of porous bone substitutes. *JSME International Journal Series A Solid Mechanics and Material Engineering*, 48(4), (2005), pp. 369-375.
- [11] M. Kanazawa, M. Iwaki, S. Minakuchi, N. Nomura. Fabrication of titanium alloy frameworks for complete dentures by selective laser melting. *The Journal of prosthetic dentistry*, 112(6), (2014), pp. 1441-1447.
- [12] V. Beal, P. Erasenthiran, C.H. Ahrens, P. Dickens. Evaluating the use of functionally graded materials inserts produced by selective laser melting on the injection moulding of plastics parts. *Proceedings of the Institution of Mechanical Engineers, Part B: Journal of Engineering Manufacture*, 221(6), (2007), pp. 945-954.
- [13] Z. Liu, D. Zhang, S. Sing, C. Chua, L. Loh. Interfacial characterization of SLM parts in multi-material processing: Metallurgical diffusion between 316L stainless steel and C18400 copper alloy. *Materials Characterization*, 94, (2014), pp. 116-125.
- [14] D. Lin, C.R. Liu, G.J. Cheng. Single-layer graphene oxide reinforced metal matrix composites by laser sintering: Microstructure and mechanical property enhancement. *Acta Materialia*, 80, (2014), pp. 183-193.
- [15] D. Gu, G. Meng, C. Li, W. Meiners, R. Poprawe. Selective laser melting of TiC/Ti bulk nanocomposites: Influence of nanoscale reinforcement. *Scripta Materialia*, 67(2), (2012), pp. 185-188.
- [16] A.K. Das, S.M. Shariff, A.R. Choudhury. Effect of rare earth oxide (Y₂O₃) addition on alloyed layer synthesized on Ti-6Al-4V substrate with Ti+SiC+h-BN mixed precursor by laser surface engineering. *Tribology International*, 95, (2016), pp. 35-43.

- [17] B. Guo, J. Zhou, S. Zhang, H. Zhou, Y. Pu, J. Chen. Phase composition and tribological properties of Ti–Al coatings produced on pure Ti by laser cladding. *Applied Surface Science*, 253(24), (2007), pp. 9301-9310.
- [18] Y. Wang, H. Wang. Wear resistance of laser clad Ti₂Ni₃Si reinforced intermetallic composite coatings on titanium alloy. *Applied Surface Science*, 229(1-4), (2004), pp. 81-86.
- [19] <Characterization of Ti-5553 parts printed by Selective Laser Melting (SLM).pdf>.
- [20] V. Hapon, Y. Teplyk, M. Tuz. ADDITIVE TECHNOLOGY IN AIRCRAFT MANUFACTURING. *Proceedings of National Aviation University*, 84(3), (2020),
- [21] G. L'tjering, J. Williams, *Titanium (engineering materials and processes)*, Berlin: Springer-Verlag Berlin Heidelberg, 2007.
- [22] N. Khanna, R.R. Rashid, S. Palanisamy. Experimental evaluation of the effect of workpiece heat treatments and cutting parameters on the machinability of Ti-10V-2Fe-3Al β titanium alloy using Taguchi's design of experiments. *International Journal of Machining and Machinability of Materials*, 19(4), (2017), pp. 374-393.
- [23] P.-J. Arrazola, A. Garay, L.-M. Iriarte, M. Armendia, S. Marya, F. Le Maître. Machinability of titanium alloys (Ti6Al4V and Ti555. 3). *J. Mater. Process. Technol.*, 209(5), (2009), pp. 2223-2230.
- [24] S. Liu, Y.C. Shin. Additive manufacturing of Ti6Al4V alloy: A review. *Materials & Design*, 164, (2019), p. 107552.
- [25] W. Chen, Z. Li. Additive manufacturing of titanium aluminides. *Additive Manufacturing for the Aerospace Industry*, Elsevier (2019), pp. 235-263.
- [26] F. Iqbal. Fracture Mechanisms of γ -TiAl Alloys Investigated by In-situ Experiments in a Scanning Electron and Atomic Force Microscope. (2012),
- [27] Y.-W. Kim. Intermetallic alloys based on gamma titanium aluminide. *JOM*, 41(7), (1989), pp. 24-30.
- [28] S.J. Qu, S.Q. Tang, A.H. Feng, C. Feng, J. Shen, D.L. Chen. Microstructural evolution and high-temperature oxidation mechanisms of a titanium aluminide based alloy. *Acta Materialia*, 148, (2018), pp. 300-310.
- [29] W. Li, J. Liu, Y. Zhou, S. Wen, Q. Wei, C. Yan, Y. Shi. Effect of substrate preheating on the texture, phase and nanohardness of a Ti–45Al–2Cr–5Nb alloy processed by selective laser melting. *Scripta Materialia*, 118, (2016), pp. 13-18.
- [30] H. Wu, X. Xie, M. Liu, C. Verdy, Y. Zhang, H. Liao, S. Deng. Stable layer-building strategy to enhance cold-spray-based additive manufacturing. *Addit. Manuf.*, 35, (2020), p. 101356.

- [31] M. Salmi, J. Tuomi, K.S. Paloheimo, R. Björkstrand, M. Paloheimo, J. Salo, R. Kontio, K. Mesimäki, A.A. Mäkitie. Patient-specific reconstruction with 3D modeling and DMLS additive manufacturing. *Rapid Prototyping Journal*, (2012),
- [32] S. Publishing, Titanium Opportunities in Additive Manufacturing. https://finance.yahoo.com/news/smartech-publishing-revenues-3d-printed-211425785.html?guccounter=1&guce_referrer=aHR0cHM6Ly93d3cuZ29vZ2xlLmNvbS8&guce_referrer_sig=AQAAAG5nUdnJQUjdyRVAccR7EHZ8XUI6W5IMl6LzZW-a9dRujNp9hB9-rBLqkiIswefxa8traOw9OMdPUeUWRUElmbHMNSYt7JUgGhVwCzuW-ttNYFKYle2e0KccYcnfQTG4esJvYYfbINc8sZ9nG5vf7P0PmXLKYtCQEHDOk5pBxWZL.
- [33] S. David, S. Babu, J. Vitek. Welding: Solidification and microstructure. *JOM Journal of the Minerals, Metals and Materials Society*, 55(6), (2003), pp. 14-20.
- [34] Č. Donik, J. Kraner, I. Paulin, M. Godec. Influence of the energy density for selective laser melting on the microstructure and mechanical properties of stainless steel. *Metals*, 10(7), (2020), p. 919.
- [35] M. Strantza, R. Vafadari, D. De Baere, B. Vrancken, W. Van Paeppegem, I. Vandendael, H. Terryn, P. Guillaume, D. Van Hemelrijck. Fatigue of Ti6Al4V structural health monitoring systems produced by selective laser melting. *Materials*, 9(2), (2016), p. 106.
- [36] Y.J. Liu, S.J. Li, H.L. Wang, W.T. Hou, Y.L. Hao, R. Yang, T.B. Sercombe, L.C. Zhang. Microstructure, defects and mechanical behavior of beta-type titanium porous structures manufactured by electron beam melting and selective laser melting. *Acta Materialia*, 113, (2016), pp. 56-67.
- [37] X. Zhang, B. Mao, L. Mushongera, J. Kundin, Y. Liao. Laser powder bed fusion of titanium aluminides: An investigation on site-specific microstructure evolution mechanism. *Mater. Des.*, 201, (2021), p. 109501.
- [38] P. Edwards, M. Ramulu. Fatigue performance evaluation of selective laser melted Ti-6Al-4V. *Mater. Sci. Eng., A*, 598, (2014), pp. 327-337.
- [39] B. Wysocki, P. Maj, R. Sitek, J. Buhagiar, K. Kurzydłowski, W. Świążkowski. Laser and Electron Beam Additive Manufacturing Methods of Fabricating Titanium Bone Implants. *Applied Sciences*, 7(7), (2017), p. 657.
- [40] H. Schwab, F. Palm, U. Kühn, J. Eckert. Microstructure and mechanical properties of the near-beta titanium alloy Ti-5553 processed by selective laser melting. *Materials & Design*, 105, (2016), pp. 75-80.
- [41] J. Gussone, Y.-C. Hagedorn, H. Gherekhloo, G. Kasperovich, T. Merzouk, J. Hausmann. Microstructure of γ -titanium aluminide processed by selective laser melting at elevated temperatures. *Intermetallics*, 66, (2015), pp. 133-140.

- [42] M. Wang, E. Liu, Y. Du, T. Liu, W. Liao. Cracking mechanism and a novel strategy to eliminate cracks in TiAl alloy additively manufactured by selective laser melting. *Scr. Mater.*, 204, (2021), p. 114151.
- [43] H. Li, Z. Yang, D. Cai, D. Jia, Y. Zhou. Microstructure evolution and mechanical properties of selective laser melted bulk-form titanium matrix nanocomposites with minor B4C additions. *Mater. Des.*, 185, (2020), p. 108245.
- [44] W.H. Yu, S.L. Sing, C.K. Chua, C.N. Kuo, X.L. Tian. Particle-reinforced metal matrix nanocomposites fabricated by selective laser melting: A state of the art review. *Progress in Materials Science*, 104, (2019), pp. 330-379.
- [45] M. Hasan, J. Zhao, Z. Jiang. Micromanufacturing of composite materials: a review. *Int. J. Extreme Manuf.*, 1(1), (2019), p. 012004.
- [46] X. Zhang, M. He, W. Yang, K. Wu, Y. Zhan, F. Song. Structure and mechanical properties of in-situ titanium matrix composites with homogeneous Ti5Si3 equiaxial particle-reinforcements. *Mater. Sci. Eng., A*, 698, (2017), pp. 73-79.
- [47] Y. Jiao, L. Huang, Q. An, S. Jiang, Y. Gao, X. Cui, L. Geng. Effects of Ti5Si3 characteristics adjustment on microstructure and tensile properties of in-situ (Ti5Si3+ TiBw)/Ti6Al4V composites with two-scale network architecture. *Mater. Sci. Eng., A*, 673, (2016), pp. 595-605.
- [48] N. Li, Y. Xiong, H. Xiong, G. Shi, J. Blackburn, W. Liu, R. Qin. Microstructure, formation mechanism and property characterization of Ti + SiC laser clad coatings on Ti6Al4V alloy. *Materials Characterization*, 148, (2019), pp. 43-51.
- [49] M. Das, V.K. Balla, D. Basu, S. Bose, A. Bandyopadhyay. Laser processing of SiC-particle-reinforced coating on titanium. *Scripta Materialia*, 63(4), (2010), pp. 438-441.
- [50] Y.-C. Lin, Y.-C. Lin. Microstructure and tribological performance of Ti–6Al–4V cladding with SiC powder. *Surface and Coatings Technology*, 205(23-24), (2011), pp. 5400-5405.
- [51] L. Caprio, A.G. Demir, G. Chiari, B. Previtali. Defect-free laser powder bed fusion of Ti–48Al–2Cr–2Nb with a high temperature inductive preheating system. *Journal of Physics: Photonics*, 2(2), (2020), p. 024001.
- [52] P. Gao, Z. Wang. Formability improvement, cracking behavior and control of Y-modified Ti–43Al–4Nb–1Mo–0.1 B alloys produced by selective laser melting. *J. Alloys Compd.*, 854, (2021), p. 157172.
- [53] X. Zhang, Y. Liao. A phase-field model for solid-state selective laser sintering of metallic materials. *Powder technology*, 339, (2018), pp. 677-685.
- [54] Y. Lee, W. Zhang. Modeling of heat transfer, fluid flow and solidification microstructure of nickel-base superalloy fabricated by laser powder bed fusion. *Addit. Manuf.*, 12, (2016), pp. 178-188.

[55] K. Teferra, D.J. Rowenhorst. Optimizing the cellular automata finite element model for additive manufacturing to simulate large microstructures. *Acta Mater.*, 213, (2021), p. 116930.

[56] R. Geng, J. Du, Z. Wei, N. Ma. Multiscale modelling of microstructure, micro-segregation, and local mechanical properties of Al-Cu alloys in wire and arc additive manufacturing. *Addit. Manuf.*, 36, (2020), p. 101735.

[57] K. Kapoor, Y.S.J. Yoo, T.A. Book, J.P. Kacher, M.D. Sangid. Incorporating grain-level residual stresses and validating a crystal plasticity model of a two-phase Ti-6Al-4 V alloy produced via additive manufacturing. *Journal of the Mechanics and Physics of Solids*, 121, (2018), pp. 447-462.

[58] C. Herriott, A.D. Spear. Predicting microstructure-dependent mechanical properties in additively manufactured metals with machine-and deep-learning methods. *Comput. Mater. Sci.*, 175, (2020), p. 109599.

CHAPTER 2. IN-SITU SYNTHESIS OF Ti_5Si_3 -REINFORCED TITANIUM MATRIX NANOCOMPOSITE BY SELECTIVE LASER MELTING: QUASI-CONTINUOUS REINFORCEMENT NETWORK AND ENHANCED MECHANICAL PERFORMANCE

Xing Zhang¹, Dian Li², Yufeng Zheng², Yiliang Liao¹

¹ Department of Industrial and Manufacturing Systems Engineering, Iowa State University, Ames, IA 50011, USA

² Department of Chemical and Materials Engineering, University of Nevada, Reno, Reno, NV 89557, USA

Modified from a manuscript under review in *Materials & Design**

Abstract

Titanium matrix nanocomposites (TMNCs) with quasi-continuously distributed Ti_5Si_3 reinforcements exhibit high material strength, good chemical/thermal stability, great tribological properties, and high fracture toughness, and therefore have shown great potentials in aerospace and automotive applications. However, fabrication of such TMNCs via advanced additive manufacturing (AM) techniques has rarely been realized due to the presence of AM-induced large columnar grains and the reinforcement coarsening. Here, we report a nanoparticle-mediated approach to in-situ fabricate nano- Ti_5Si_3 reinforced TMNC coatings by selective laser melting (SLM) of Ti powders and SiC nanoparticles. The effects of nano-SiC amount and laser energy input on the microstructure evolution and mechanical properties were investigated. Results showed that with the optimized SiC amount and SLM processing parameters, a quasi-continuous Ti_5Si_3 network can be achieved at the grain boundaries of laser-printed coatings. It was also found that the addition of nano-SiC promoted the columnar-to-equiaxed grain transition and the formation of a grain structure with primary α_p grains and prior- β grains composed of acicular secondary α_s plates. The SLM-fabricated TMNCs with quasi-continuously distributed Ti_5Si_3

* This chapter is currently as work in progress. It may differ in significant ways from the published version.

showed an ultrahigh surface microhardness of 706 VHN, which was 51.5% higher than that of SLM-fabricated SiC-free sample (466 VHN). Spherical nanoindentation results showed that the effective indentation modulus and indentation yield strength were improved by 62.6% and 57.2%, respectively. A more pronounced strain hardening phenomenon was also observed in the optimized TMNCs. The dry sliding tests revealed that the wear rate was reduced by 70%, and the wear mechanism transferred from abrasion to adhesion.

Introduction

Ti-based matrix nanocomposites (TMNCs) reinforced with nano-scale ceramics play an increasingly important role in aerospace, automotive and military applications, due to their high-specific strength, remarkable chemical resistance, good wear resistance and high-temperature durability [1-3]. However, these TMNCs have mostly been fabricated to achieve a homogeneous microstructure with uniformly distributed reinforcements in the matrix, which leads to the significantly reduced fracture toughness and ductility. To overcome this issue, TMNCs with a novel quasi-continuous network distribution of reinforcements have been developed in recent years [4, 5]. Such unique network microstructure is consisted of reinforcement-rich region at the grain boundary that provides an excellent strengthening effect and reinforcement-lean region within the grains that contributes to the ductility of nanocomposites. In the work of Huang et al. [5], it was reported that given the same amount of TiB reinforcements (8.5 vol.%), the Ti composite with a network microstructure showed an ultimate tensile strength (UTS) of 842.3 MPa and a maximum elongation of 11.8%, whereas the one with a uniform microstructure only demonstrated an UTS of 687.9 MPa and a maximum elongation of 2.9%.

To date, several attempts have been made to develop TMNCs with quasi-continuously distributed reinforcements (e.g., TiB, TiC, Ti_5Si_3) via casting and sintering. For instance, Cai et al. [6] successfully fabricated TiB reinforced Ti-6Al-4V (Ti64) by hot isostatic pressing of Ti64

and TiB_2 powders. TMNCs with similar microstructure was also obtained by Morikawa et al. [7] using casting of elemental Ti and B powders. Zhang et al. [8] produced a TMNC with the quasi-continuous Ti_5Si_3 network structure by casting of Ti and Si powders and showed that the yield strength was increased to 860 MPa from 280 MPa (pure Ti). In particular, Ti_5Si_3 -reinforced TMNCs have received considerable attention as one of the most promising high-temperature and wear-resistant material because of the high strength, good high-temperature stability and outstanding oxidation resistance [8]. Jiao et al. [9] demonstrated that the presence of nano- Ti_5Si_3 in the TMNCs resulted in a remarkable improvement of oxidation resistance at 800 °C due to the formation of SiO_2 layer that restrains oxygen from penetrating into matrix. They also found [10] that the service temperature of the composite was increased to 650 °C (770 MPa) as compared to that of commercial Ti64 (550 MPa at 400 °C).

In addition to conventional manufacturing processes, it is of specific importance to fabricate aforementioned TMNCs via additive manufacturing (AM) techniques, since AM offers exceptional freedom and flexibility in geometric shape designs. Selective laser melting (SLM), as an extensively employed metal AM process, has demonstrated its great potential in manufacturing high-performance metal matrix nanocomposites, owing to its flexibility in feedstock and ability to produce complex-shape in a highly efficient way [11-14]. However, the fabrication of TMNCs with a quasi-continuous Ti_5Si_3 network via SLM has rarely been reported and remains an open question. The main challenge here is associated with the large columnar grains in SLM-fabricated Ti alloys, which leads to limited grain boundary area for the network formation. To tackle this challenge, it is necessary to achieve the columnar-to-equiaxed grain transition for refined microstructure. Nevertheless, it is difficult to obtain fine equiaxed grain structure during SLM of Ti alloys by minor Si additions (unlike casting and sintering), as Si has

a moderate grain refining effect for additive manufactured Ti alloys and only reduces the width of columnar grains [15]. A drastically increase in Si addition may provide sufficient grain refining effect and facilitate the columnar-to-equiaxed grain transition during SLM of Ti; however, the excessive Si (in hypereutectic composition range, >8.3 wt.%) could cause the massive formation of micro-scale Ti_5Si_3 phase and diminish of Ti_5Si_3 network, leading to extreme brittleness [16]. Another promising approach to control the solidification microstructure during metal AM is to introduce nano-scale additives, such as TiC and TiB_2 nanoparticles for Al alloys [17, 18] and stainless steel [19, 20]. The presence of nano-additives could refine the microstructure by pinning the advance of solid-liquid interface [21] or promoting the nucleation of new grains [17] during solidification. Thus, we hypothesize that nano-scale Si-containing compounds, especially SiC, could be the ideal additive for the fabrication of quasi-continuous Ti_5Si_3 reinforced TMNCs by SLM due to following reasons: nano-SiC as a high-melting point (~ 2730 °C) ceramic could partially survive the rapid melting process and impede the grain growth upon solidification to form equiaxed grain structure; effective impediment could be achieved by a small amount of nano-SiC, thereby providing limited Si in hypoeutectic composition range; unlike O and N atoms, the C atom from SiC could further strengthen TMNCs by solid solution hardening without introducing the intensive embrittlement [22, 23].

In this work, we report a nanoparticle-mediated approach to in-situ fabricate TMNC coatings with quasi-continuously distributed nano- Ti_5Si_3 network. SLM experiments of Ti powders and SiC nanoparticles on Ti64 substrate were conducted to systematically investigate the influences of nano-SiC amount and SLM processing parameters on the microstructure evolution. The microstructure characterization was performed with a focus on phase constituents and distribution as well as the grain size. The improved mechanical properties of TMNCs,

including micro-hardness, effective indentation modulus and indentation yield strength as well as wear performance, were assessed. The underlying mechanisms responsible for the microstructure evolution and strengthening effect of TMNCs were discussed.

Experimental Details

Materials preparation

The 99% purity Ti powder (US Nano Inc.) with an average particle size of 45 μm and the 99% purity SiC nanoparticle (US Nano Inc.) with an average particle size of 40 nm were used as the raw materials for this study. The Ti powder was mixed with different amounts of nano-SiC using a planetary ball mill (Retsch PM100) at a rotation speed of 200 rpm, ball-to-powder ration of 5:1, and milling time of 4 h. Ethanol was used as a process control agent to prevent cold welding of the powder materials. The uniformly mixed powder with a layer thickness of 200 μm was preset on a commercial Ti64 plate with dimensions of 25 mm \times 15 mm \times 6 mm.

SLM process

The SLM experiments were carried out using an Ytterbium fiber laser (YLR-500, IPG) with a maximal power of 500W and a wavelength of 1070 nm. The laser beam size was adjusted to \sim 200 μm , and Argon was used as the protective gas to prevent the mixed powder from oxidation. Preliminary single-track SLM experiments were conducted to optimize processing parameters of the laser power (125 - 225 W with an interval of 25 W) and the scanning velocity (10 - 30 mm/s with an interval of 10 mm/s). The overlapping ratio was set to be 50% during multi-track experiments. For a comparison, the SLM experiments of pure Ti powder without nano-SiC were carried out.

Microstructure characterization

The as-processed samples were cross-sectioned, polished, and etched with Kroll's reagent (2 ml HF + 4 ml HNO₃ + 94 ml H₂O) for 15 s. Phase constituents of coatings were determined

by a D8 Advance X-ray diffractometer (XRD) with Cu K α radiation at 40 kV and 40 mA. The microstructure of as-etched TMNCs was examined by Leica DM2700 optical microscope (OM) and JEOL JSM-7100FT scanning electron microscope (SEM) under secondary mode.

Backscatter electron (BSE) imaging of TMNCs were examined by Thermo Scientific Scios 2 dual-beam SEM. Energy dispersive spectroscopy (EDS), selected area diffraction pattern (SADP) and dark-field (DF) images were collected using the FEI Talos F200s scanning transmission electron microscope (STEM). Electron backscattered diffraction (EBSD) analysis was performed to reveal the grain structure.

Mechanical properties testing

The hardness testing was conducted using a Wilson Vickers hardness tester at a 500-g load and a 10-s holding time. Spherical nanoindentation testing was carried out on an MTS nanoXP Nano Indenter with continuous stiffness measurement (CSM), using a spherical diamond tip with radius of 31.2 μm . The load rate was set to be a constant value of 0.05 /s to reach a maximum indentation depth of \sim 500 nm. CSM was obtained at a displacement amplitude of 2 nm and frequency of 45 Hz for determining the effective zero-point correction. The wear tests were performed using a ball-on-plate configuration with a Rtec Multi-function tribometer 5000 under ambient condition. The E52100 steel ball (McMaster) with a diameter of 6.35 mm and a Vickers hardness value of 746 VHN was chosen as the counter material. Prior to sliding tests, the surfaces of the samples were ground with sandpaper (up to 1200 grid) to obtain the same surface roughness. The tests were performed at a normal load of 20 N, a reciprocating speed of 5 mm/s, and a sliding distance of 1 m. The wear rate was calculated based on the dimension of wear track. The worn surfaces of different samples were characterized by SEM and EDS.

Results

Parametric study of SLM

Single-track SLM experiments were firstly carried out to determine appropriate SLM processing parameters for fabricating defect-free TMNCs. Our preliminary investigations indicated that severe cracking issues can be found in single-tracks with excessive addition of nano-SiC (> 5 wt.%) for all processing conditions, similar as the work reported in Ref. [24]. Thus, 0 - 5 wt.% was considered as the appropriate range of nano-SiC addition for performing the parametric study and microstructural investigation, as shown in Figures 2.1-2.3. Here, Figure 2.1 presents an example of parametric study showing the cross-sectional morphologies of TMNCs with 5 wt.% nano-SiC processed by single-track SLM with various laser powers and scanning velocities. The results show that, given a low laser energy input (Zone I), the TMNCs exhibit poor quality with a large porosity and zero dilution rate (into the substrate). Given a moderate laser energy input (Zone II), relatively dense tracks with a proper dilution rate can be obtained. In addition, a magnified image [Figure 2.1 (b)] shows that the fabricated TMNCs consist of dark equiaxed grains and bright grains with dendritic or globular morphology. On the other hand, further increasing the laser energy input (Zone III) leads to a higher dilution rate and the formation of structure with alternating bright and dark regions [Figure 2.1 (c)]. In this study, to consider the quality of TMNCs and the microstructural change as affected by laser energy input, two sets of processing parameters were selected, i.e., a moderate energy input of laser power 150 W and scanning velocity 20 mm/s and a high energy input of laser power 200 W and scanning velocity 20 mm/s.

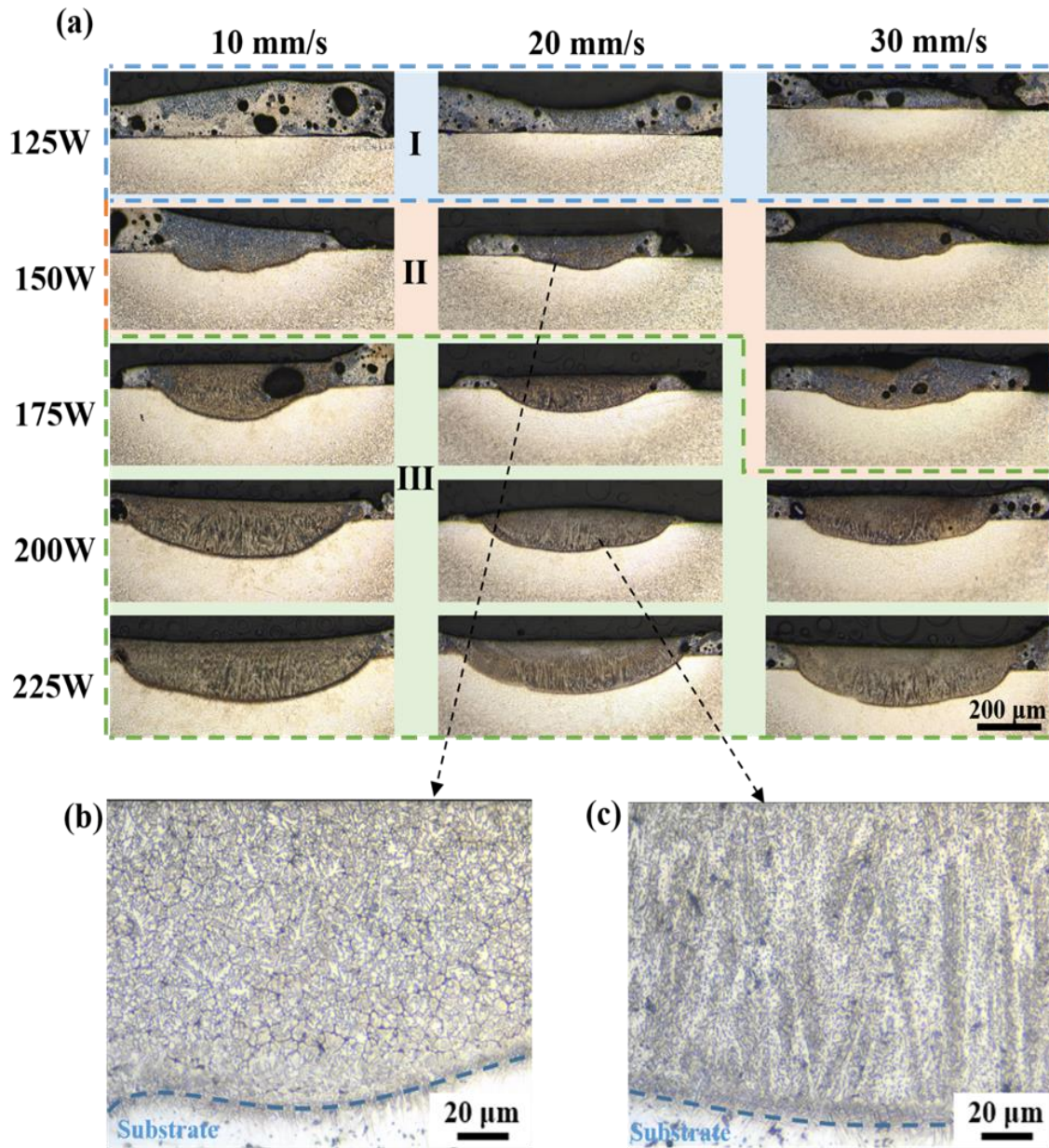


Figure 2.1: Parametric study of SLM of TMNCs with 5 wt.% nano-SiC. (a) Cross-sectional OM images showing morphology and microstructure as affected by laser power input and scanning velocity. High magnification OM images of TMNCs produced at (b) a moderate laser energy input and (c) a high laser energy input.

Microstructural analysis and phase identification

SEM images in Figure 2.2 present the effect of nano-SiC amount (0, 2.5 and 5 wt.%) on the microstructure of SLM-fabricated parts processed at the moderate energy input. The as-fabricated SiC-free sample [Figure 2.2(a) and (b)] depicts a typical microstructure of SLM-

produced Ti parts [25], where large prior- β columnar grains can be observed. In addition, continuous grain boundary α (α_{GB}) can be easily found at the prior- β columnar grain boundaries and acicular α -Ti forms a basketweave structure within the prior- β grains, owing to the ultrafast cooling rate ($10^3 - 10^6$ °C/s) during SLM. By adding 2.5 wt.% nano-SiC [Figure 2.2 (c) and (d)], the as-fabricated material shows similar columnar structure as SLM-fabricated SiC-free sample. However, the grain boundary α becomes discontinuous and difficult to be identified. Additionally, a dendritic structure without acicular α -Ti inside (marked by the blue dashed circle) can be observed. By further increasing the amount of nano-SiC to 5 wt.%, where the columnar grain structure disappears and thin grain boundaries (marked by yellow arrows) showing a network architecture can be found around the refined grains. In addition, two types of grains, namely Type I and Type II, can be observed. Type I grain exhibits dendritic or globular morphology without acicular plates inside; while Type II grain shows a colony structure composed of parallel acicular plates.

On the other hand, the microstructure of as-fabricated TMNCs under the high energy input is present in Figure 2.3. Without nano-SiC addition, the TMNC exhibits an identical microstructure to the one fabricated at a moderate energy input [Figure 2.2(a) and (b)] and thus is not shown below. With the addition of 2.5 wt.% nano-SiC, the as-fabricated TMNC [Figure 2.3(a) and (b)] shows columnar grains with acicular plates in basketweave structure and discontinuous phase at grain boundaries, similar to the sample fabricated at the moderate energy input in Figure 2.2(d). Nevertheless, there is no evidence of the dendritic grains without acicular α -Ti.

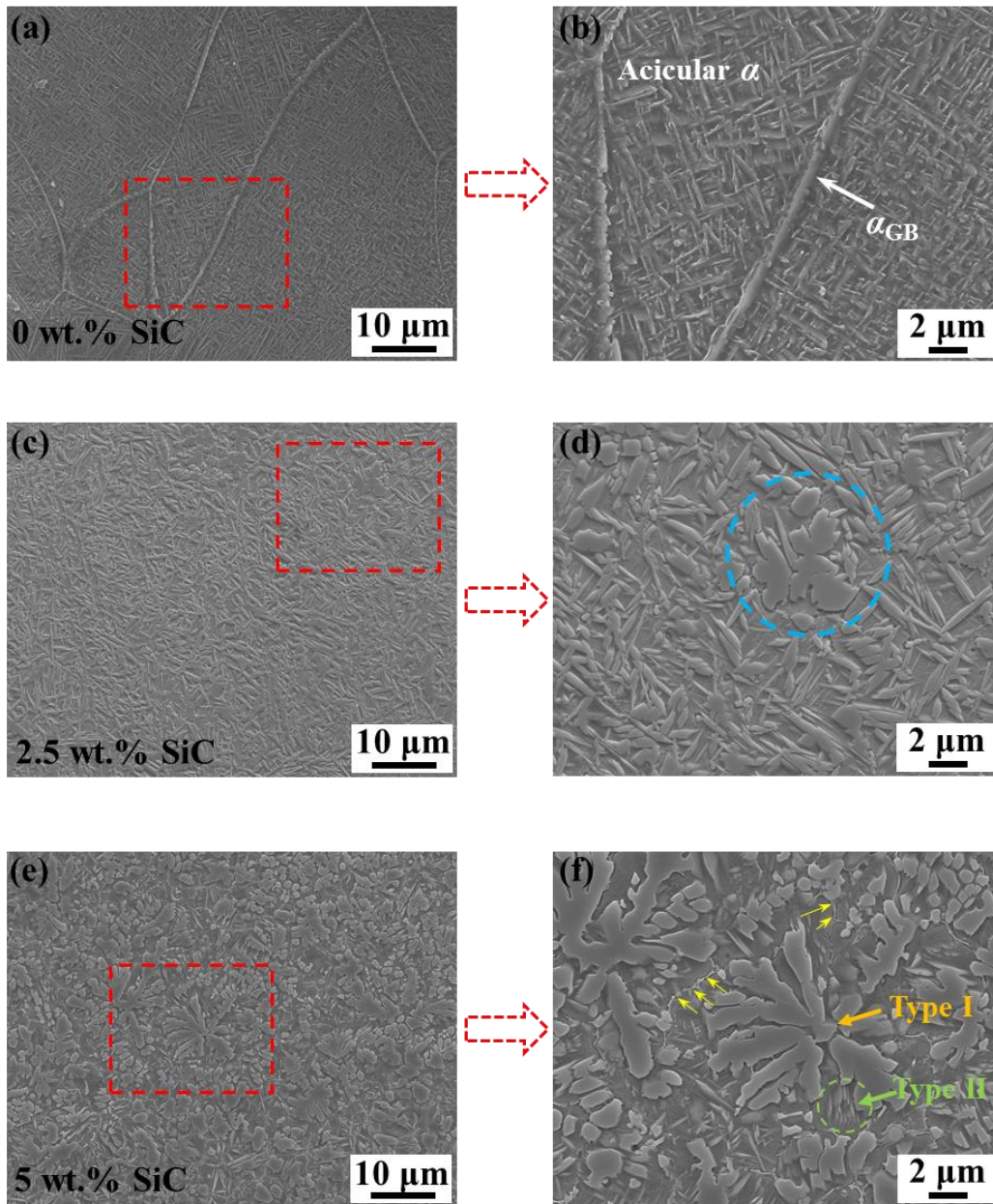


Figure 2.2: SEM images showing microstructure of TMNCs fabricated at a moderate energy input of laser power 150 W and scanning velocity 20 mm/s: (a, b) without nano-SiC, (b, c) with 2.5 wt.% nano-SiC, and (e, f) with 5 wt.% nano-SiC.

By increasing the nano-SiC amount to 5 wt.%, the TMNC [Figure 2.3(c) and (d)] is still dominated by large columnar grains but consisted of alternated regions with different sizes of acicular plates. In comparison to the sample fabricated at the moderate energy shown in Figure 2.2(f), neither the Type I or Type II grains nor the trace of possible network are observed. Based

on the SEM characterization results, it is found that both the nano-SiC amount and the laser energy input play important roles in determining the microstructure of as-fabricated TMNCs. More importantly, for all SLM-fabricated samples, only the TMNC with 5 wt.% nano-SiC addition fabricated at a moderate laser energy input exhibits the desirable network architecture. Here, we denote such sample as TMNC-5 and the SiC-free sample fabricated at a moderate laser energy input as TMNC-0.

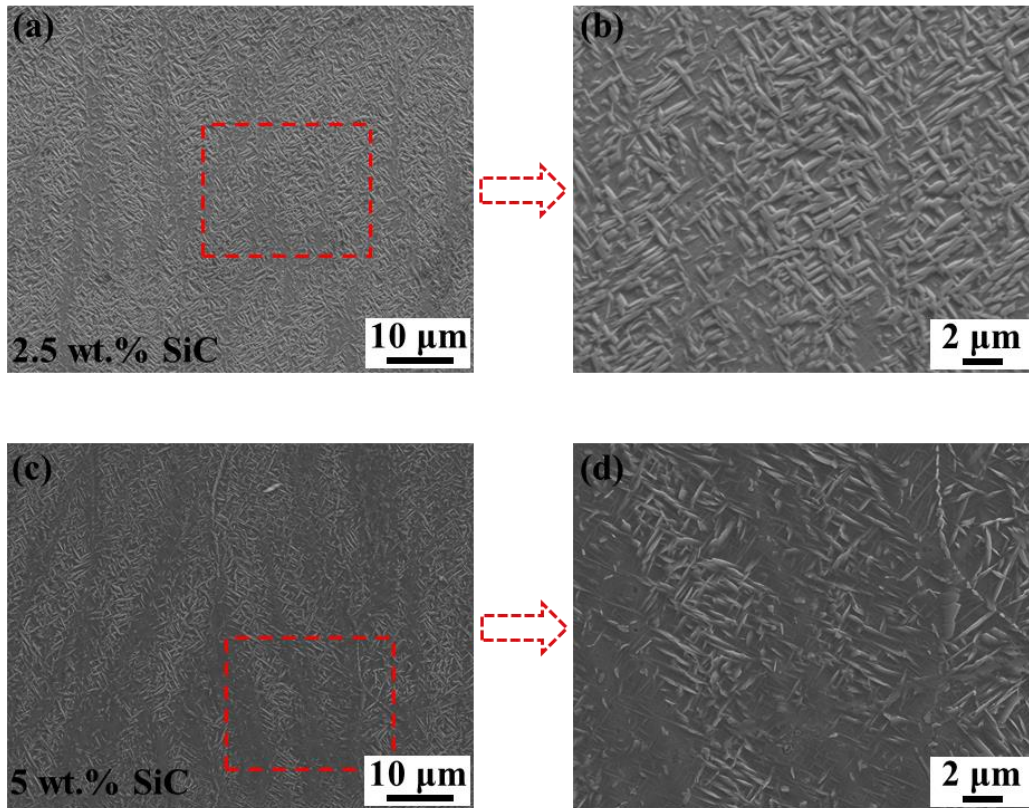


Figure 2.3: SEM images showing microstructure of TMNCs fabricated at a high energy input of laser power 200 W and scanning velocity 20 mm/s: (a, b) with 2.5 wt.% nano-SiC, and (c, d) with 5 wt.% nano-SiC.

Further characterizations were conducted to identify phases in SLM-fabricated TMNCs. The XRD results in Figure 2.4 demonstrated that both TMNC-0 and TMNC-5 samples are primarily composed of hexagonal close-packed α -Ti phase. The strong diffraction peaks corresponding to Ti_5Si_3 phase can be clearly identified in TMNC-5, indicating the in-situ

reaction between Ti and Si during laser processing. It is worth mentioning that diffraction peaks of SiC or TiC are not identified, indicating none or limited amount of SiC and TiC in SLM-fabricated parts. In addition, the enlarged view in Figure 2.4(b) shows that diffraction peaks of α -Ti shifts to the left after adding nano-SiC, which could be ascribed to the increased lattice constant of α -Ti due to the interstitial solution of C atoms in the α -Ti lattice.

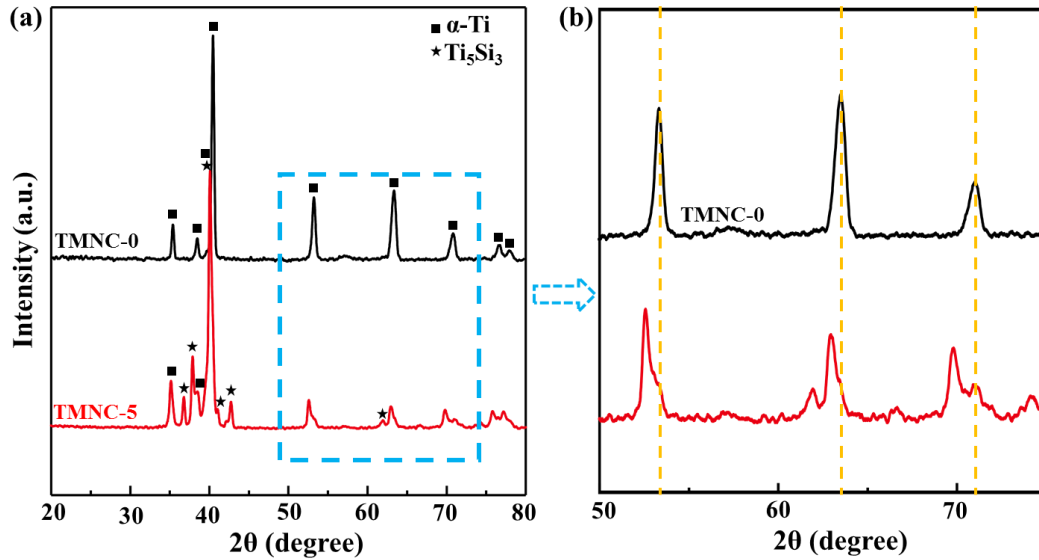


Figure 2.4: (a) XRD patterns of TMNC-0 and TMNC-5. (b) Enlarged view of XRD patterns showing the shift of α -Ti peaks.

Moreover, TEM analysis was carried out to further characterize the in-situ synthesized Ti_5Si_3 , dendritic/globular grains and elemental distribution in TMNC-5. The high-angle annular dark-field (HAADF) image in Figure 2.5(a) clearly shows the Type I and Type II grains as well as a nano-scale lamellar structure at the grain boundary. Based on the EDS results shown in Figure 2.5(b-d), such lamellar structure showing alternative composition change in Ti and Si is deemed to be the typical Ti+ Ti_5Si_3 eutectic structure, similar as reported in other literatures [16, 26]. Clearly, a quasi-continuous nano- Ti_5Si_3 network architecture is obtained in TMNC-5. In addition, both Type I and Type II grains are mainly composed of Ti (>90 at.%). Combined with the selected area electron diffraction (SAD) patterns and corresponding dark field image [Figure

2.5(e) and (f)], it is confirmed that the Type I grain and the acicular plates in type II grain are the α -Ti phase. More importantly, due to the existence of the 60-degree growth angle of dendritic arms (typically found in hcp structure) in Figure 2.2(e) and the absence of acicular plates inside the Type I grains, we conclude that the dendritic/globular α -Ti grain is directly formed from the melt pool rather than from $\beta(\text{bcc}) \rightarrow \alpha(\text{hcp})$ phase transformation. Here, we denote the Type I grain as primary α_p phase and acicular α -Ti in the Type II grain (prior- β) as secondary α_s phase. Moreover, it is also found that Type I grain contains a higher amount of C and a lower amount of Si, as compared to Type II grain. Finally, a spherical particle (marked by yellow dashed circle) can be found at the grain boundaries in the HAADF image and identified to be SiC based on the EDS results, showing that nano-SiC is not completely consumed during SLM.

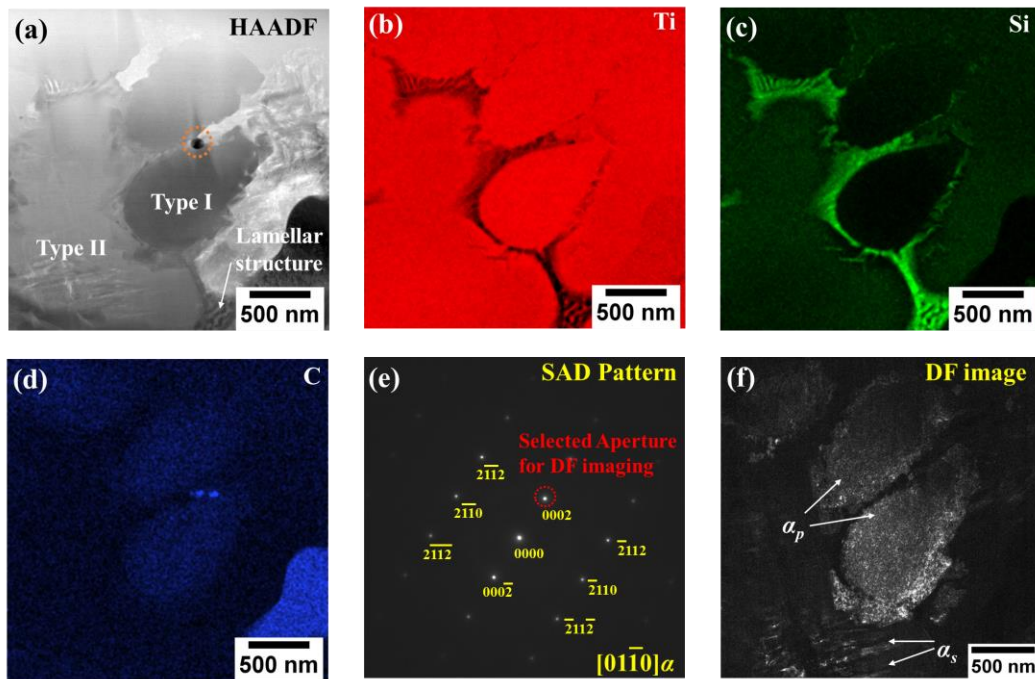


Figure 2.5: TEM analysis results: (a) HAADF-STEM image of TMNC-5. EDS mapping showing the elemental distributions of (b)Ti, (c)Si, and (d). (e) SAD pattern and (f) corresponding DF image.

Microstructure characterizations in Figure 2.2-2.5 indicate the fabrication of TMNC with a quasi-continuous network distribution of nano- Ti_5Si_3 by SLM of Ti and nano-SiC. To further

investigate the effect of nano-SiC on the grain growth during SLM, particularly the equiaxed/near equiaxed microstructure that could facilitate Ti_5Si_3 network formation, EBSD analysis was performed. Figure 2.6(a) is the inverse pole figure (IPF) map of TMNC-0, showing the grain orientations of α -Ti. The α_{GB} showing the chain morphology can be easily observed and is marked by white dashed lines. Consequently, prior- β columnar grains with a width of 20 - 40 μm and a length larger than 80 μm can be identified, which is consistent with the observation from the SEM image in Figure 2.2(a). In contrast, the solidification grain structure of TMNC-5 is dominated by equiaxed grains with an average size smaller than 8 μm , as shown in Figure 2.6(b). Clearly, a significant columnar-to-equiaxed grain transition in the solidification stage is achieved by adding 5 wt.% nano-SiC during SLM of Ti, which is more effective as compared to adding previously explored grain refiners such as Si or B [27]. Such ultrafine equiaxed grain structure provides abundant solidification grain boundaries for the formation of Ti_5Si_3 network in the TMNC-5. In addition, the crystallographic textures of as-fabricated TMNCs are influenced by nano-SiC, as confirmed by the corresponding $\{0001\}$ pole figures shown in Figure 2.6(c) and (d). Without nano-SiC addition [Figure 2.6(c)], the α -Ti phase presents a relatively strong crystallographic texture with a maximum orientation density of 11.09 (a description of preferential orientation strength). This strong crystallographic texture has been reported in other literatures [28, 29], and is caused by the columnar prior- β grain growth during solidification and the variant selection process [30] during $\beta \rightarrow \alpha$ solid state phase transformation. On the other hand, with 5 wt.% nano-SiC addition [Figure 2.6(d)], the microstructure shows a weakened crystallographic texture with the maximum orientation density of 6.54, since a number of equiaxed grains with different orientations are formed during solidification. The obtained

equiaxed solidification microstructure and weakened crystallographic texture are expected to be beneficial to isotropic mechanical properties of as-fabricated parts.

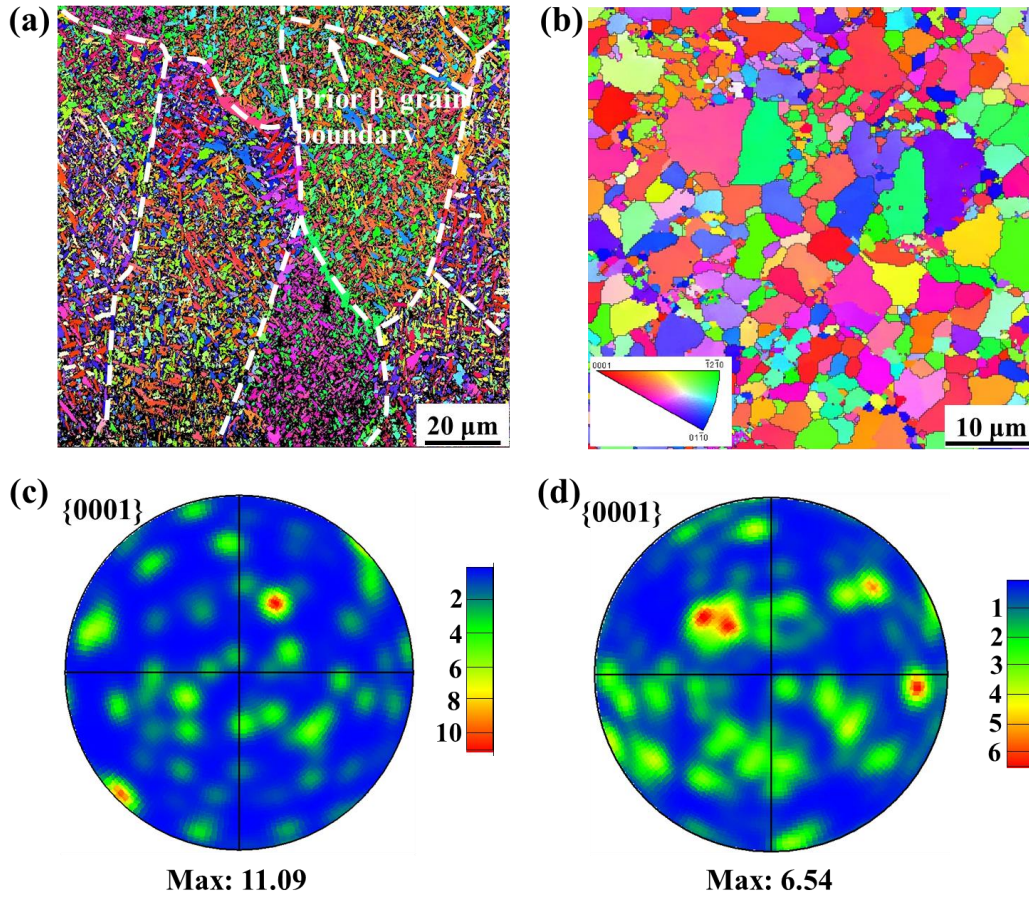


Figure 2.6: EBSD analysis results: IPF maps of (a) TMNC-0 and (b) TMNC-5; and $\{0001\}$ Pole figures of (c) TMNC-0 and (d) TMNC-5.

Mechanical properties

The presence of such quasi-continuous Ti_5Si_3 network and refined equiaxed grains in SLM-fabricated TMNCs is anticipated to significantly enhance their mechanical properties. To obtain fundamental insights into the property improvement, we performed hardness, spherical nanoindentation, and dry sliding tests. Figure 2.7 depicts the Vickers hardness values of TMNCs with different amounts of nano-SiC, indicating that the surface strength is linearly increased with the increase of nano-SiC amount. The surface hardness value of SLM-fabricated SiC-free sample

(TMNC-0) is 466 VHN, showing a 38.3% increase as compared to the substrate (Ti64, 337 VHN). This is similar as reported in Ref. [31] and can be explained by the formation of dominated acicular α -Ti. By adding 1, 2.5, and 5 wt.% of nano-SiC, the hardness values of TMNCs further increase to 588, 617, and 706 VHN, respectively. It is thus calculated that TMNC-5 with desirable microstructure increased the surface strength by 51.5% and 109.5% as compared to SiC-free sample and the substrate Ti64, respectively. Note that to demonstrate the influence of possible excessive amount (hypereutectic composition) of additions, TMNC coatings with higher than 5 wt.% nano-SiC were fabricated. It is found that for the sample with 10 wt.% nano-SiC, despite the continuously increased surface strength (up to 792 VHN), thermal cracks can be easily observed within the coating, which is similar as reported in Ref. [24] and could be explained by the thermal expansion mismatch between the severe aggregated ceramic particles and metal matrix. Additionally, the cracks formed after the micro-indentation/hardness testing (as shown in Figure 2.7(a)) indicates the extreme brittleness of as-fabricated TMNC sample. Consequently, in this study, 5 wt.% is considered as the optimal weight percentage of nano-SiC that can be added to obtain desired microstructure and maximally improve the surface strength while maintain the structure integrity of SLM-fabricated TMNCs.

Compared to other additions used for fabricating TMNCs by SLM [1, 32-36], nano-SiC exhibits a much higher effectiveness in strengthening Ti matrix especially in consideration of the amount of additions, as summarized in Figure 2.7(b). In this work, the addition of 1-5 wt.% SiC leads to a dramatic increasement in surface hardness of as-fabricated TMNCs, among which TMNC-5 with the in-situ formed Ti_5Si_3 network shows a hardness value more than twice that of the commercial Ti64. On the contrary, given similar weight percentage of additions, the surface strength of TMNCs produced by SLM using widely used TiB_2 and TiC is generally reported to

be maximally ~ 550 VHN, 63% higher than that of Ti64. The extraordinary surface strengthening by adding nano-SiC is comparable to that of titanium matrix composites (TMCs) with a high amount of micro-scale reinforcement, e.g., TMCs with 60% TiC fabricated by direct energy deposition showed a hardness of ~ 660 VHN [37]. Therefore, SLM of Ti mediated by minor nano-SiC addition is expected to make breakthrough in producing ultrahigh-strength TMNCs.

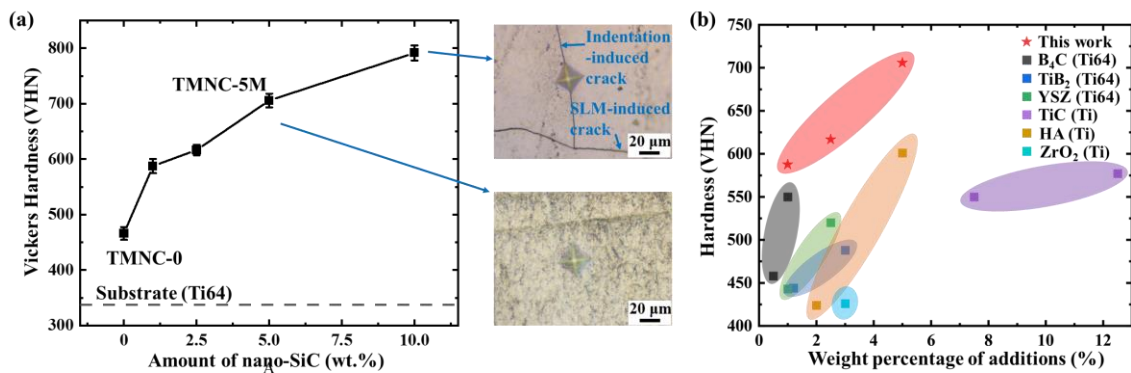


Figure 2.7: (a) Vickers hardness of TMNCs as affected by the amount of nano-SiC. (b) Comparison of Vickers hardness values of TMNCs with different additions.

To evaluate the material deformation behavior as affected by Ti₅Si₃ network and equiaxed grain structure, spherical nanoindentation experiments were carried out on TMNC-0 and TMNC-5 samples. The as-measured load-displacement data was converted to indentation stress-strain curves, as shown in Figure 2.8, following the protocols in Ref. [38]. It can be seen that the TMNC-5 presents an effective indentation modulus E_{eff} of 231 GPa, 62.7% higher than that of TMNC-0 (142 GPa). The indentation yield strength of TMNC-5 shows an enhancement of 57.2% from 1.52 to 2.39 GPa. Moreover, the post-elastic deformation indicates that TMNC-5 has a more pronounced strain hardening rate as compared to TMNC-0.

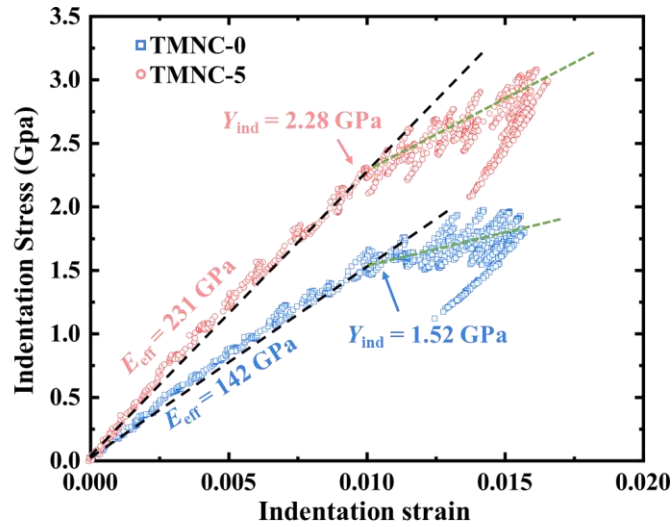


Figure 2.8: Indentation stress-strain curves of TMNC-0 and TMNC-5.

In addition, tribological performance of TMNC coatings was evaluated by conducting dry sliding tests on substrate (Ti64), TMNC-0, and TMNC-5. The 3D morphologies of wear tracks of different samples in Figure 2.9(a) demonstrate that the wear track of TMNC-5 is rougher and shallower than those of the substrate and TMNC-0, indicating enhancement in wear resistance and possible change in wear mechanism. To quantitatively investigate the improved wear resistance by quasi-continuous Ti_5Si_3 network and refined grain structure, 2D cross-sections of wear tracks of different samples are depicted in Figure 2.9(b). It is found that the wear track depth of TMNC-5 is $1.8 \mu\text{m}$, which is significantly shallower as compared to those of the substrate ($6.8 \mu\text{m}$) and TMNC-0 ($4.9 \mu\text{m}$), respectively. The wear rates, as shown in Figure 2.9(c), are calculated based on the dimensions of wear tracks. It is observed that the substrate has the highest wear rate of $42 \times 10^{-5} \text{ mm}^3/\text{N}\cdot\text{m}$, and TMNC-0 shows a slightly lower wear rate of $30 \times 10^{-5} \text{ mm}^3/\text{N}\cdot\text{m}$. TMNC-5 exhibits the lowest wear rate of $9 \times 10^{-5} \text{ mm}^3/\text{N}\cdot\text{m}$, demonstrating 70% and 78.6% reductions as compared to the TMNC-0 and substrate, respectively.

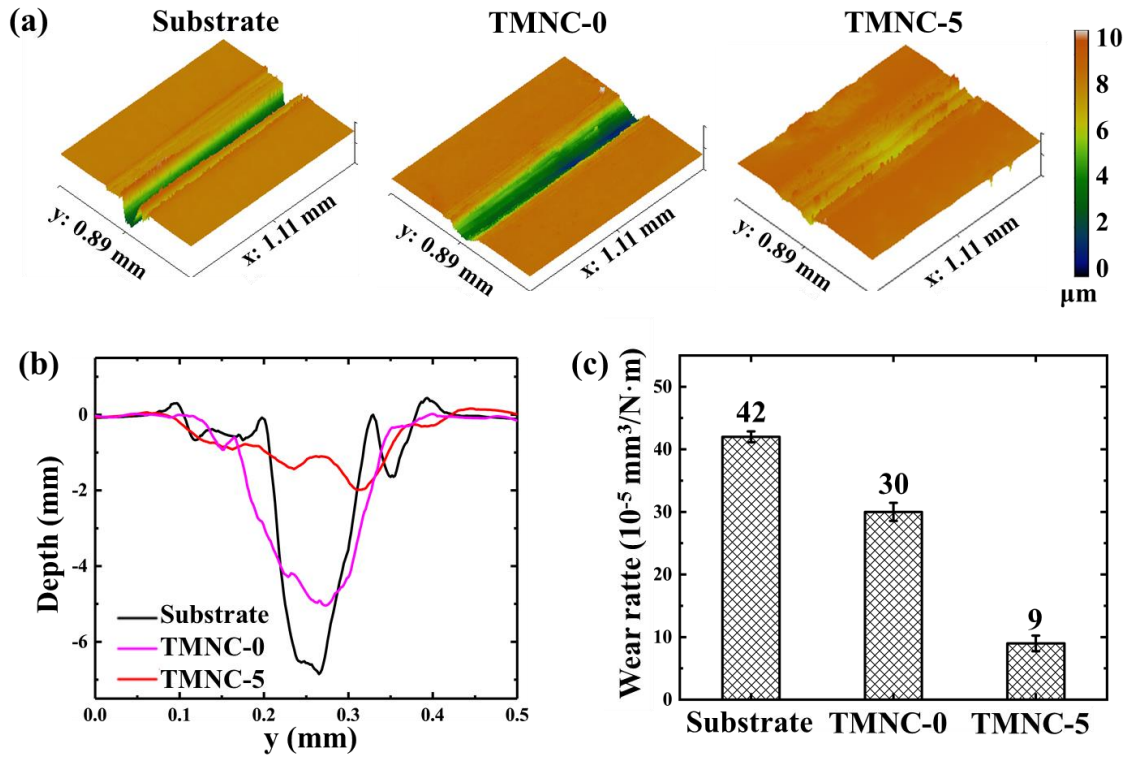


Figure 2.9: Tribological properties of SLM-fabricated TMNCs: (a) 3D morphologies, (b) 2D profiles of cross-sections of wear tracks, and (c) wear rates of substrate, TMNC-0 and TMNC-5.

To understand the possible change in wear mechanism due to the reinforcements, the worn surface morphologies of substrate, TMNC-0 and TMNC-5 were examined by SEM, as shown in Figure 2.10. A worn surface with deep parallel grooves [Figure 2.10(a)] can be observed on the substrate. This is due to the asperities of relative hard steel ball (746 VHN) penetrating into the soft Ti64 substrate (337 VHN), which leads to the typical two-body abrasion as the dominant wear mechanism. Similar surface morphology [Figure 2.10(b)] and wear mechanism were found in the TMNC-0 sample but with less abrasion. In contrast, the worn surface of TMNC-5 [Figure 2.10(c)] shows the absence of deep ploughing grooves and a large amount of wear debris. The EDS result [Figure 2.10(d)] indicates that these debris contain a small amount of Fe element (red color), which confirms the formation of transfer layer from steel

ball onto TMNC-5. Thus, it is reasonable to consider that the dominant wear mechanism changes from abrasion for TMNC-0 to adhesion for TMNC-5.

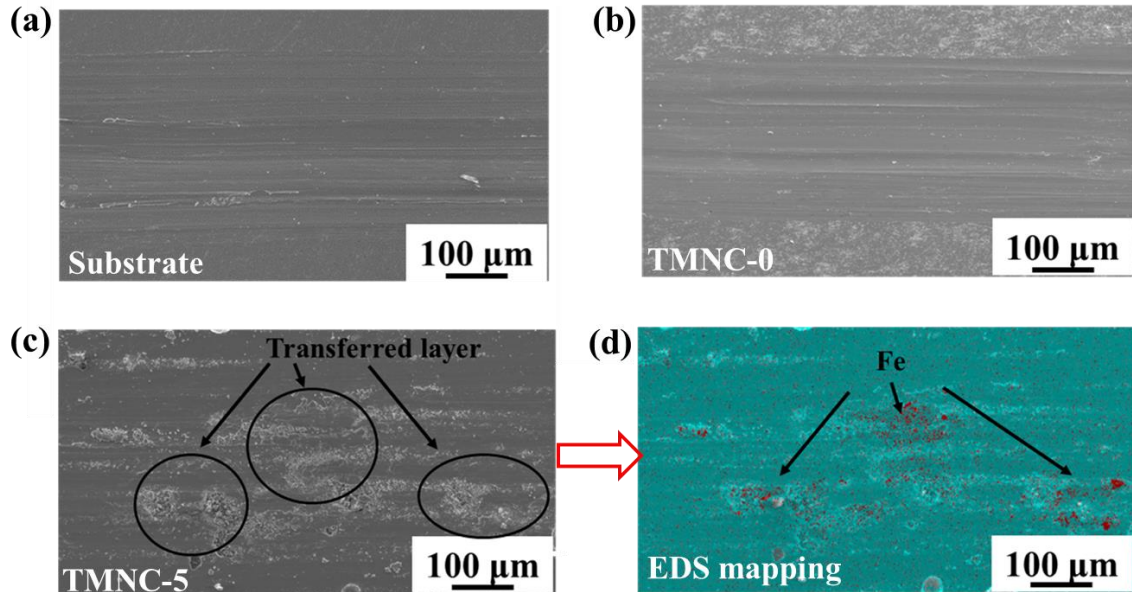


Figure 2.10: SEM images of worn surfaces of (a) substrate, (b) TMNC-0 and (c) TMNC-5. (d) EDS mapping of worn surface of TMNC-5.

Discussion

Formation of quasi-continuous network

Based on the characterization results, the phase transformation process during SLM of TMNC-5 with a hypoeutectic composition (<8.3 wt.% Si) follows the sequences: L (Liquid) \rightarrow L + primary β + primary α_p \rightarrow primary β + primary α_p + eutectic (β -Ti+Ti₅Si₃) \rightarrow acicular α_s (within prior- β) + primary α_p + eutectic (α -Ti+Ti₅Si₃). Figure 2.11 schematically illustrates the proposed mechanism responsible for the formation of quasi-continuous Ti₅Si₃ network and equiaxed grain structure in SLM-fabricated TMNC-5. In a typical SLM fabrication of Ti, a melt pool with liquid Ti is generated when the laser beam is absorbed by the powder bed. In the solidification stage, the ultrafast cooling rate during SLM leads to the formation large columnar β -Ti grains. Later on, solid-state phase transformation occurs, where α -Ti starts to nucleate at the

β -Ti grain boundary, followed by the formation of acicular α -Ti with a basket-weave pattern within the prior- β grains [39].

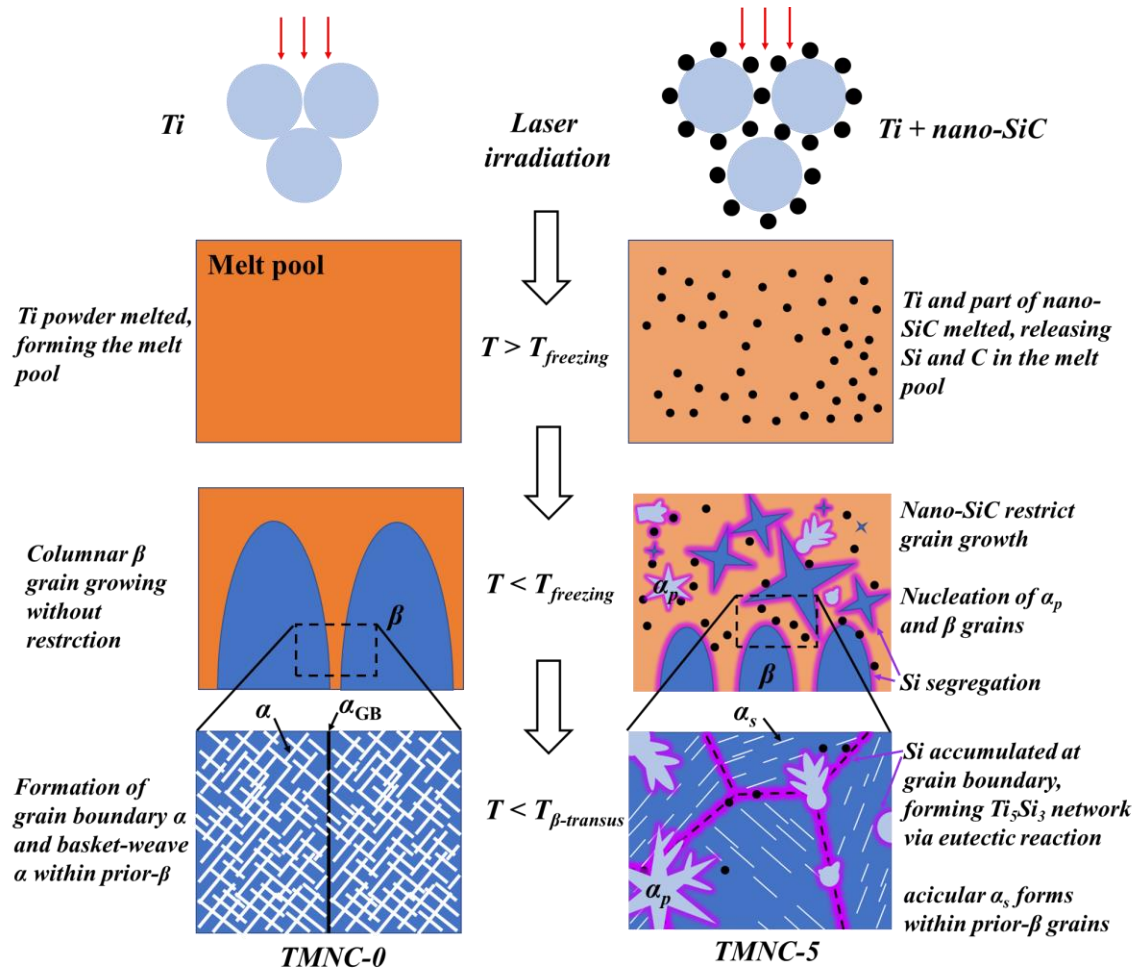
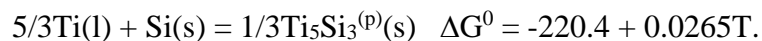
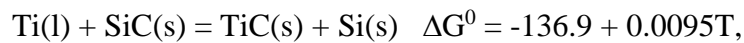


Figure 2.11: Schematic illustration of mechanism responsible for the formation of quasi-continuous Ti_5Si_3 network .

For SLM of Ti with the addition of nano-sized SiC, the laser energy input is tuned to a moderate level to achieve part of nanoparticles being dissolved, releasing Si and C atoms into the melt pool. At this stage, nano-SiC could also be consumed by the following chemical reaction between Ti and SiC due to the negative change in Gibbs free energy, resulting in the formation of $Ti_5Si_3^{(p)}$ and TiC particles [40]:



The symbols “l” and “s” indicates liquid and solid state, respectively. Upon solidification, β -Ti grain nucleates and grows from the bottom of melt pool. However, as the solidification front advances and encounters remained nano-SiC, the solid-liquid interface evolves into a nonlinear (curved) geometry. The growth of such curved interface requires additional undercooling [21]. Meanwhile, the released Si in the melt pool is rejected into the liquid, due to its low solubility in solid Ti. Such microsegregation of Si decreases the liquidus temperature near the solidification front and results in constitutional undercooling [41]. Thus, both remained nano-SiC and released Si contribute to the grain growth restriction by providing enhanced undercooling, increasing the chances for potential nuclei to grow ahead of the columnar front. Note that besides regular β -Ti nuclei from the impurities, α -Ti nuclei also present within the melt pool in this study. This is proved by the presence of dendritic/globular primary α_p , which could be attributed to reasons including: the presence of C as α -Ti stabilizer, $\text{Ti}_5\text{Si}_3^{(p)}$ as a potential nucleus for α -Ti [42], and high undercooling [43]. As numerous α_p and β grains grow, they are further impeded once the grains start to impinge on one another, leading to the columnar-to-equiaxed grain transition and the final refined microstructure. Note that between α_p and β grains, C as a α -Ti stabilizer [44] is preferentially diffused into α_p grains, and Si as a β -Ti stabilizer [45] is preferentially diffused into primary β grains, which explains the non-uniform distribution of Si and C within the two types of grains in Figure 2.5. More importantly, Si continues to be rejected into the liquid during the solidification process, approaching the eutectic composition (8.3 wt.%) at the grain boundary. As a result, when the temperature drops to ~ 1330 °C, β -Ti+ Ti_5Si_3 lamellar structure is formed via eutectic reaction. As the temperature continuous to decreases to below β -transus temperature, $\beta \rightarrow \alpha$ phase transformation occurs in two regions: acicular α_s emerges inside the primary β grain; β -Ti+ Ti_5Si_3 lamellar structure becomes α -Ti+ Ti_5Si_3 structure. Consequently, the final

microstructure is consisted of dendritic/globular α_p , acicular α_s within prior- β , and quasi-continuous Ti_5Si_3 network at the grain boundary. It is worth pointing out the nano-SiC is continuously consumed during the solidification and later solid-state phase transformation, which could explain the observation of only few nano-SiC survives at the grain boundary. Also, a low amount of nano-SiC (<5 wt.%) or an excessive laser energy input could both lead to insufficient restriction on grain growth and thus failure in obtaining Ti_5Si_3 network.

Strengthening mechanism

The enhanced mechanical performance including microhardness, nanoindentation properties and wear resistance indicates that the strength of SLM-fabricated TMNC-5 is considerably higher than that of TMNC-0 and commercial Ti64. Considering the microstructural features including the quasi-continuous Ti_5Si_3 network, equiaxed grain structure and elemental distribution, the major possible strengthening mechanisms can be summarized as following: Hall-Petch strengthening $\Delta\sigma_{HP}$, Ti_5Si_3 -induced dislocation strengthening $\Delta\sigma_{dis}$, Ti_5Si_3 -induced load-bearing effect $\Delta\sigma_{lb}$, and solid solution hardening $\Delta\sigma_s$. Based on a modified Ramakrishnan's approach [46], the yield strength of TMNC-5, σ_y , could be formulated as:

$$\sigma_y = \sigma_0(1 + \Delta\sigma_{HP}/\sigma_0)(1 + \Delta\sigma_{dis}/\sigma_0)(1 + \Delta\sigma_{lb}/\sigma_0)(1 + \Delta\sigma_s/\sigma_0) \quad (2.1)$$

where σ_0 is the yield strength of TMNC-0.

The fine equiaxed grain structure due to nano-SiC addition could produce a larger grain boundary area to hinder the dislocation motion, thus enhancing the strength of Ti matrix. The increased yield strength can be described by the well-known Hall-Petch relationship [47]:

$$\Delta\sigma_{HP} = k_{HP}(d_2^{-0.5} - d_1^{-0.5}) \quad (2.2)$$

where k_{HP} is the material constant for Ti matrix (328 MPa· $\mu m^{0.5}$). d_1 and d_2 are the average grain size of TMNC-0 and TMNC-5. In this study, the primary columnar grains with a width of 20 - 40

μm and a length larger than $80\ \mu\text{m}$ in TMNC-0 was considerably refined to equiaxed grains with an average size of $5\ \mu\text{m}$ in TMNC-5. However, TMNC-5 has a smaller amount of acicular $\alpha\text{-Ti}$ due to the presence of α_p , leading to the softening effect on the nanocomposite.

The strengthening effect from the quasi-continuous Ti_5Si_3 network can be mainly ascribed to dislocation strengthening mechanism and load-bearing mechanism [48]. The increase in the yield strength due to dislocation strengthening could be written as [48]:

$$\Delta\sigma_{dis} = \sqrt{(\Delta\sigma_{Oro})^2 + (\Delta\sigma_{geo})^2 + (\Delta\sigma_{CTE})^2} \quad (2.3)$$

where $\Delta\sigma_{Oro}$ is the Orowan stress required for a dislocation to cross the Ti_5Si_3 lamellar structure. $\Delta\sigma_{geo}$ is the stress increase due to geometrically necessary dislocations resulting from the plastic deformation mismatch between Ti matrix and nano- Ti_5Si_3 . $\Delta\sigma_{CTE}$ is the stress increase due to additional dislocations resulting from the coefficient of thermal expansion mismatch between Ti matrix and nano- Ti_5Si_3 . The Orowan stress can be described by the Orowan-Ashby equation:

[47]:

$$\Delta\sigma_{Oro} = \frac{0.13Gb \ln(d_{eq}/2b)}{d_{eq}[2(V)^{-1/3}]} \quad (2.4)$$

where G and b are the shear modulus and burgers vector of metal matrix, respectively. V is the volume fraction of Ti_5Si_3 . d_{eq} is the equivalent diameter of Ti_5Si_3 phase and could be written as:

$$d_{eq} = \sqrt[3]{1.5d^2l} \quad (2.5)$$

where d and l are the width/diameter and length of Ti_5Si_3 phase in the lamellar structure. The stress increasement due to geometrically necessary dislocations can be expressed as:

$$\Delta\sigma_{geo} = 0.4G\sqrt{V\varepsilon b/d_{eq}} \quad (2.6)$$

where ε is the plastic strain of metal matrix. Note that $\Delta\sigma_{CTE}$ may not play important role in strengthening effect, as dislocations are rarely observed at the $\text{Ti}_5\text{Si}_3/\text{Ti}$ interface in TMNC-5

according to TEM results. This is because the CTE of Ti_5Si_3 ($10.8 \times 10^{-6} \text{ K}^{-1}$ [49]) is similar to that of Ti matrix ($11.3 \times 10^{-6} \text{ K}^{-1}$ [50]).

The strengthening due to load-bearing effect of Ti_5Si_3 could be expressed as [21]:

$$\Delta\sigma_{lb} = 1.5V\sigma_i \quad (2.7)$$

where σ_0 is the interfacial bonding strength between Ti_5Si_3 and Ti matrix. Since the Ti_5Si_3 is formed via in-situ reaction during SLM process, it is expected that a strong bonding strength would present and contribute to a large stress increase via load-bearing mechanism.

Solid solution hardening also plays important roles in the strengthening $\Delta\sigma_s$. EDS results (Figure 2.5) indicate that a few amount (<2 wt.%) of C and Si were diffused into the α_p and prior- β grains, respectively. In the work of Yan et al. [50], it was stated that C solid solution could lead to a maximal increase of 35 MPa in the yield strength of SLM-produced Ti matrix, due to its solution limit (0.05 wt.%) in α -Ti. Si has an even stronger strengthening effect for Ti matrix. In the work of Hsu et al. [16], it was reported that bending strength of as-cast Ti was improved from 844 to 1621 MPa by adding 1 wt.% Si.

In conclusion, the strengthening mechanism of SLM-fabricated TMNCs is complicated, which is an integration of contributions from Hall-Petch strengthening, Ti_5Si_3 -induced dislocation strengthening, Ti_5Si_3 -induced load-bearing effect, and solid solution hardening. Future investigation is needed to elucidate details of strengthening mechanism responsible for the ultrahigh-strength, and related mechanical properties of laser printed TMNCs.

Conclusion

In summary, the TMNC reinforced with a novel quasi-continuous Ti_5Si_3 network was successfully fabricated by SLM of Ti and nano-sized SiC. The microstructure evolution as affected by nano-SiC amount and laser energy input were investigated. The enhanced

mechanical properties were evaluated by hardness, spherical nanoindentation and dry sliding tests. The main findings in this work are as follows:

(1) TMNC with a quasi-continuous Ti_5Si_3 network could be produced by SLM at the optimized nano-SiC addition (5 wt.%) and laser energy input (150 W, 20 mm/s). The microstructure of TMNC under optimal conditions presented nano-scale $\text{Ti}_5\text{Si}_3+\text{Ti}$ lamellar eutectic structure at the grain boundary and a bimodal grain structure consisted of dendritic/globular α_p and acicular α_s within prior- β .

(2) The formation of Ti_5Si_3 network could be attributed to the effective columnar-to-equiaxed grain transition and the segregated Si at the grain boundary resulting in the eutectic reaction between Ti and Si. The formation of ultrafine near-equiaxed/equiaxed grains (size less than 8 μm) was caused by the grain growth restriction due to the pinning effect of nano-SiC and the Si-induced constitutional undercooling. The formation of the bimodal grain structure could be attributed to the simultaneous nucleation and growth of α_p and β phases during solidification and subsequent $\beta \rightarrow \alpha_s$ acicular transition.

(3) The nano-SiC addition presented a significantly higher effectiveness in strengthening Ti matrix, as compared to other nano-ceramics (e.g., TiC, TiB_2 and ZrO_2). The surface hardness, effective indentation modulus and indentation yield strength of optimized TMNC with quasi-continuous Ti_5Si_3 network are 706 VHN, 231 GPa and 2.28 GPa, which are 51.5%, 62.6%, 57.2% enhancements comparing with the SLM-produced reinforcement-free sample, respectively. In addition, the wear tests revealed that the wear rate was reduced by 70%, and the wear mechanism transferred from abrasion to adhesion due to the elevated surface strength.

(4) The strengthening mechanism of SLM-fabricated TMNCs is an integration of contributions from Hall-Petch strengthening, Ti_5Si_3 -induced dislocation strengthening, Ti_5Si_3 -

induced load-bearing effect, and solid solution hardening. Future investigation is needed to elucidate details.

This work demonstrates an effective AM strategy in fabricating ultrahigh-strength TMNC coatings with quasi-continuous Ti_5Si_3 network. The results gained in this work advance the understanding of the role of nano-additives during metal AM, and provide new insights and guidance to process design and optimization. The developed strategy is anticipated to be applicable to a wide variety of alloys, and thus will promote AM of high-performance metal matrix nanocomposites with desired microstructures and properties towards harsh environment applications.

References

- [1] H. Li, Z. Yang, D. Cai, D. Jia, Y. Zhou. Microstructure evolution and mechanical properties of selective laser melted bulk-form titanium matrix nanocomposites with minor B₄C additions. *Mater. Des.*, 185, (2020), p. 108245.
- [2] W.H. Yu, S.L. Sing, C.K. Chua, C.N. Kuo, X.L. Tian. Particle-reinforced metal matrix nanocomposites fabricated by selective laser melting: A state of the art review. *Progress in Materials Science*, 104, (2019), pp. 330-379.
- [3] M. Hasan, J. Zhao, Z. Jiang. Micromanufacturing of composite materials: a review. *Int. J. Extreme Manuf.*, 1(1), (2019), p. 012004.
- [4] L.J. Huang, L. Geng, H. Peng, J. Zhang. Room temperature tensile fracture characteristics of in situ TiBw/Ti6Al4V composites with a quasi-continuous network architecture. *Scr. Mater.*, 64(9), (2011), pp. 844-847.
- [5] L. Huang, S. Wang, Y. Dong, Y. Zhang, F. Pan, L. Geng, H. Peng. Tailoring a novel network reinforcement architecture exploiting superior tensile properties of in situ TiBw/Ti composites. *Mater. Sci. Eng., A*, 545, (2012), pp. 187-193.
- [6] C. Cai, S. He, L. Li, Q. Teng, B. Song, C. Yan, Q. Wei, Y. Shi. In-situ TiB/Ti-6Al-4V composites with a tailored architecture produced by hot isostatic pressing: microstructure evolution, enhanced tensile properties and strengthening mechanisms. *Composites Part B: Engineering*, 164, (2019), pp. 546-558.
- [7] D. Morikawa, J. Ramkumar, H. Mabuchi, H. Tsuda, T. Matsui, K. Morii. Microstructure and mechanical properties of Ti-BN cast alloys prepared by reactive arc-melting. *Mater. Trans.*, 43(9), (2002), pp. 2193-2196.

- [8] X. Zhang, M. He, W. Yang, K. Wu, Y. Zhan, F. Song. Structure and mechanical properties of in-situ titanium matrix composites with homogeneous Ti₅Si₃ equiaxial particle-reinforcements. *Mater. Sci. Eng., A*, 698, (2017), pp. 73-79.
- [9] Y. Jiao, L. Huang, S. Wei, L. Geng, M. Qian, S. Yue. Nano-Ti₅Si₃ leading to enhancement of oxidation resistance. *Corros. Sci.*, 140, (2018), pp. 223-230.
- [10] Y. Jiao, L. Huang, Q. An, S. Jiang, Y. Gao, X. Cui, L. Geng. Effects of Ti₅Si₃ characteristics adjustment on microstructure and tensile properties of in-situ (Ti₅Si₃+ TiBw)/Ti₆Al₄V composites with two-scale network architecture. *Mater. Sci. Eng., A*, 673, (2016), pp. 595-605.
- [11] J. Wang, L. Li, C. Tan, H. Liu, P. Lin. Microstructure and tensile properties of TiCp/Ti₆Al₄V titanium matrix composites manufactured by laser melting deposition. *Journal of Materials Processing Technology*, 252, (2018), pp. 524-536.
- [12] X. Li, G. Ji, Z. Chen, A. Addad, Y. Wu, H. Wang, J. Vleugels, J. Van Humbeeck, J.-P. Kruth. Selective laser melting of nano-TiB₂ decorated AlSi₁₀Mg alloy with high fracture strength and ductility. *Acta Materialia*, 129, (2017), pp. 183-193.
- [13] C. Zhang, J. Zhu, H. Zheng, H. Li, S. Liu, G.J. Cheng. A review on microstructures and properties of high entropy alloys manufactured by selective laser melting. *Int. J. Extreme Manuf.*, 2(3), (2020), p. 032003.
- [14] D. Cheng, L. Li. An overview of laser-based multiple metallic material additive manufacturing: from macro-to micro-scales. *Int. J. Extreme Manuf.*, 3, (2020), p. 012003.
- [15] S. Mereddy, M.J. Bermingham, D.H. StJohn, M.S. Dargusch. Grain refinement of wire arc additively manufactured titanium by the addition of silicon. *Journal of Alloys and Compounds*, 695, (2017), pp. 2097-2103.
- [16] H.-C. Hsu, S.-C. Wu, S.-K. Hsu, Y.-C. Li, W.-F. Ho. Structure and mechanical properties of as-cast Ti-Si alloys. *Intermetallics*, 47, (2014), pp. 11-16.
- [17] J.H. Martin, B.D. Yahata, J.M. Hundley, J.A. Mayer, T.A. Schaedler, T.M. Pollock. 3d printing of high-strength aluminium alloys. *Nature*, 549(7672), (2017), pp. 365-369.
- [18] D. Gu, H. Wang, D. Dai, P. Yuan, W. Meiners, R. Poprawe. Rapid fabrication of Al-based bulk-form nanocomposites with novel reinforcement and enhanced performance by selective laser melting. *Scripta Materialia*, 96, (2015), pp. 25-28.
- [19] B. AlMangour, D. Grzesiak. Selective laser melting of TiC reinforced 316L stainless steel matrix nanocomposites: Influence of starting TiC particle size and volume content. *Mater. Des.*, 104, (2016), pp. 141-151.
- [20] B. AlMangour, Y.-K. Kim, D. Grzesiak, K.-A. Lee. Novel TiB₂-reinforced 316L stainless steel nanocomposites with excellent room-and high-temperature yield strength developed by additive manufacturing. *Composites Part B: Engineering*, 156, (2019), pp. 51-63.

- [21] C. Cao, G. Yao, L. Jiang, M. Sokoluk, X. Wang, J. Ciston, A. Javadi, Z. Guan, I. De Rosa, W. Xie. Bulk ultrafine grained/nanocrystalline metals via slow cooling. *Science advances*, 5(8), (2019), p. eaaw2398.
- [22] L.-P. Lefebvre, E. Baril, L. de Camaret. The effect of oxygen, nitrogen and carbon on the microstructure and compression properties of titanium foams. *J. Mater. Res.*, 28(17), (2013), pp. 2453-2460.
- [23] D. Texier, Q. Sirvin, V. Velay, M. Salem, D. Monceau, B. Mazères, E. Andrieu, R. Roumiguier, B.B. Dod, Oxygen/nitrogen-assisted degradation of the mechanical behavior of titanium alloys exposed at elevated temperature, *Ti2019: The 14th world conference on titanium*, 2019, p. 4 p.
- [24] P. Krakhmalev, I. Yadroitsev. Microstructure and properties of intermetallic composite coatings fabricated by selective laser melting of Ti–SiC powder mixtures. *Intermetallics*, 46, (2014), pp. 147-155.
- [25] S.L. Lu, M. Qian, H.P. Tang, M. Yan, J. Wang, D.H. StJohn. Massive transformation in Ti–6Al–4V additively manufactured by selective electron beam melting. *Acta Materialia*, 104, (2016), pp. 303-311.
- [26] Y.-C. Lin, Y.-C. Lin. Microstructure and tribological performance of Ti–6Al–4V cladding with SiC powder. *Surface and Coatings Technology*, 205(23-24), (2011), pp. 5400-5405.
- [27] D.H. St John, S.D. McDonald, M.J. Bermingham, S. Mereddy, A. Prasad, M. Dargusch, The challenges associated with the formation of equiaxed grains during additive manufacturing of titanium alloys, *Key Eng. Mater.*, *Trans Tech Publ*, 2018, pp. 155-164.
- [28] C. Todaro, M. Easton, D. Qiu, D. Zhang, M. Bermingham, E. Lui, M. Brandt, D. StJohn, M. Qian. Grain structure control during metal 3D printing by high-intensity ultrasound. *Nat. Commun.*, 11(1), (2020), pp. 1-9.
- [29] P. Barriobero-Vila, J. Gussone, A. Stark, N. Schell, J. Haubrich, G. Requena. Peritectic titanium alloys for 3D printing. *Nat Commun*, 9(1), (2018), p. 3426.
- [30] H. Beladi, Q. Chao, G.S. Rohrer. Variant selection and intervariant crystallographic planes distribution in martensite in a Ti–6Al–4V alloy. *Acta Materialia*, 80, (2014), pp. 478-489.
- [31] F. Bartolomeu, M. Buciumeanu, E. Pinto, N. Alves, F. Silva, O. Carvalho, G. Miranda. Wear behavior of Ti6Al4V biomedical alloys processed by selective laser melting, hot pressing and conventional casting. *Transactions of Nonferrous Metals Society of China*, 27(4), (2017), pp. 829-838.
- [32] Z. Zhou, Y. Liu, X. Liu, Q. Zhan, K. Wang. Microstructure evolution and mechanical properties of in-situ Ti6Al4V–TiB composites manufactured by selective laser melting. *Composites Part B: Engineering*, 207, (2021), p. 108567.

- [33] A. Hattal, T. Chauveau, M. Djemai, J.J. Fouchet, B. Bacroix, G. Dirras. Effect of nano-yttria stabilized zirconia addition on the microstructure and mechanical properties of Ti6Al4V parts manufactured by selective laser melting. *Materials & Design*, 180, (2019), p. 107909.
- [34] D. Gu, G. Meng, C. Li, W. Meiners, R. Poprawe. Selective laser melting of TiC/Ti bulk nanocomposites: Influence of nanoscale reinforcement. *Scripta Materialia*, 67(2), (2012), pp. 185-188.
- [35] C. Han, Q. Wang, B. Song, W. Li, Q. Wei, S. Wen, J. Liu, Y. Shi. Microstructure and property evolutions of titanium/nano-hydroxyapatite composites in-situ prepared by selective laser melting. *J Mech Behav Biomed Mater*, 71, (2017), pp. 85-94.
- [36] J. Li, L. Shen, Z. Liu, H. Liang, Y. Li, X. Han. Microstructure, microhardness, and wear performance of zirconia reinforced pure titanium composites prepared by selective laser melting. *Materials Research Express*, 6(3), (2018), p. 036520.
- [37] M. Radhakrishnan, M. Hassan, B. Long, D. Otazu, T. Lienert, O. Anderoglu. Microstructures and properties of Ti/TiC composites fabricated by laser-directed energy deposition. *Addit. Manuf.*, 46, (2021), p. 102198.
- [38] S.R. Kalidindi, S. Pathak. Determination of the effective zero-point and the extraction of spherical nanoindentation stress–strain curves. *Acta Mater.*, 56(14), (2008), pp. 3523-3532.
- [39] Q. Zhang, J. Chen, X. Lin, H. Tan, W.D. Huang. Grain morphology control and texture characterization of laser solid formed Ti6Al2Sn2Zr3Mo1.5Cr2Nb titanium alloy. *Journal of Materials Processing Technology*, 238, (2016), pp. 202-211.
- [40] S.N. Li, H.P. Xiong, N. Li, B.Q. Chen, C. Gao, W.J. Zou, H.S. Ren. Mechanical properties and formation mechanism of Ti/SiC system gradient materials fabricated by in-situ reaction laser cladding. *Ceramics International*, 43(1), (2017), pp. 961-967.
- [41] D. Zhang, A. Prasad, M.J. Bermingham, C.J. Todaro, M.J. Benoit, M.N. Patel, D. Qiu, D.H. StJohn, M. Qian, M.A.J.M. Easton, M.T. A. Grain refinement of alloys in fusion-based additive manufacturing processes. *METALLURGICAL AND MATERIALS TRANSACTIONS 50TH ANNIVERSARY COLLECTION*, 51(9), (2020), pp. 4341-4359.
- [42] N. Li, C. Cui, S. Liu, S. Liu, S. Cui, Q. Wang. Microstructure and Mechanical Properties of Ti6Al4V Alloy Modified and Reinforced by In Situ Ti5Si3/Ti Composite Ribbon Inoculants. *Metals*, 7(7), (2017), p. 267.
- [43] B. Zhai, K. Zhou, H. Wang. Coupling effect of undercooling and cooling on Ti–Al–V alloy solidification. *Applied Physics A*, 126(1), (2020), p. 16.
- [44] E. Schwaighofer, B. Rashkova, H. Clemens, A. Stark, S. Mayer. Effect of carbon addition on solidification behavior, phase evolution and creep properties of an intermetallic β -stabilized γ -TiAl based alloy. *Intermetallics*, 46, (2014), pp. 173-184.

- [45] H.-S. Kim, W.-Y. Kim, S.-H. Lim. Microstructure and elastic modulus of Ti–Nb–Si ternary alloys for biomedical applications. *Scripta materialia*, 54(5), (2006), pp. 887-891.
- [46] N. Ramakrishnan. An analytical study on strengthening of particulate reinforced metal matrix composites. *Acta Mater.*, 44(1), (1996), pp. 69-77.
- [47] Y. Hu, W. Cong, X. Wang, Y. Li, F. Ning, H. Wang. Laser deposition-additive manufacturing of TiB-Ti composites with novel three-dimensional quasi-continuous network microstructure: Effects on strengthening and toughening. *Composites Part B: Engineering*, 133, (2018), pp. 91-100.
- [48] X. Guo, L. Wang, M. Wang, J. Qin, D. Zhang, W. Lu. Effects of degree of deformation on the microstructure, mechanical properties and texture of hybrid-reinforced titanium matrix composites. *Acta Mater.*, 60(6-7), (2012), pp. 2656-2667.
- [49] X. Huang, Y. Gao, Y. Yi, P. Xiao, Y. Jian, Y. Wang, S. Zhao, Q. Liu, Z. Ren. Microstructure evolution mechanisms and strength improvement of (6.5 vol% TiC+ 3.3 vol% Ti₅Si₃)/Ti6Al4V composites via heat treatments. *Mater. Sci. Eng., A*, 805, (2021), p. 140581.
- [50] Q. Yan, B. Chen, J. Li. Super-high-strength graphene/titanium composites fabricated by selective laser melting. *Carbon*, 174, (2021), pp. 451-462.

CHAPTER 3. SELECTIVE LASER MELTING OF GRAPHENE OXIDE-REINFORCED TI-48AL-2CR-2NB: IMPROVED MANUFACTURABILITY AND MECHANICAL STRENGTH

Xing Zhang¹, Bo Mao¹, Yiliang Liao¹, Yufeng Zheng²

¹ Department of Industrial and Manufacturing Systems Engineering, Iowa State University, Ames, IA 50011, USA

² Department of Chemical and Materials Engineering, University of Nevada, Reno, Reno, NV 89557, USA

Modified from a manuscript published in *Journal of Materials Research*

Abstract

Severe cracking and unsatisfied mechanical performance are the major challenges of manufacturing titanium aluminide (TiAl) components by selective laser melting (SLM). In this work, graphene oxide (GO) sheets were introduced onto the metal powder surface to improve the manufacturability of SLM of a Ti-48Al-2Cr-2Nb (at.%) alloy and enhance the mechanical strength of the laser-fabricated parts. The effect of laser power and GO content on the macro-morphology of single-track processing was investigated, showing that the crack-free track could be obtained with the addition of 0.1 - 0.5 wt.% GO under a laser power of 110 W. In addition, the characterization of multi-layer build-ups via electron backscatter diffraction and backscatter electron imaging reveals the grain refinement during SLM of GO/TiAl nanocomposites. Finally, the strength of the as-built samples was examined using micro-hardness test, showing a maximal increase of 21.9% by adding 0.3 wt.% GO into the TiAl powders from laser-fabricated samples without GO.

Introduction

In recent years, titanium aluminium (TiAl)-based alloys have received significant amount of attention as promising candidates to replace heavy-weight superalloys towards next generation aerospace and automobile applications. This is attributed to the unique combination of

characteristics of TiAl alloys, including the high specific strength, excellent creep and oxidation resistance at elevated temperature, and high ignition resistance [1-3]. It was reported that the GENx™ engine fabricated using Ti-48Al-2Cr-2Nb (at.%, Ti-4822) by General Electric can significantly reduce the fuel consumption, noise, and NO_x emission by 20%, 50%, and 80%, respectively, compared with the prior engines made of Ni-/Fe-based superalloys [4].

Nevertheless, it is difficult to manufacture TiAl components via machining or forming processes because of their poor room-temperature ductility and low high-temperature formability [5], leading to the restriction of their industrial applications .

As an effective additive manufacturing (3D printing) process, selective laser melting (SLM) has emerged as a promising manufacturing technique for fabricating near net-shape parts with complex geometries [6], and thus showed a great potential to produce high-performance TiAl components [7]. To date, very limited research [8-13] was conducted to study the manufacturability of processing TiAl alloys by SLM, and the relationship among processing parameters, microstructure and properties still requires further investigation. For example, Lober et al. [8] conducted a parametric study on a β -solidifying TiAl alloy. It was claimed that a narrow processing window with a scanning speed of 50 - 100 mm/s and a laser power of 100 - 250 W was required to produce smooth and stable melt tracks. Gussone et al. [9] investigated the effects of laser energy density on the microstructure evolution during SLM of a Ti-44.8Al-6Nb-1Mo-0.1B (at.%, Ti4461) alloy on a preheated substrate. It was found that a lower energy density led to less Al evaporation and a finer lamellar (α_2/γ) structure. Li et al. [10] investigated the effect of laser scanning speed on the microstructure and mechanical properties of a Ti-45Al-2Cr-5Nb alloy. It was reported that when the scanning speed increased from 500 to 800 mm/s, the α_2 phase decreased while the γ and B_2 phases increased in terms of volume fraction. The nano-

hardness and compression strength of the as-built TiAl alloy were also found to be increased with the increase of scanning speed.

Despite the increasing interests of processing TiAl alloys by SLM, defects such as cracks and pores can be easily found in the SLM-built parts. For instance, Loeber et al. [14] used SLM to process the Ti-4822 alloy and found an abundance of cracks in the as-built parts, which was explained by the combination of the SLM-induced high residual stress and the brittleness of TiAl alloys. Kenel et al. [15] also found a large number of cracks with a density of 2.38 to 4.51 mm/mm² when fabricating a Ti-45Al-3Nb alloy using SLM, and the cracks were predominantly oriented perpendicular to the laser scanning direction. Besides the cracking, Shi et al. [16] observed the formation of micro-pores and the significant loss of Al during SLM of a Ti-47Al-2Cr-2Nb alloy, due to the material evaporation induced by the high-energy laser beam. Moreover, the mechanical performance of the SLM-built parts without post-treatment is much less satisfied as compared to that of the as-casted parts. For example, Gussone et al. [9] found that the SLM-fabricated Ti4461 showed a tensile strength of 200 - 400 MPa, which was much lower than that of as-casted parts (450 – 700 MPa).

The aim of this work is to develop a manufacturing strategy to improve the manufacturability of SLM of Ti-4822 and enhance the mechanical strength of as-built parts. In specific, graphene oxide (GO), a two-dimensional material with high tensile strength, yield strength and creep resistance [17, 18], was added as a reinforcement and process modifier. SLM experiments were conducted to fabricate GO/Ti-4822 nanocomposites. The effects of GO on the macro-morphology and microstructure evolution were investigated using scanning electron microscopy (SEM), energy dispersive X-ray spectroscopy (EDS), and electron backscatter

diffraction (EBSD). The strength of SLM-fabricated samples was examined using micro-hardness test.

Methods

Fabrication of GO/Ti-4822 mixed powders

Spherical Ti-4822 powders (Praxair Surface Technologies, Inc.) with a diameter of 15 - 45 μm and the GO water dispersion (Graphenea) with a particle lateral size smaller than 10 μm were used as the raw materials in the present work. Several steps were required to prepare the GO/Ti-4822 mixture. Firstly, 4 g of Ti-4822 powders were added into 60 ml of a solvent composed of 80% ethanol and 20% water, followed by magnetic stirring for 30 min. Then, a certain amount of GO was added into the 60 ml solvent, followed by 5 min of probe ultrasonication. Finally, the uniformly dispersed GO colloid was added dropwisely into the Ti-4822 suspension with magnetic stirring until the solution at the top becomes transparent. The stirring time for mixture with 0.1, 0.3, and 0.5 wt. % GO were 2, 4, and 8 h, respectively. The mixture was finally rinsed with ethanol for three times.

SLM process

An Ytterbium fiber laser (YLR-500, IPG) with a maximal power of 500 W and a wavelength of 1070 nm was used to perform the SLM experiments. SLM processing was conducted on a Ti substrate ($25 \times 15 \times 5 \text{ mm}^3$). The processing parameters were as follows: laser power 90 - 130 W, beam radius 200 μm , scanning speed 1200 mm/min, hatch spacing 250 μm , layer thickness 100 μm . The selection of this relative low scanning speed (as compared to a typical SLM process) was to ensure the integrity of the as-scanned tracks for characterization in our preliminary study. An argon flow (10 L/min) was utilized as the protective gas during SLM processing. Zigzag scanning strategy, as shown in Figure 3.1, without any rotation between the layers was adopted for multi-layer build-up.

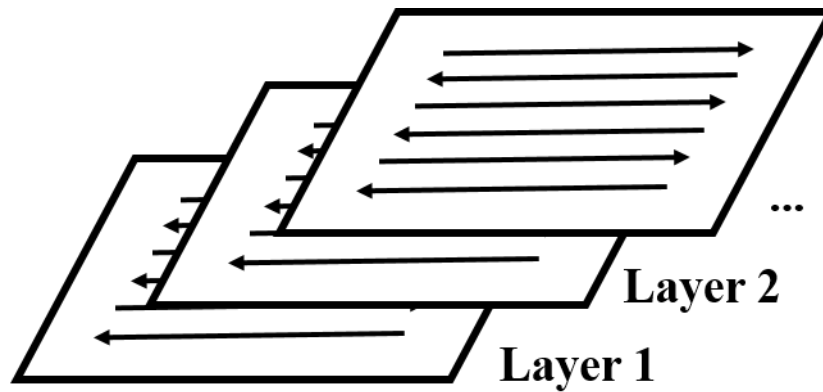


Figure 3.1: An illustration of adopted zigzag scanning strategy.

Microstructure characterization and hardness tests

The SLM-built samples were cross-sectioned using Buehler IsoMet 1000 cutter, ground with abrasive papers (up to 1200 grit), and finally vibrationally polished using 0.06 μm colloidal silica. A JEOL JSM-6010LA SEM was used to characterize the morphologies of powder particles at 20 kV. A JEOL JSM-7100FT field emission SEM was used to characterize the macro-morphologies of as-polished samples under the BSE mode at 10 kV. The chemical composition was analyzed by the EDS at 20 kV. EBSD scans were performed at an operating voltage of 25 kV and a sample tilt angle of 70° . The data acquisition was carried out with HKL Channel 5 software with a step size of 0.8 μm . Vickers hardness values were measured on the cross-sections using a Wilson hardness tester with a 200 g load and a 10 s holding time.

Results and Discussion

Characterization of the powders

It is well known that the GO sheets exhibit a negatively charge in an aqueous solution due to the abundance of functional groups such as carboxyl groups and ethers, whereas the Ti-4822 powder surfaces can be ionized because of the high standard reduction potential of Al/Al^{3+} (-1.68 V , $\text{Al} = \text{Al}^{3+} + 3\text{e}^-$) and Ti/Ti^{2+} (-1.63 V , $\text{Ti} = \text{Ti}^{2+} + 2\text{e}^-$) [19-21]. As a result, the GO sheets can be adsorbed onto metal powders via the electrostatic attraction, achieving the

homogeneous mixing of thin GO sheets with Ti-4822 powders. Figure 3.2(a) shows the photographs of solutions before and after adsorption. Prior to a stirring process, the upper layer of the solution shows the brown color of GO dispersion. After stirring for a certain time period, the upper layer becomes transparent, indicating an effective adsorption process between GO sheets and Ti-4822 powders, similar to the results reported in the work by Zhang et al. [18]. Figure 3.2(b) and (c) show SEM images of morphologies of Ti-4822 and GO-decorated Ti-4822 (0.3 wt.% GO) powders, respectively. GO in the morphology of thin sheets can be observed on the powder surfaces because of the wrinkling effect [22] and at powder interfaces due to the bridging effect, as marked in Figure 3.2(c).

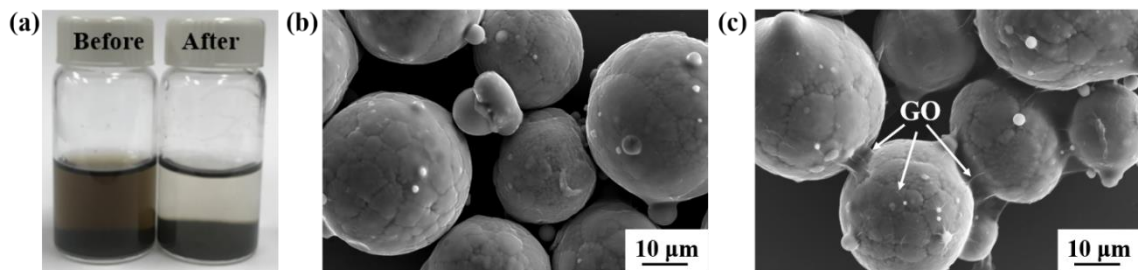


Figure 3.2: Photograph and images showing the absorption process of GO sheets onto the Ti-4822 powders: (a) Photograph showing GO/Ti-4822 solution before and after adsorption; (b-c) SEM images showing the morphology of (b) Ti-4822 powders and (c) 0.3 wt.% GO/Ti-4822 powders with arrows highlighting the GO sheets present at the surface and interface of the powders.

Improved manufacturability

The physical and mechanical properties of SLM-built parts strongly depend on the quality of each single track. Therefore, the effects of laser energy and GO content on the macro-morphology of melt pool were evaluated before the multi-layer structure was built up.

Backscatter electron (BSE) images in Figure 3.3 illustrate the cross-sections of single-track SLM of Ti-4822 with various GO content under laser powers of 90, 110 and 130 W. It can be observed that the scanning tracks of Ti-4822 without GO addition at these three laser energy levels exhibit

severely damaged perimeters and a large number of cracks, marked by white arrows in Figure 3.3(a). Nevertheless, by adding 0.1 wt.% GO, the as-built track under a laser power of 90 W shows a decreased crack density. Given a higher laser power of 110 or 130 W, a crack-free scanning track with a smooth perimeter can be obtained. With the addition of 0.3 wt.% GO, the quality of the scanning track under a laser power of 90 W is significantly improved. A higher laser power is also found to promote the elimination of defects. Further increasing GO content to 0.5 wt.% results in defect-free scanning tracks at all energy levels. Additionally, it is found that the dimensions of melt pools are decreased with the addition of GO. For instance, the height and width of as-built track of Ti-4822 under a laser power of 110 W are 150 and 490 μm , respectively. By adding 0.3 wt.% GO, the height and width of the melt pool are reduced to 117 and 448 μm , respectively. Such observed reduction in the dimensions of the melt pool is speculated due to the higher thermal conductivity of GO/Ti-4822 mixture compared with Ti-4822 powders, that arises from the higher conductivity of GO sheets and the increased contact surfaces among powders.

During the solidification of SLM-built parts, cracks tend to initiate from grain boundaries between adjacent matrix grains, where vacancies can be easily found, and from the defects such as pores and micro-scaled balls induced by melt splashes. For SLM of Ti-4822 powders, the laser-matter interaction is very violent, accompanied by the pronounced splashing of molten material out to the melt pool [23]. With the addition of GO sheets, partial area of the powder surface is shielded against directly laser irradiation, and the formed GO network [Figure 3.2(c)] constrains the material ejected from the melt pool. As a result, the defects caused by intense laser-matter interaction are reduced, leading to less crack initiations. Additionally, due to the significant mismatch of the coefficients of thermal expansion (CTE) between Ti-4822 (10.8×10^{-6}

6 K^{-1}) and GO ($-8 \times 10^{-6} \text{ K}^{-1}$), the localized thermal residual stresses induced by cooling is sufficient to produce a large number of dislocations at the GO/metal interface, resulting in the partial release of tensile residual stresses [24] and thus fewer solid-state cracks. Moreover, the crack growth can be restricted by GO sheets due to the crack-pinning and crack-deflection mechanisms [25]. When a crack propagates in the Ti-4822 matrix and encounters tougher GO sheets, it requires a much higher energy to penetrate these obstacles and grows along its original direction, thus leading to the crack front pinned or deflected toward GO-free regions.

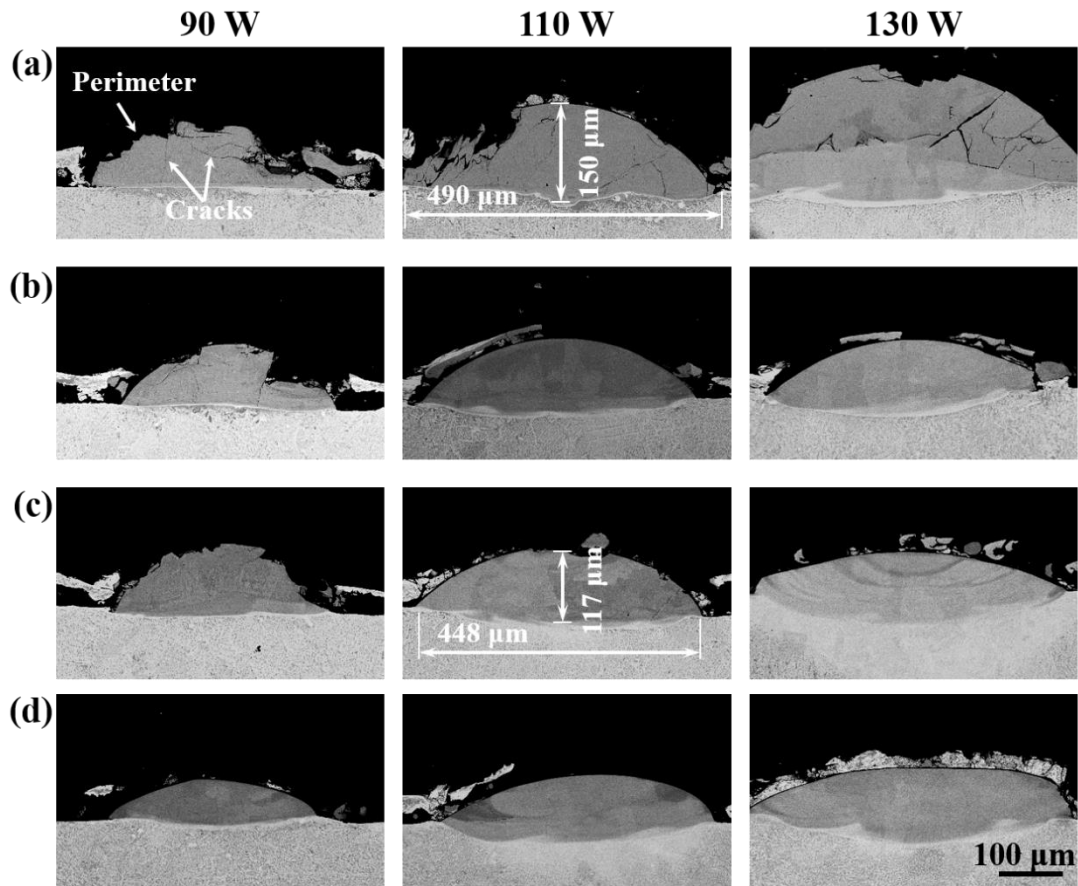


Figure 3.3: BSE images showing the macro-morphologies of the cross-sections in the single-track SLM of: (a) Ti-4822, (b) 0.1 wt.% GO/Ti-4822, (c) 0.3 wt.% GO/Ti-4822, and (d) 0.5 wt.% GO/Ti-4822 under the laser powers of 90, 110 and 130 W.

To further investigate the manufacturability of SLM of Ti-4822, multi-layer structures of Ti-4822 and 0.3wt% GO/Ti-4822 were built up and the characterization using BSE imaging is shown in Figure 3.4. A laser power of 110 W was chosen for this purpose to minimize the crack density and to avoid the overheating of the powder bed. By comparing the low magnification BSE images recorded from Ti-4822 and GO/Ti-4822 in Figure 3.4(a) and (b), it is found that there is a much lower crack density in the GO/Ti-4822 sample compared with that in the Ti-4822 sample, revealing the beneficial effect of GO on the cracking behavior during SLM process. In addition, layer band structures consisted of alternated regions of bright phase and dark phase can be observed in both samples [Figure 3.4(c) and (d)], which may be caused by the re-heat or re-melt of the previously solidified track/layer. Similar layer structure was also observed in Ti-4822 sample built via the electron beam melting, during which the formation of alternated duplex-like fine grain layers and coarser γ grain layers was attributed to the combination of pre-heated substrate and repeated local heat treatment [5]. Moreover, the chemical composition in each phase in the GO/Ti-4822 sample was determined using EDS analysis and the results are summarized in Table 3.1. It is shown that the average concentration of Al in the bright phase is 46.5 at. % and in the dark phase is 45.7 at.%, indicating only a slight loss of Al as compared to the initial powder. Therefore, it proves that the selected process parameters are suitable for SLM of Ti-4822.

Table 3.1: The average chemical composition (at.%) of SLM-fabricated 0.3 wt.% GO/Ti-4822 sample at different regions (highlighted in Figure 3.4(b)).

	Ti	Al	Cr	Nb
Region 1	49.4	46.8	2.0	1.8
Region 2	50.5	45.8	1.9	1.8
Region 3	50.1	46.2	1.9	1.8
Region 4	50.4	45.6	2.0	2.0

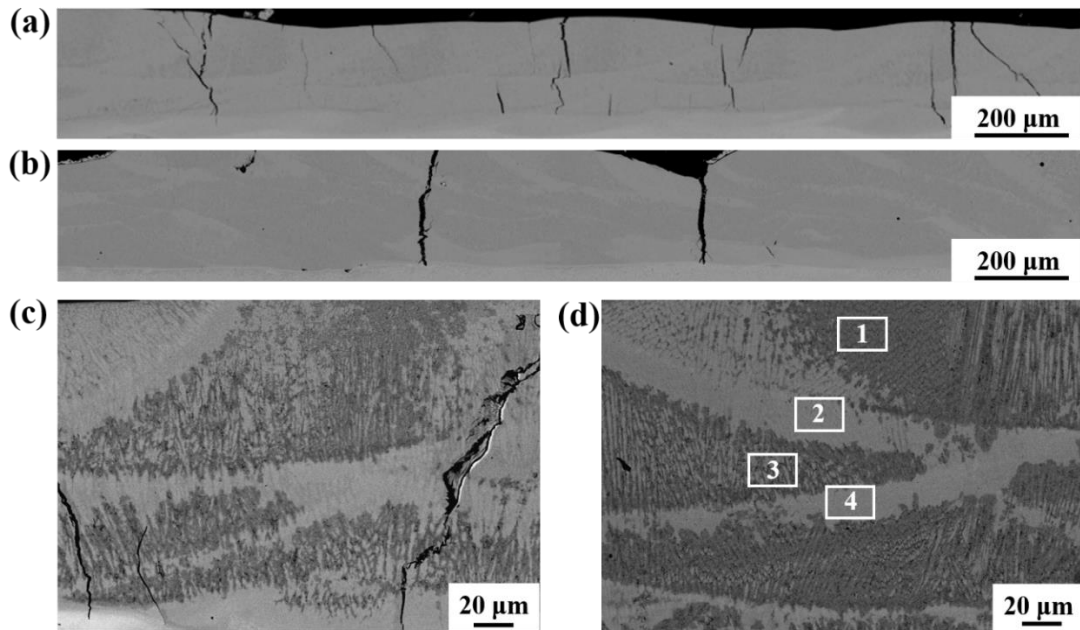


Figure 3.4: BSE images showing the cross-sections of SLM-fabricated multi-layer samples: low magnification images showing the large area of (a) Ti-4822 and (b) 0.3 wt.% GO/Ti-4822; and high magnification images showing the small area of (c) Ti-4822 and (d) 0.3 wt.% GO/Ti-4822.

Enhanced mechanical strength

The influence of GO content on the microhardness of SLM-built samples is illustrated in Figure 3.5. The results indicate that all GO/Ti-4822 samples exhibit higher average hardness values as compared to the Ti-4822 sample. By adding 0.3 wt.% GO, the as-built part shows a maximum value of 591 Vickers hardness number (VHN), which is 21.9% higher than that of Ti-4822 (485 VHN). Further increasing the GO content to 0.5 wt.% leads to a decrease of hardness value to 553 VHN. Such reduction in the surface strength could be attributed to the agglomeration and clustering of GO sheets [26].

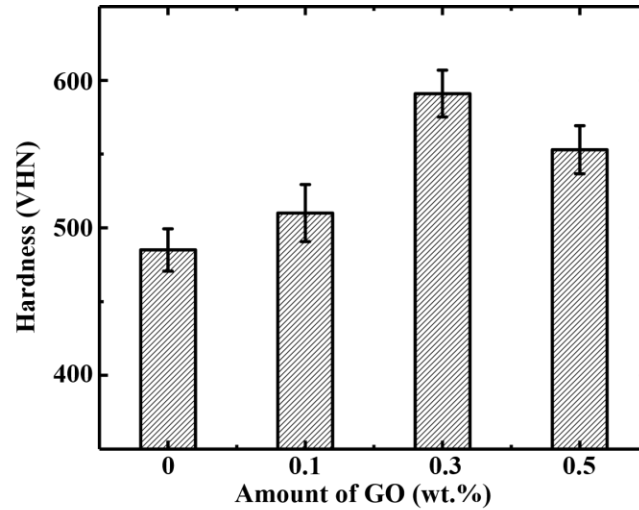


Figure 3.5: The Vickers hardness values of SLM-fabricated Ti-4822 samples with different wt. % of GO sheets.

In order to understand the strengthening effect by GO sheets, the microstructure of Ti-4822 and 0.3 wt.% GO/Ti-4822 samples was characterized using EBSD and BSE imaging. From the EBSD orientation maps [Figure 3.6(a) and (b)], the as-solidified coarse columnar grains (α_2 -Ti₃Al) can be clearly identified, whereas some regions are occupied by ultra-fine grains (γ -TiAl), similar to the microstructure reported in Seifi's work [27]. Moreover, it is found that the length and width of these columnar grains are significantly reduced after adding 0.3 wt.% GO. For instance, the width of grains is decreased from 25 - 50 μm in the Ti-4822 to 10 - 20 μm in the GO/Ti-4822 sample. This grain refinement is also observed at the sub-grain level, as shown in the high-magnification BSE images [Figure 3.6(c) and 5(d)]. These sub-grains/cells are formed because of the micro-segregation during rapid solidification, that the sub-grains/cells sharing a similar crystalline orientation eventually evolve into one large grain. It can be observed that the Ti-4822 sample exhibits a dendritic-cellular structure with an average sub-grain size (PDAS) of 4.2 μm , which is measured from the average distance between the centers of neighboring

cells/sub-grains. By adding GO sheets, the GO/Ti-4822 sample shows a dramatically refined cellular structure with an average PDAS of 2.2 μm . Liu et al. [28] observed the same microstructure change during the directional solidification of Ti-4822 when the cooling rate was increased from 2.9×10^3 to 1.5×10^4 K/s.

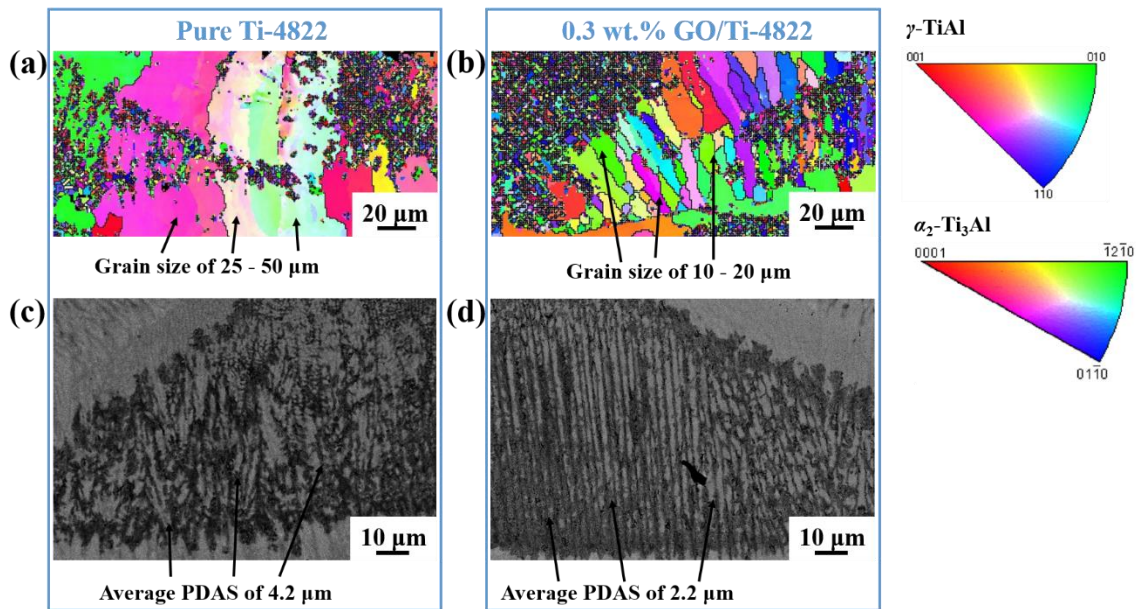


Figure 3.6: EBSD and BSE images showing the grain and sub-grain refinement: (a) EBSD orientation map showing coarse columnar grains in Ti-4822 and (b) EBSD orientation map showing refined columnar grains in 0.3 wt.% GO/Ti-4822 sample, with two legends on the right side indicating the grain orientations for columnar grains ($\alpha_2\text{-Ti}_3\text{Al}$) and ultra-fine ($\gamma\text{-TiAl}$) grains, respectively. (c) high-magnification BSE image showing coarse sub-grains in Ti-4822 and (d) high-magnification BSE image showing refined sub-grains in 0.3 wt.% GO/Ti-4822 sample.

The grain and sub-grain refinement induced by GO can be attributed to the following two reasons. Firstly, due to the high specific area of plate-like GO sheets present at grain boundary, the diffusion of atoms across the grain boundary is significantly restricted and a high Zener pinning force is generated [29], both of which will effectively constrain the grain growth. What is more, the increased thermal conductivity due to the presence of GO leads to a higher cooling rate during the SLM process, can result in a higher undercooling and thus create more nucleation

sites for the new grains. According to the work of Liu et al. [30], the cooling rate V_c during rapid solidification of TiAl-based alloys is related to the PDAS by: $PDAS = A_m(V_c)^{-0.55}$, where A_m is a material constant. Hence, ignoring the constraining effect of GO at the grain boundary, it can be estimated that the cooling rate during SLM is increased by 2.24 times after adding 0.3 wt.% GO.

According to the microstructural characteristics, the increased mechanical strength can be partially attributed to the grain refinement, which can be described by the Hall-Petch equation [31]:

$$\Delta\sigma_{hp} = k\left(\frac{1}{\sqrt{d}} - \frac{1}{\sqrt{d_0}}\right) \quad (3.1)$$

where k is the strengthening coefficient (0.5 MPa \cdot m^{-1/2} in Ti-4822 matrix [32]). d_0 and d is the average grain sizes of the Ti-4822 and GO/Ti4822 samples, respectively. Since the average PDAS is reduced from 4.2 to 2.2 μ m after adding 0.3 wt.% GO as shown in Figure 3.6, following the Hall-Petch equation, it can be calculated that the yield strength of 0.3 wt.% GO/Ti-4822 would be 93 MPa higher than that of the Ti-4822. In addition, dislocation pinning can also take place within the grains due to the uniformly distributed thin GO sheets. The resulted improvement of material strength can be explained by the Orowan mechanism expressed as [33]:

$$\Delta\sigma_{Orowan} = \frac{MGb}{2\pi\lambda(1-\nu)^{1/2}} \ln\left(\frac{\pi d_p}{4b}\right) \quad (3.2)$$

where M , G , b , and ν are the Taylor factor, shear modulus, Burgers vectors, and Poisson's ratio of Ti-4822 matrix, respectively. d_p is the mean particle size and λ is the effective inter-particle spacing. The value of λ which is highly related to the shape of the reinforcements is defined by Kim et al. [34] as:

$$\text{Plate-like particles: } \lambda = \left[0.912\sqrt{1/ef_v} - \pi/8 - 0.919/e\right]d_p \quad (3.3)$$

$$\text{Spherical particles: } \lambda = \left[0.779/\sqrt{f_v} - 0.785\right]d_p \quad (3.4)$$

where e and f_v are the aspect ratio (particle size/thickness) and volume fraction of the reinforcements, respectively. Clearly, given a constant volume fraction f_v , the increase of aspect ratio e will lead to the decrease of effective inter-particle spacing λ , thus leading to an increase in the local stress required for dislocation motion. For instance, the increased strength of a copper matrix reinforced by plate-like particles with an aspect ratio of 8 and a volume fraction of 0.03 was reported 8-times higher than that in the copper matrix reinforced by spherical particles with an aspect ratio of 1 [34]. Therefore, in this study, the incorporated GO sheets with a high aspect ratio of 100 - 1000 is expected to provide a strong Orowan strengthening effect and result in a high strength. Moreover, the generated high-density dislocations due to the CTE mismatch in Ti-4822 matrix and GO reinforcement could also contribute to the strengthening effect, expressed as [35]:

$$\Delta\sigma_{CTE} = \alpha Gb \sqrt{12\Delta T \Delta C f_v / bd_p} \quad (3.5)$$

where α is a material constant, ΔT is the change in temperature and ΔC is the mismatch of CTE. Hu et al. [36] observed a large number of dislocations near the GO/Ni interface after laser melting, and estimated the dislocation density as high as $6.5 \times 10^{17} \text{ m}^{-2}$. So it is expected in our GO/Ti-4822 the high density of the dislocations will also hinder their movement, due to the effect of dislocation entanglement. Based on the above three strengthening mechanisms introduced, the enhanced mechanical strength of GO/TiAl nanocomposites can be estimated as:

$$\Delta\sigma = \Delta\sigma_{lp} + \Delta\sigma_{Orowan} + \Delta\sigma_{CTE} \quad (3.6)$$

The effect of GO reinforcements on TiAl-GO nanocomposite's mechanical properties of yield strength, tensile strength, and fatigue performance will be investigated and reported in another effort.

Conclusion

In summary, GO/Ti-4822 nanocomposites were successfully fabricated by SLM and mechanical strength of as-built product was evaluated. The effects of GO reinforcements on the macro-morphology of melt pool, material's microstructure evolution and mechanical strength were investigated in detail. The major conclusions can be summarized as follows:

- (1) The manufacturability of SLM of TiAl alloys can be improved significantly by adding GO reinforcements. Given a high laser power (≥ 110 W), crack-free single-track can be obtained with the addition of 0.1 – 0.5 wt.% GO.
- (2) Grain refinement can be achieved by adding GO sheets during SLM of TiAl alloys. With the addition of 0.3 wt.% GO, the coarse columnar grain size was reduced from 25 - 50 to 10 - 20 μm , and the PDAS of sub-grain cellular structure was reduced from 4.2 to 2.2 μm .
- (3) The as-built GO/Ti-4822 nanocomposites exhibited higher surface strength as compared to the Ti-4822 sample. With the addition of 0.3 wt.% GO, the microhardness was maximally increased by 21.9%, from 485 to 591 VHN.

References

- [1] W. Li, Y. Yang, J. Liu, Y. Zhou, M. Li, S. Wen, Q. Wei, C. Yan, Y. Shi. Enhanced nanohardness and new insights into texture evolution and phase transformation of TiAl/TiB₂ in-situ metal matrix composites prepared via selective laser melting. *Acta Materialia*, 136, (2017), pp. 90-104.
- [2] Y. Ma, D. Cuiuri, C. Shen, H. Li, Z. Pan. Effect of interpass temperature on in-situ alloying and additive manufacturing of titanium aluminides using gas tungsten arc welding. *Additive Manufacturing*, 8, (2015), pp. 71-77.
- [3] G. Baudana, S. Biamino, B. Klöden, A. Kirchner, T. Weißgärber, B. Kieback, M. Pavese, D. Ugues, P. Fino, C. Badini. Electron Beam Melting of Ti-48Al-2Nb-0.7Cr-0.3Si: Feasibility investigation. *Intermetallics*, 73, (2016), pp. 43-49.
- [4] B. Bewlay, S. Nag, A. Suzuki, M. Weimer. TiAl alloys in commercial aircraft engines. *Materials at High Temperatures*, 33(4-5), (2016), pp. 549-559.

- [5] M. Todai, T. Nakano, T. Liu, H.Y. Yasuda, K. Hagihara, K. Cho, M. Ueda, M. Takeyama. Effect of building direction on the microstructure and tensile properties of Ti-48Al-2Cr-2Nb alloy additively manufactured by electron beam melting. *Additive Manufacturing*, 13, (2017), pp. 61-70.
- [6] X. Zhang, C.J. Yocom, B. Mao, Y. Liao. Microstructure evolution during selective laser melting of metallic materials: A review. *Journal of Laser Applications*, 31(3), (2019), p. 031201.
- [7] W. Li, J. Liu, Y. Zhou, S. Wen, Q. Wei, C. Yan, Y. Shi. Effect of substrate preheating on the texture, phase and nanohardness of a Ti-45Al-2Cr-5Nb alloy processed by selective laser melting. *Scripta Materialia*, 118, (2016), pp. 13-18.
- [8] L. Löber, F.P. Schimansky, U. Kühn, F. Pyczak, J. Eckert. Selective laser melting of a beta-solidifying TNM-B1 titanium aluminide alloy. *Journal of Materials Processing Technology*, 214(9), (2014), pp. 1852-1860.
- [9] J. Gussone, Y.-C. Hagedorn, H. Gherekhloo, G. Kasperovich, T. Merzouk, J. Hausmann. Microstructure of γ -titanium aluminide processed by selective laser melting at elevated temperatures. *Intermetallics*, 66, (2015), pp. 133-140.
- [10] W. Li, J. Liu, Y. Zhou, S. Li, S. Wen, Q. Wei, C. Yan, Y. Shi. Effect of laser scanning speed on a Ti-45Al-2Cr-5Nb alloy processed by selective laser melting: Microstructure, phase and mechanical properties. *Journal of Alloys and Compounds*, 688, (2016), pp. 626-636.
- [11] J. Gussone, G. Garces, J. Haubrich, A. Stark, Y.-C. Hagedorn, N. Schell, G. Requena. Microstructure stability of γ -TiAl produced by selective laser melting. *Scripta Materialia*, 130, (2017), pp. 110-113.
- [12] M. Thomas, T. Malot, P. Aubry, C. Colin, T. Vilaro, P. Bertrand. The prospects for additive manufacturing of bulk TiAl alloy. *Materials at High Temperatures*, 33(4-5), (2016), pp. 571-577.
- [13] W. Li, M. Li, J. Liu, Y. Yang, S. Wen, Q. Wei, C. Yan, Y. Shi. Microstructure control and compressive properties of selective laser melted Ti-43.5Al-6.5Nb-2Cr-0.5B alloy: Influence of reduced graphene oxide (RGO) reinforcement. *Materials Science and Engineering: A*, 743, (2019), pp. 217-222.
- [14] L. Loeber, S. Biamino, U. Ackelid, S. Sabbadini, P. Epicoco, P. Fino, J. Eckert, Comparison of selective laser and electron beam melted titanium aluminides, Conference paper of 22nd International symposium "Solid freeform fabrication proceedings", University of Texas, Austin, 2011, pp. 547-556.
- [15] C. Kenel, G. Dasargyri, T. Bauer, A. Colella, A.B. Spierings, C. Leinenbach, K. Wegener. Selective laser melting of an oxide dispersion strengthened (ODS) γ -TiAl alloy towards production of complex structures. *Materials & Design*, 134, (2017), pp. 81-90.
- [16] X. Shi, S. Ma, C. Liu, Q. Wu. Parameter optimization for Ti-47Al-2Cr-2Nb in selective laser melting based on geometric characteristics of single scan tracks. *Optics & Laser Technology*, 90, (2017), pp. 71-79.

- [17] Z. Hu, D. Wang, C. Chen, X. Wang, X. Chen, Q. Nian. Bulk titanium–graphene nanocomposites fabricated by selective laser melting. *Journal of Materials Research*, 34(10), (2019), pp. 1744-1753.
- [18] L. Zhang, G. Hou, W. Zhai, Q. Ai, J. Feng, L. Zhang, P. Si, L. Ci. Aluminum/graphene composites with enhanced heat-dissipation properties by in-situ reduction of graphene oxide on aluminum particles. *Journal of Alloys and Compounds*, 748, (2018), pp. 854-860.
- [19] Z. Li, G. Fan, Z. Tan, Q. Guo, D. Xiong, Y. Su, Z. Li, D. Zhang. Uniform dispersion of graphene oxide in aluminum powder by direct electrostatic adsorption for fabrication of graphene/aluminum composites. *Nanotechnology*, 25(32), (2014), p. 325601.
- [20] Q. Liu, M. He, X. Xu, L. Zhang, J. Yu. Self-assembly of graphene oxide on the surface of aluminum foil. *New Journal of Chemistry*, 37(1), (2013), pp. 181-187.
- [21] Z. Fan, K. Wang, T. Wei, J. Yan, L. Song, B. Shao. An environmentally friendly and efficient route for the reduction of graphene oxide by aluminum powder. *Carbon*, 48(5), (2010), pp. 1686-1689.
- [22] X. Shen, X. Lin, N. Yousefi, J. Jia, J.-K. Kim. Wrinkling in graphene sheets and graphene oxide papers. *Carbon*, 66, (2014), pp. 84-92.
- [23] C. Qiu, S. Yue, N.J. Adkins, M. Ward, H. Hassanin, P.D. Lee, P.J. Withers, M.M. Attallah. Influence of processing conditions on strut structure and compressive properties of cellular lattice structures fabricated by selective laser melting. *Materials Science and Engineering: A*, 628, (2015), pp. 188-197.
- [24] Y. Song, Y. Chen, W. Liu, W. Li, Y. Wang, D. Zhao, X. Liu. Microscopic mechanical properties of titanium composites containing multi-layer graphene nanofillers. *Materials & Design*, 109, (2016), pp. 256-263.
- [25] S. Wang, X. Wei, J. Xu, J. Hong, X. Song, C. Yu, J. Chen, X. Chen, H. Lu. Strengthening and toughening mechanisms in refilled friction stir spot welding of AA2014 aluminum alloy reinforced by graphene nanosheets. *Materials & Design*, 186, (2020), p. 108212.
- [26] A. Bhadauria, L.K. Singh, T. Laha. Effect of physio-chemically functionalized graphene nanoplatelet reinforcement on tensile properties of aluminum nanocomposite synthesized via spark plasma sintering. *Journal of Alloys and Compounds*, 748, (2018), pp. 783-793.
- [27] M. Seifi, A.A. Salem, D.P. Satko, U. Ackelid, S.L. Semiatin, J.J. Lewandowski. Effects of HIP on microstructural heterogeneity, defect distribution and mechanical properties of additively manufactured EBM Ti-48Al-2Cr-2Nb. *Journal of Alloys and Compounds*, 729, (2017), pp. 1118-1135.
- [28] Y. Liu, R. Hu, T. Zhang, H. Kou, J. Wang, G. Yang, J. Li. Dendritic growth and microstructure evolution with different cooling rates in Ti48Al2Cr2Nb alloy. *Journal of Materials Engineering and Performance*, 25(1), (2016), pp. 38-45.

- [29] S. Nam, K. Chang, W. Lee, M.J. Kim, J.Y. Hwang, H. Choi. Structural effect of two-dimensional BNNS on grain growth suppressing behaviors in Al-matrix nanocomposites. *Scientific reports*, 8(1), (2018), p. 1614.
- [30] S. Liu, H. Ding, J. Guo, H. Zhang, Z. Chen, Q. Wang, R. Chen, H. Fu. Rapid Cellular Crystal Growth of TiAl-Based Intermetallic without Peritectic Reaction by Melt-Quenching in Ga–In Liquid. *Crystal Growth & Design*, 17(4), (2017), pp. 1716-1728.
- [31] N. Hansen. Hall–Petch relation and boundary strengthening. *Scripta Materialia*, 51(8), (2004), pp. 801-806.
- [32] Y.-W. Kim. Strength and ductility in TiAl alloys. *Intermetallics*, 6(7-8), (1998), pp. 623-628.
- [33] D. Zhang, Z. Zhan. Strengthening effect of graphene derivatives in copper matrix composites. *Journal of Alloys and Compounds*, 654, (2016), pp. 226-233.
- [34] W. Kim, T. Lee, S. Han. Multi-layer graphene/copper composites: Preparation using high-ratio differential speed rolling, microstructure and mechanical properties. *Carbon*, 69, (2014), pp. 55-65.
- [35] M. Rashad, F. Pan, A. Tang, M. Asif. Effect of Graphene Nanoplatelets addition on mechanical properties of pure aluminum using a semi-powder method. *Progress in Natural Science: Materials International*, 24(2), (2014), pp. 101-108.
- [36] Z. Hu, G. Tong, D. Lin, Q. Nian, J. Shao, Y. Hu, M. Saeib, S. Jin, G.J. Cheng. Laser sintered graphene nickel nanocomposites. *Journal of Materials Processing Technology*, 231, (2016), pp. 143-150.

CHAPTER 4. UNRAVELLING THE HETEROGENEITIES IN SUB-GRAIN CELLULAR STRUCTURE AND MICROMECHANICAL RESPONSE OF SELECTIVE LASER MELTED TI-NB ALLOYS: AN INTEGRATED EXPERIMENTAL AND COMPUTATIONAL INVESTIGATION

Xing Zhang¹, Wenye Ye², Leslie Mushgonra², Yiliang Liao¹

¹ Department of Industrial and Manufacturing Systems Engineering, Iowa State University, Ames, IA 50011, USA

² Department of Chemical and Materials Engineering, University of Nevada, Reno, Reno, NV 89557, USA

Modified from a manuscript under review in *Additive Manufacturing*[†]

Abstract

Additive manufactured (AM) metallic components often exhibit unique hierarchical and heterogenous microstructure. Recently, exploiting the heterogeneities in sub-grain microstructure and associated micromechanical response has been considered as a novel strategy to achieve unprecedented mechanical properties of AM-fabricated parts. In-depth understanding of such heterogeneities is critical for AM process control and optimization. In this work, selective laser melting (SLM) of a Ti-35Nb alloy is investigated with focus on the underlying mechanism responsible for the heterogeneities in site-specific sub-grain cellular structure and associated micromechanical response. The experimental results reveal significant changes in such heterogeneities across the melt pool as affected by SLM conditions. For in-depth investigation, a computational framework integrating a finite element thermal model, a phase-field grain growth model and a crystal plasticity micromechanical model is developed. The integrated experimental and computational effort is utilized to investigate the process-microstructure-property relationship at the sub-grain scale. In specific, the effects of process-induced thermal conditions on sub-grain microstructure, thereby micromechanical response, are investigated. Spatial

* This chapter is currently as work in progress. It may differ in significant ways from the published version.

distribution maps of sub-grain size and microhardness are constructed to demonstrate the heterogeneities within the melt pool. The roles of individual processing parameters on the spatial control of sub-grain microstructure and micromechanical response are evaluated.

Introduction

Additive manufacturing (AM), such as selective laser melting (SLM) and direct energy deposition (DED), has shown enormous potentials in fabricating metallic components with complex or customized structures for aerospace, automotive, energy, and medical applications. However, due to the rapid solidification and multiple thermal cycles during AM, the as-fabricated components often exhibit unique hierarchical microstructural features, which play a key role on determining mechanical properties for critical applications [1, 2]. Such hierarchical microstructure has been frequently reported for a number of additive manufactured alloys such as Inconel 718 [3], 316L SS [4], and AlSi10Mg [5], of which the typical characteristics of microstructure are columnar grains (10 - 100 μm) containing sub-grain cellular structures (0.2 - 2 μm) featured by multiple cells/sub-grains and element segregated boundaries within each individual grain [2]. Existing studies have mainly focused on the microstructure-property relationship at the grain scale and rarely considered the influence of sub-grain cellular structure. The sub-grain microstructural features, such as sub-grain size, elemental microsegregation, and precipitation, also significantly affect mechanical properties of as-fabricated parts including strength, fracture toughness, and fatigue performance. For instance, in the work of Wang et al. [6], it was reported that the sub-grain boundaries in the SLM-fabricated 316L SS could effectively arrest the dislocation motion, contributing to the enhanced strength. Zhang et al. [7] reported that Al segregation during SLM of Ti-48Al-2Cr-2Nb led to the formation of α_2 -Ti₃Al within the sub-grain and γ -TiAl at the sub-grain boundary. The volume fraction and distribution of these two phases determine the high-temperature performance of as-fabricated components.

Thus, in-depth understanding of the sub-grain microstructure evolution during AM is critical for obtaining desired mechanical properties.

It is well known that the sub-grain cellular structure formed during the rapid solidification is highly affected by thermal conditions, particularly the cooling rate and temperature gradient. However, AM process involves complex thermal conditions due to the non-uniform energy distribution and multiple thermal cycles. The spatial variations in these thermal conditions result in heterogenous sub-grain microstructure, as extensively reported in literature [4, 8]. This could further lead to the heterogeneity in site-specific micromechanical response, even within a single melt pool [9, 10]. These heterogeneities induce additional difficulties in investigating the process-microstructure-property relationship and cause uncertainties in component performance. To date, research efforts have been devoted to alleviating such heterogeneities and obtaining homogenous microstructure and uniform mechanical properties for AM-fabricated components. Nevertheless, recent investigations [6, 9] have provided a new perspective that such heterogeneities can be exploited to fabricate components with unprecedented mechanical properties. It was reported [6] that the heterogeneous sub-grain microstructure in SLM-fabricated 316L SS could lead to a strain hardening effect, contributing to an exceptional combination of strength and ductility surpassing that of conventional 316L SS. In addition, different levels of structural and chemical heterogeneities as affected by AM conditions were observed, leading to significant variances in component performance. Therefore, understanding the heterogeneities in site-specific sub-grain microstructure and associated micromechanical response is of specific importance for realizing AM of high-performance metallic components. To achieve this purpose, the following aspects need to be revealed: the quantitative linkage among process-microstructure-property at the sub-

grain scale; the underlying mechanisms responsible for heterogeneities in sub-grain microstructure and associated micromechanical response; the effects of processing parameters on such heterogeneities.

In this study, selective laser melting (SLM) of a Ti-35Nb alloy is investigated with focus on the underlying mechanism responsible for the heterogeneities in site-specific sub-grain microstructure and associated micromechanical response. Ti-Nb alloys are β -type Ti alloys, which have recently received considerable attention as the next-generation biomedical alloys for AM-produced implants due to its excellent biocompatibility and low elastic modulus. The site-specific solidification microstructure of as-fabricated Ti-35Nb was examined by backscattered electron (BSE) imaging and corresponding micromechanical response was evaluated by microhardness testing. A computational framework integrating a finite element thermal model, a phase-field grain growth model and a crystal plasticity micromechanical model was developed to investigate the formation mechanism of experimentally observed heterogeneities. Quantitative investigations of process-microstructure-property relationship were performed to demonstrate the spatial distribution of microstructure and nonuniform mechanical properties under varying processing parameters. The roles of laser power and scanning velocity on the spatial control of sub-grain cellular structure and micromechanical response were evaluated. This study provides valuable insights in understanding and controlling the heterogeneities in sub-grain microstructure and associated micromechanical response, and therefore will benefit the process control and optimization towards AM of high-performance metallic components for various applications.

Experimental procedure

Ti powders (AP&C) with the diameter of 45 - 90 μm and Nb powders (US Research Nanomaterials) with an average diameter of 40 μm were used as the starting materials. The powder mixture with a weight ratio of 65:35 (Ti:Nb) was prepared using a planetary ball mill

(BM6Pro, POWTEQ), with a rotation speed of 200 rpm, a ball-to-powder ratio of 5:1, and a processing time of 4h. The SLM experiments were performed using an Ytterbium fiber laser (YLR-1500-WC, IPG photonics) with a wavelength of 1070 nm. The Ti-35Nb samples were printed on a pure Ti substrate (McMaster-Carr) under argon atmosphere. The as-print samples were cross-sectioned by a diamond wire saw (STX-202A, MTI), and followed by the conventional grinding and polishing procedure. Keller's etchant was used to reveal the microstructure of SLM-fabricated Ti-35Nb. The microstructure characterization was performed using a scanning electron microscope (SEM, FT50, FEI) in the BSE imaging mode with an operating voltage of 10 kV. Local mechanical response was evaluated by performing the microhardness testing (LM 247AT, LECO) with a 25-gf load and a 13-s holding time.

Computational Framework

Given the complexity of SLM process and the limitation of in-situ characterization/monitoring, multi-scale/multi-physics integrated computational materials engineering (ICME) [11] has become an ideal approach for revealing the process-microstructure-property relationship. In our proposed ICME-based framework, as illustrated in Figure 4.1, the finite element thermal model is firstly used to investigate the complex thermal conditions including site-specific cooling rate and temperature gradient. Then, the thermal inputs are fed into the phase-field (PF) model to simulate the site-specific evolution of sub-grain cellular structure as affected by processing parameters. Finally, the predicted sub-grain cellular structure is integrated into the crystal plasticity (CP) model to investigate the micromechanical response. Note that, the proposed PF model is formulated using the driving force written in terms of thermodynamic factors (defined as the second derivative of a free energy function with respect to the solute concentration), therefore, eliminates the necessity for directly using free energy density values from the thermodynamic database. As compared to conventional PF models, the

applied PF model in this study has shown significantly improved efficiency in simulating rapid solidification, particularly for multi-phase multi-component systems, while maintaining a reasonable accuracy.

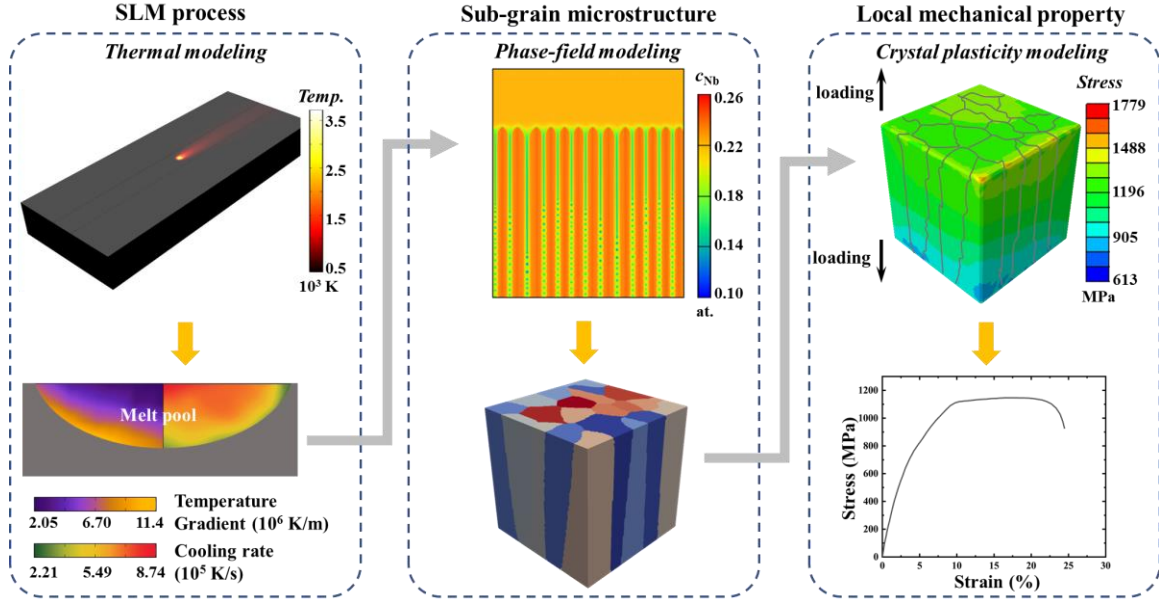


Figure 4.1: Schematic illustration of the proposed computational framework: understanding of the spatial distribution of microstructure and nonuniform mechanical properties under varying processing parameters.

Thermal modeling for solidification conditions

The tempo-spatial temperature field $T(x, y, z, t)$ during the SLM process, as a function of position (x, y, z) and time t , can be calculated by solving a three-dimensional (3D) transient heat conduction equation [12]:

$$\rho \frac{\partial c_p T}{\partial t} = \frac{\partial}{\partial x} \left(k \frac{\partial T}{\partial x} \right) + \frac{\partial}{\partial y} \left(k \frac{\partial T}{\partial y} \right) + \frac{\partial}{\partial z} \left(k \frac{\partial T}{\partial z} \right) \quad (4.1)$$

where ρ , k , and C_p are the material density, thermal conductivity and specific heat capacity, respectively. To obtain solutions from Eq. (4.1), relevant initial and boundary conditions are considered based on the experimental setup. In this study, the temperature of simulation domain is initially set as the ambient temperature: $T(x, y, z, 0) = T_0 = 298$ K. The thermal boundary

condition on the top surface of the powder bed is determined by the laser heat influx, heat convection and radiation [13]:

$$-k \frac{\partial T_s}{\partial z} = Q + h_c(T_0 - T_{surf}) + \varepsilon\sigma(T_0^4 - T_{surf}^4) \quad (4.2)$$

where T_{surf} is the top surface temperature, h_c is the heat convection coefficient, ε is the surface emissivity, and σ is the Stefan-Boltzmann constant. The laser heat source Q is approximated by a Gaussian distribution [14]:

$$Q = (1 - R) \frac{2P}{\pi r^2} \exp\left(-2 \frac{(x-vt)^2 - y^2}{r^2}\right) \quad (4.3)$$

where R is the material reflectivity, P is the laser power, r is the laser beam radius, and v is the scanning velocity. The boundary conditions on other surfaces are set to be adiabatic.

The established thermal model was implemented into the commercial software COMSOL Multiphysics, with a $2.5 \times 2 \times 1 \text{ mm}^3$ computational domain consisted of 0.1-mm-thick powder layer and 0.9-mm-thick as-print bulk. The alloy properties, such as reflectivity, temperature-dependent thermal conductivity and heat capacity, were calculated based on the mass fraction of each element and their elemental properties using data from Ref. [15-18]. Note that the density and thermal conductivity of powder bed were correlated to the porosity ψ [19, 20], which was assumed to be 0.5 in our study. The related material properties are listed in Table 1. Based on the experimental observations of manufacturability, SLM processing parameters are selected for modeling as summarized in Table 4.1. The key thermal parameters for the rapid solidification, including the cooling rate V and temperature gradient G , were captured from simulated temperature fields by:

$$G = \sqrt{(\partial_x T)^2 + (\partial_y T)^2 + (\partial_z T)^2}, V = dT/dt \quad (4.4)$$

Table 4.1: Material properties [15-18] and SLM processing parameters for the thermal modeling

Material properties	Powder bed	Bulk
Density, ρ (kg/m ³)	2700	5400
Reflectivity, R	0.3	0.523
Emissivity, ε	0.4	
Convection coefficient, h_c (W/m ² k)	15	
Processing parameters	Values	
Laser power, P (W)	180 - 270	
Scanning velocity, v (mm/s)	50 - 200	
Beam radius, r (mm)	0.2	

Phase-field modeling for grain growth

To simulate the microstructure evolution during SLM of Ti-35Nb alloy, a quantitative two-dimensional (2D) PF model [21, 22] was employed. This model has been used to capture the sub-grain growth and non-equilibrium microsegregation during rapid solidification of multi-component systems, at a higher computational efficiency as compared to other PF models. A non-conserved order parameter $\varphi \in [0, 1]$ representing liquid and solid phases and a conserved solute concentration field c representing elemental distribution are used to describe the sub-grain microstructure. In this work, the 2D PF computational domain is aligned with the transverse cross-section of the melt pool, i.e., the xz plane in the 3D thermal model. For the simulation of solidification, the temporal and spatial evolution of the PF variable $\varphi(x, z, t)$ is described as [21]:

$$\frac{\tau_0}{W} a(\theta)^2 \frac{\partial \varphi}{\partial t} = \vec{\nabla} [a(\theta)^2 \vec{\nabla} \varphi] + \partial_x \left[|\vec{\nabla} \varphi|^2 a(\theta) \frac{\partial}{\partial (\partial_x \varphi)} \right] + \partial_z \left[|\vec{\nabla} \varphi|^2 a(\theta) \frac{\partial}{\partial (\partial_z \varphi)} \right] - \frac{1}{W^2} \frac{\partial h(\varphi)}{\partial \varphi} + \frac{a_1}{W\mu} \frac{\partial g(\varphi)}{\partial \varphi} \Delta g_{ch} \quad (4.5)$$

where τ_0 , W , and μ are the relaxation time, interface width and interface energy, respectively.

The double well function $h(\varphi)$ is defined as $h(\varphi) = \varphi^2 (1 - \varphi)^2$, and the interpolation function $g(\varphi)$

is chosen as $g(\varphi) = \varphi^3 (10 - 15\varphi + 6\varphi^2)$. The term $a(\theta) = 1 + \delta \cos 4\theta$ represents the four-fold anisotropy function, where δ is the anisotropy strength and $\theta = \arctan(\partial_z \varphi / \partial_x \varphi)$ is the angle between the interface normal and the x axis. Δg_{ch} is the driving force for solidification determined from the chemical free energy density, and expressed as [23]:

$$\Delta g_{ch}(\varphi, c) = \frac{\chi_L(c_s^{eq} - c_l^{eq})(c - c^{eq})}{\varphi + (1 - \varphi)m_l/m_s} \quad (4.6)$$

where χ_L is the so-called thermodynamic factor of the liquid phase [24]. The parameters m_s and m_l are the solidus and liquidus slopes, respectively. The mean equilibrium concentration $c^{eq} = \varphi c_s^{eq} + (1 - \varphi)c_l^{eq}$ is calculated based on the weighted sum of the equilibrium concentrations in the solid (c_s^{eq}) and liquid (c_l^{eq}) phases.

The diffusion equation for the solute can be expressed by [21]:

$$\frac{\partial c}{\partial t} = \vec{\nabla} \left[(D_s + D_l(1 - \varphi)) \vec{\nabla} \frac{c - c^{eq}}{\varphi + (1 - \varphi)m_l/m_s} \right] + \frac{W}{\sqrt{2}} (c_s^{eq} - c_l^{eq}) \frac{\vec{\nabla} \varphi}{|\vec{\nabla} \varphi|} \frac{\partial \varphi}{\partial t} \quad (4.7)$$

where D_s and D_l are the solute diffusion coefficients in the solid and liquid phases, respectively.

To achieve quantitative analysis, the relaxation time of the system τ_0 is associated with the physical quantities as follows:

$$\tau_0 = \frac{a_1 a_2 W^3 \chi_L (c_s^{eq} - c_l^{eq})^2}{\mu D_l} \quad (4.8)$$

where numerical constants $a_1 = 0.2357$ and $a_2 = 2.35$ [25]. The transient temperature field for the PF modeling is correlated to the thermal inputs, V and G , by:

$$T(x, z, t) = T_L - \Delta T + G \left(z - \frac{3}{4}Z \right) - Vt + Gn_s l_s \quad (4.9)$$

where T_L is the liquidus temperature. The above equation is constructed to apply a shifting simulation box along the temperature gradient direction (z axis) for obtaining steady-state solutions with less computational cost. Specifically, when the solidification front reaches 3/4 of the simulation domain height Z , this frame is shifted in z direction with n_s and l_s being the shift

length and number of shifts, respectively. The undercooling $\Delta T = m_l(c_s^{eq} - c_l^{eq})\Omega$ can be related to the supersaturation $\Omega = \left(\frac{\pi^4 V d_0}{820 G \delta D_l}\right)^{1/5.4}$, where d_0 is the chemical capillary length [22].

In this study, the governing equations [Eqs. (4.5) and (4.7)] were solved in a 2D computational domain of $5 \times 6 \mu\text{m}^2$, where the grid spacing $dx = dz = 0.5W$. Zero-flux boundary conditions are applied to all boundaries, except for a constant concentration c_0 at the top of the domain. The interface thickness W was chosen to be 10 nm. The thermodynamic factor χ_L was derived using the CALPHAD database. The initial domain consisted of a set of randomly distributed nuclei at the bottom. The solute concentration field was set to be $c_s^{eq}(T_L)$ in the solid and $c_l^{eq}(T_L)$ in the liquid. Further details can be found in Ref. [8, 22]. The deduced material properties and modeling parameters used for simulating the evolution of sub-grain microstructure during SLM of Ti-35Nb are listed in Table 4.2.

Table 4.2: Material parameters used for the PF modeling [26].

Parameters	Values
Solidus temperature, T_S (K)	2025
Liquidus temperature, T_L (K)	2052
Equilibrium concentration in solid, $c_s^{eq}(T_L)$ (at.)	0.268
Equilibrium concentration in liquid, $c_l^{eq}(T_L)$ (at.)	0.219
Solidus slope, m_s (K/at.)	481
Liquidus slope, m_l (K/at.)	688
Diffusivity of solid, D_s (m ² /s)	6.5×10^{-13}
Diffusivity of liquid, D_l (m ² /s)	6.5×10^{-9}
Thermodynamic factor of liquid, χ_L (J/mol/at. ²)	1.45×10^5

Crystal plasticity modeling for local mechanical response

The microstructural features obtained from the PF modeling were used as inputs for the CP modeling to investigate the micromechanical response. In specific, with the predicted sub-

grain size, the 3D sub-grain cellular structure was reconstructed in an automated manner using Dream3D software [27]. The sub-grains were designed with a length to width to thickness ratio of 10:1:1, and distributed in a cubic computational domain with an edge of 2 μm using the algorithm of Voronoi tessellation [28]. Note that these sub-grains within each individual grain usually exhibit the same grain orientation, thus, were assigned the same Euler angle in the simulations. The reconstructed cellular structure, as shown in Figure 4.1, was meshed with Gmsh using four-node tetrahedral elements, followed by the execution of CP simulations under monotonic uniaxial loading along the sub-grain length direction.

In this study, the site-specific stress-strain behavior of SLM-produced Ti-35Nb was predicted by CP modeling, which uses phenomenological expressions to define both the slip rates and the evolution of the internal variables. The total deformation gradient F can be separated into the elastic (F^e) and plastic (F^p) contributions using the multiplicative decomposition approach [29], and expressed as: $F = F^e F^p$. The plastic contribution F^p represents the irreversible permanent deformation. The change rate of plastic deformation $\dot{\epsilon}$ is related to the slip rate $\dot{\gamma}^\alpha$ of the active slip system α by [30]:

$$\dot{\epsilon} = \sum_{\alpha=1}^N \dot{\gamma}^\alpha M \quad (4.10)$$

where N is the number of active slip systems and M is the Schmid factor that describes the relationship between the external normal stress and the critical resolved shear stress in a slip system. Then, the plastic deformation velocity gradient L^p can be determined by the slip direction vector s^α and the vector normal to the slip plane m^α by:

$$L^p = \sum_{\alpha=1}^N \dot{\gamma}^\alpha (s^\alpha \otimes m^\alpha) \quad (4.11)$$

The plastic strain rate during deformation \dot{p} can be written in terms of velocity gradient:

$$\dot{p} = \sqrt{\frac{2}{3} L^p : L^p} \quad (4.12)$$

The rate of shear deformation on the α^{th} slip system follows a power-law flow rule [31]:

$$\dot{\gamma}^\alpha = \dot{\gamma}_0 \left| \frac{\tau^\alpha - \chi^\alpha}{g^\alpha} \right|^{1/m} \text{sgn}(\tau^\alpha - \chi^\alpha) \quad (4.13)$$

where $\dot{\gamma}_0$ and m are the reference shear strain rate and strain rate-sensitivity exponent, respectively. τ^α , χ^α , and g^α are the resolved shear stress, back stress, and drag stress on the α^{th} slip system, respectively. The Drag and back stresses evolve by following the Armstrong-Frederick relation [32]:

$$\dot{g}^\alpha = H \sum_{\beta=1}^N q^{\alpha\beta} |\dot{\gamma}^\beta| - R g^\alpha \sum_{\beta=1}^N |\dot{\gamma}^\beta| \quad (4.14)$$

$$\dot{\chi}^\alpha = A_{dir} \dot{\gamma}^\alpha - A_{dyn} \chi^\alpha |\dot{\gamma}^\alpha| \quad (4.15)$$

where H and R are the direct hardening and dynamic recovery coefficients for the drag stress, respectively. $q^{\alpha\beta}$ is the latent hardening matrix consisting of 1 for diagonal terms for self-hardening and 1.0 for the cross-terms for latent hardening [33, 34]. A_{dir} and A_{dyn} are the direct hardening and dynamic recovery coefficients for the back stress, respectively.

The established CP model was implemented into ABAQUS using the user-defined material subroutine (UMAT). To calibrate this model for describing the deformation behavior of SLM-produced Ti-35Nb, a genetic fitting algorithm [35] was employed to identify appropriate CP parameters. Specifically, the genetic algorithm systematically varied possible sets of CP parameters in Eqs. (4.13), (4.14) and (4.15), until the simulation results matched well with the experimental data. The identified CP parameters listed in Table 4.3 were adopted for the simulations in this research.

Table 4.3: Calibrated parameters for the CP modeling.

Parameters	Values
Elastic constant, C_{11} (GPa)	165 GPa
Elastic constant, C_{12} (GPa)	98 GPa
Elastic constant, C_{44} (GPa)	55 GPa
Initial shear strain rate, $\dot{\gamma}_0$	0.55
Strain rate sensitivity exponent, m	1.66
Initial isotropic hardening, $g^{(0)}$	336.3
Direct hardening coefficient, H	6502.5
Dynamic hardening parameter, R	41.2
Direct hardening parameter, A_{dir}	19.0
Dynamic recovery parameter, A_{dvn}	79.1
Latent hardening ratio, $q^{a\beta}$	1.0

Results and Discussion

Site-specific solidification microstructure

A commonly observed microstructure in SLM-produced metallic components is the columnar cellular structure consisted of rod-like sub-grains. Figure 4.2 shows BSE images of the cross-section of such cellular structure in Ti-35Nb processed by SLM under a laser power of 210 W and a scanning velocity of 200 mm/s, within which sub-grains generally grow perpendicular to the melt pool boundary (dashed lines) towards the center of melt pool. Sub-grain heterogeneity within the melt pool, particularly the sub-grain size decreasing at locations closer to the center of the melt pool, can be observed. This is clearly demonstrated by the higher magnification images of multiple regions (A1-A4 in Figure 4.2), showing the as-measured sub-grain sizes of $\lambda = 0.54, 0.72, 0.96,$ and $1.44 \mu\text{m}$, respectively. In addition, the contrast between sub-grains and sub-grain boundaries indicates possible chemical heterogeneity in the cellular structure, which has been previously identified in SLM of AlSi10Mg [36] and 316L SS [6].

Moreover, sub-grains appear without secondary arms, indicating that the solid-liquid interface instabilities are significantly restricted at the sides of sub-grains in this case.

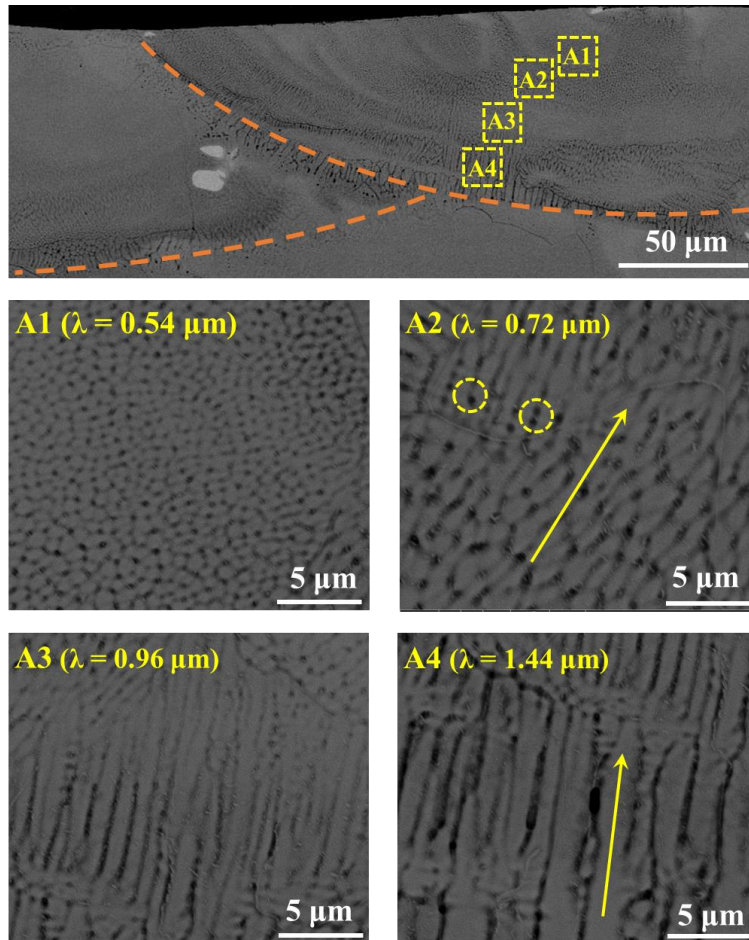


Figure 4.2: BSE images showing the spatial variations in the solidification microstructure of Ti-35Nb fabricated by SLM under a laser power of 210 W and a scanning velocity of 200 mm/s.

Fundamentally understanding the formation mechanism of such heterogeneous sub-grain microstructure is essential for SLM process control and optimization. In the following discussion, PF modeling is conducted to firstly examine the general microstructural features of SLM-produced Ti-35Nb, including sub-grain size and elemental segregation. The second modeling effort focuses on investigating the spatial variations in the sub-grain cellular structure as affected by the site-specific thermal loadings. The general evolution of cellular structure, as shown in Figure 4.3, is demonstrated by a PF simulation performed at a given cooling rate of 6.9

$\times 10^5$ K/s and a temperature gradient of 1.4×10^6 K/m (within the appropriate range of thermal variables during SLM). Figure 4.3(a) shows the temporal evolution of the sub-grain microstructure represented by the solute (Nb) concentration variation. The simulation was initialized by setting a set of randomly distributed nuclei at the bottom of the calculation domain. Upon solidification, local perturbations applied to the solid-liquid interface promote the growth of numerous small sub-grains along the temperature gradient direction (z axis). Meanwhile, competitive growth among these sub-grains occurs by a series of merging/splitting events, in order to stabilize the system by reducing the interfacial energy. Eventually, the microstructure reaches a steady state where the number and feature of sub-grains remain the same as the solidification advances. Based on the final steady cellular structure, the sub-grain size λ is calculated to be $0.398 \mu\text{m}$ by dividing the number of sub-grains with the width of the simulation box, which is within the reasonable range according to our experiments and the results ($0.27 - 0.73 \mu\text{m}$) reported by Roehling et al. [37]. Moreover, the non-uniform distribution of Nb (also known as microsegregation) is observed. As the solidification proceeds, Nb tends to diffuse from the liquid into solidified sub-grains owing to its higher solubility in solid Ti as compared to that in liquid Ti. Consequently, the Nb-lean/Ti-rich regions are observed at the sub-grain boundary, contributing to the color contrast between sub-grains and sub-grain boundaries in BSE images. It is worth noting that several Ti enriched circular droplets are formed at the sub-grain boundaries, which is also experimentally observed in the BSE images (marked by dashed circles in Figure 4.2). These droplets play minor roles in determining the mechanical response of Ti-35Nb. However, for certain alloy systems such as Ni-Nb, these droplets could transform to secondary phases and significantly affect the mechanical properties of as-fabricated alloys.

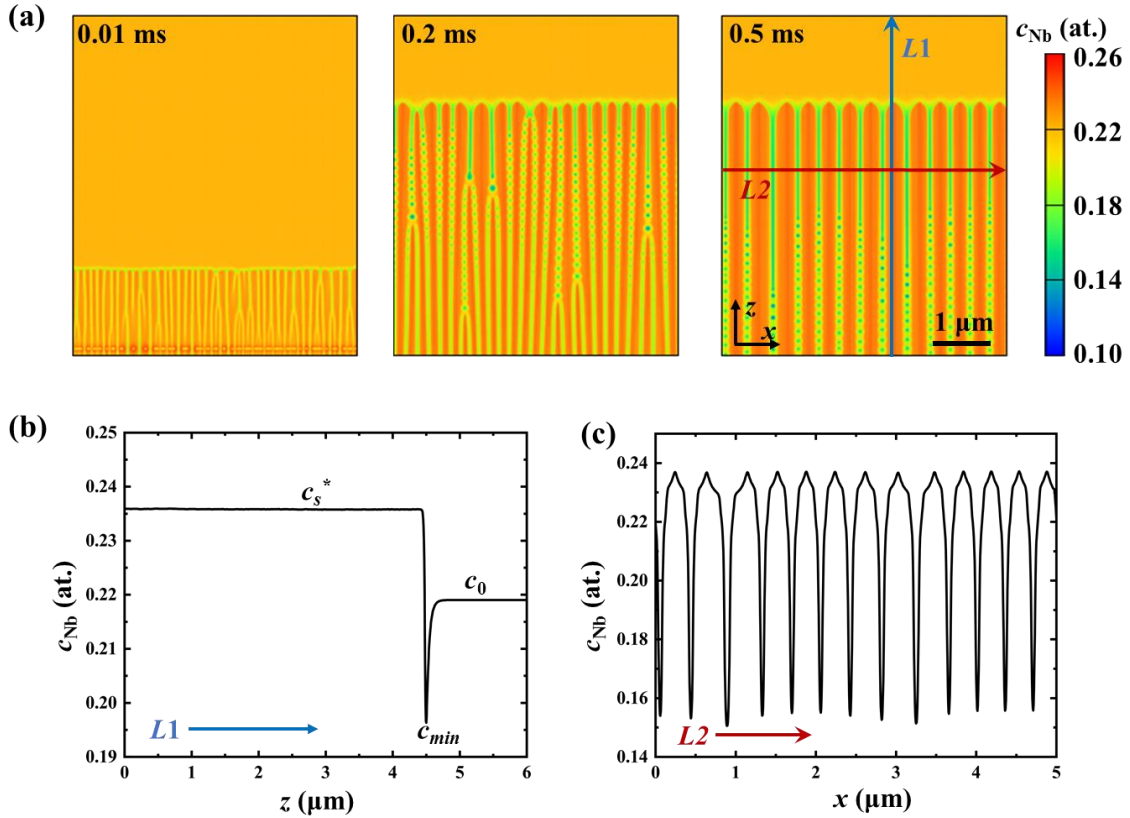


Figure 4.3: PF modeling of the evolution of sub-grain cellular structure, given a cooling rate of 6.9×10^5 K/s and a temperature gradient of 1.4×10^6 K/m: (a) microstructure evolution at different simulation timesteps, represented by Nb concentration, and (b, c) microsegregation of steady-state microstructure, examined by solute concentration variations along lines $L1$ (b) and $L2$ (c).

To further quantify the microsegregation behavior during SLM of Ti-35Nb, the Nb concentration variations along two lines ($L1$ and $L2$ in Figure 4.3(a)) were extracted, as shown in Figure 4.3(b) and (c), respectively. Figure 4.3(b) shows the Nb concentration variation across the sub-grain tip along z axis (line $L1$). It can be seen that the Nb concentration remains a constant value of c_s^* through the sub-grain, and rapidly decreases at the solid-liquid interface due to the diffusion of Nb from liquid into solid until reaching a minimum value of c_{min} . Beyond this point, the Nb concentration increases rapidly and finally reaches the far-field liquid concentration of c_0 . Figure 4.3(c) shows the Nb concentration variation across multiple sub-grains along x axis (line $L2$). The solute microsegregation pattern with a n-shape profile can be observed, where the

regions with higher and lower concentrations represent the sub-grains and sub-grain boundaries, respectively. The average concentration of each region can be calculated by:

$$\bar{c}_{Nb} = \frac{\int_{x_1}^{x_2} c_{Nb}}{x_2 - x_1} \quad (4.16)$$

This information could benefit our understanding of solid solution strengthening in as-fabricated Ti-Nb components. It could also help the design of subsequent ageing treatment if applied, as the region with less β -Ti stabilizer (Nb) is more favorable for the precipitation of α -Ti.

With the understanding of cellular structure growth and its characteristic features, the experimentally observed sub-grain heterogeneity can be elucidated by investigating the site-specific thermal variables including cooling rate V and temperature gradient G within the melt pool. Figure 4.4 presents the thermal modeling results across the transverse cross-section of the melt pool during SLM of Ti-35Nb under a laser power of 210 W and a scanning velocity of 200 mm/s. The developed thermal model was validated on account of matching the melt pool dimensions, as discussed in Section 4.2. The transient temperature distribution in Figure 4.4(b) shows that the temperature gradient direction is perpendicular to the fusion line (T_L isotherm) near the melt pool boundary and gradually changes when approaching the center of melt pool (marked by black arrows). This explains the change of sub-grain growing direction (marked by yellow arrows in Figure 4.2) in regions A2 and A4. Moreover, the site-specific thermal conditions shown in Figure 4.4(c) were extracted from the temperature field using Eq. (4.4), indicating significant variations in thermal variables across a single melt pool. It is observed that the cooling rate decreases from 8.74×10^5 to 2.21×10^5 K/s when moving away from the center to the boundary of the melt pool, whereas the temperature gradient presents an opposite trend with maximum (11.4×10^6 K/m) and minimum (2.05×10^6 K/m) values being at the melt pool boundary and center, respectively. Similar trends were also observed in other studies [26, 38].

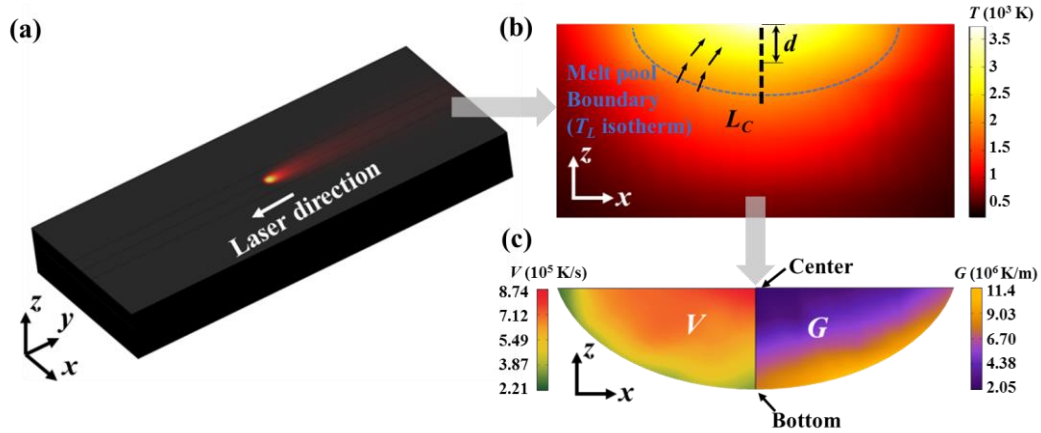


Figure 4.4: Modeling of thermal profiles during SLM of Ti-35Nb at a laser power of 210 W and a scanning velocity of 200 mm/s: (a) global temperature distribution, (b) transient temperature distribution, and (c) spatial variations in cooling rate V and temperature gradient G across the transverse cross-section of the melt pool.

To investigate the heterogenous sub-grain microstructure, PF modeling is conducted using the site-specific thermal inputs within the melt pool, as shown in Figure 4.5(a). It is found that a finer microstructure can be obtained at locations closer to the center of melt pool. The calculation results show that λ increases from 0.24 μm at the center (B3) to 1.32 μm at the bottom (B1) along the depth direction and to 0.96 μm at the edge (B6) along the lateral direction, indicating a significant change in λ across the melt pool. According to the Hunt [39] and Kurz-Fisher [40] models, the sub-grain size λ is inversely proportional to the cooling rate and temperature gradient by $\lambda \propto G^{-a}V^{-b}$ ($a = b = 0.25$). When approaching the center of the melt pool, the increased cooling rate leads to the decrease of λ while the decreased temperature gradient leads to the increase of λ . However, during the rapid solidification, the cooling rate could deliver a greater impact on λ as compared to the temperature gradient ($a > b$) [22]. Therefore, finer microstructure presents near the center of melt pool while coarser microstructure presents at the melt pool boundary. Such phenomenon was also identified in AM of AlSi10Mg [36], Ti-Al [8] and Ni-Nb [38] alloys. Additional simulations performed at A1-A4 regions (in Figure 4.2)

present the sub-grain size of 0.47, 0.63, 0.88, and 1.25 μm , respectively, showing a good agreement with experimental measurements. The small discrepancy could be attributed to the misorientation between temperature gradient and actual grain growth direction [8].

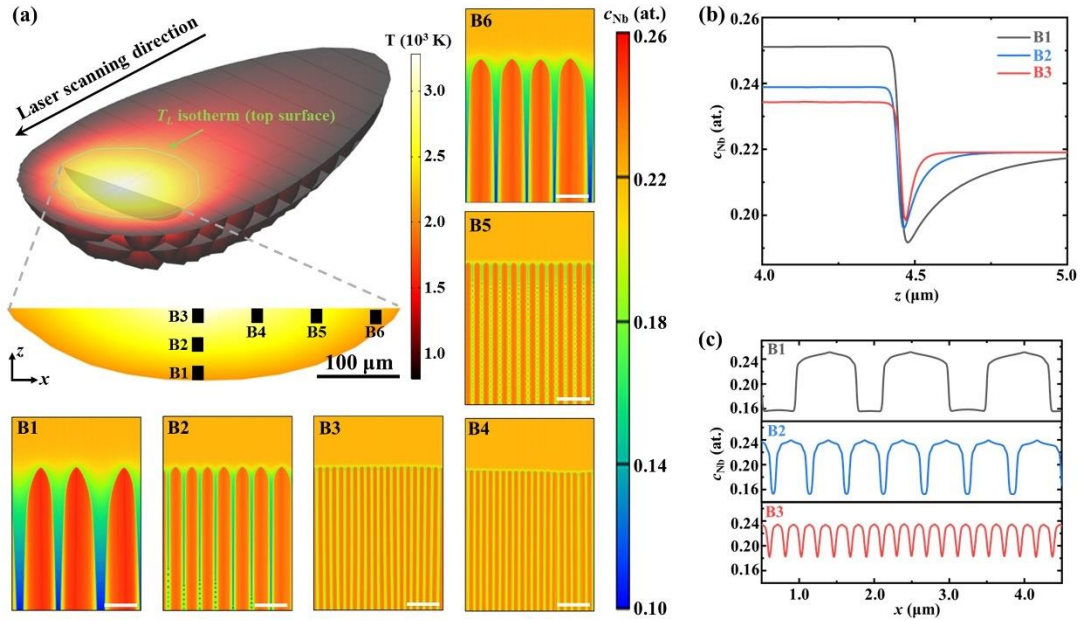


Figure 4.5: The spatial variation in the sub-grain microstructure during SLM of Ti-35Nb with a laser power of 210W and a scanning velocity of 200 mm/s. (a) PF modeling results at multiple locations within a single melt pool. The white scale bars represent 1 μm . (b, c) Nb concentration variations along line L1 (b) and L2 (c), respectively, for locations B1, B2 and B3 in Figure 4.5(a).

In addition to the heterogeneity in the sub-grain size, it is noted that the microsegregation behavior also differs at varying locations within the melt pool. Figure 4.5(b) and (c) compares Nb concentration profiles at different locations (B1, B2, B3) along lines L1 and L2, respectively. It is observed that the degree of Nb microsegregation at the solid-liquid interface ($c_s^* - c_{\text{min}}$) decreases when moving towards the center of the melt pool. It is also observed that the n-shape concentration profiles become finer and closer when approaching the center. Both observations indicate a weaker microsegregation effect at locations closer to the center, as the solute has shorter time to re-distribute at a higher cooling rate. Furthermore, according to Eq. (4.16), it can

be calculated that the average Nb concentration within the sub-grain increases by only 1.4 at.% from 23.0 at.% at the top (B3) to 24.4 at.% at the bottom (B1). The natural question is whether this difference in microsegregation will contribute to the variation in micromechanical response due to the solid solution hardening effect. According to the work of Qian et al. [41], for SLM-produced Ti-Nb alloys, a significant increase of Nb concentration from 25 to 45 at.% led to a 19.9% enhancement in the surface strength from 297 to 356 VHN. Therefore, it is reasonable to claim that in our study, the small increase in Nb concentration from 23.0 (B3) to 24.4 (B1) at.% might induce a limited hardening effect as comparing the top region to the bottom region. In other words, the spatial variation in micromechanical response could mainly arise from the change of the sub-grain size across the melt pool rather than that of the microsegregation.

Heterogeneous microstructure as affected by processing parameters

SLM has a robust capability in tuning processing parameters to effectively change the complex thermal conditions, allowing us to tailor the site-specific microstructure to obtain desired properties. It is of great importance to establish the process-microstructure relationship and evaluate the effectiveness of tuning SLM parameters on the heterogeneous sub-grain microstructure. Among all SLM processing variables, the laser power and scanning velocity play the dominant roles on determining the thermal conditions induced by laser-matter interaction. Prior to extracting thermal conditions during SLM of Ti-35Nb, the modeling predictions are compared with experimental results in terms of melt pool dimensions under varying processing conditions, as shown in Figure 4.6. The inset images are the simulated and experimental transverse cross-sections of the melt pool under a laser power of 210W and a scanning velocity of 200 mm/s, showing a similar morphology. The width and depth of the melt pool were obtained by measuring the maximum distance across the melt pool along lateral and vertical directions, respectively. It is found that both experimental measurements and modeling results

demonstrate similar qualitative trends of melt pool width and depth as affected by the laser power or scanning velocity. Moreover, the predicted melt pool dimensions at varying processing conditions show a good consistency with the experimental measurements, which indicates that the established thermal model is capable of providing reliable thermal inputs for PF modeling.

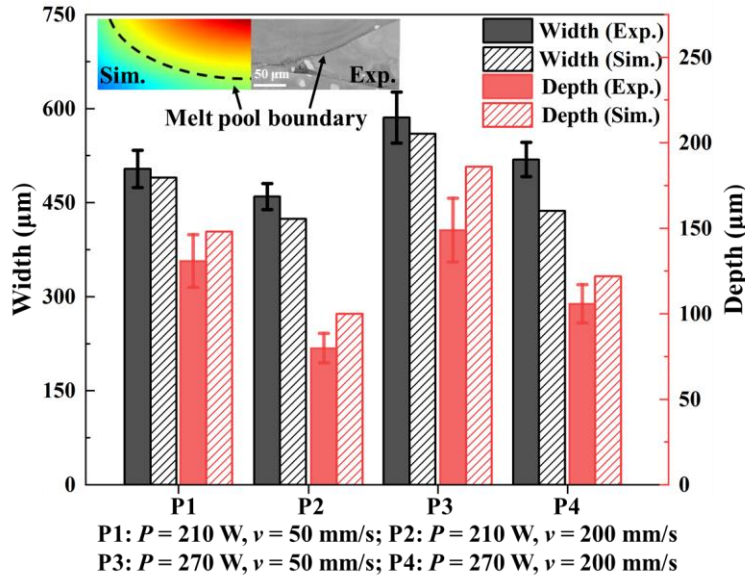


Figure 4.6: Melt pool dimensions under four groups of processing parameters (P1: 210W, 50 mm/s; P2: 210W, 200 mm/s; P3: 270W, 50 mm/s; P4: 270W, 200mm/s). Inset image shows simulated and experimental cross-section morphologies of the melt pool under processing condition P2.

The calculated thermal inputs as affected by SLM processing parameters, including laser power P and scanning velocity v , are present in Figure 4.7. The thermal data were extracted from locations on the centerline L_C in Figure 4.4 (described by the distance d from the center of the melt pool) to clearly demonstrate the trends. As shown in Figure 4.7(a) and (b), given a scanning velocity of 200 mm/s, the cooling rate at a fixed location (same d) does not show a clear trend as affected by the laser power in the selected range. In contrast, the temperature gradient at a fixed location generally increases with the increase of laser power. Such increase becomes more significant at locations closer to the bottom of the melt pool. Additionally, a lower laser power leads to a larger local variation in the temperature gradient along centerline L_C . For instance, as d

increases from 30 to 50 μm , the temperature gradient increases by 17.5% from 2.91×10^6 to 3.42×10^6 K/m with $P = 270$ W while by 37.7% from 5.65×10^6 to 7.78×10^6 K/m with $P = 180$ W. Figure 4.7(c) and (d) demonstrate that, given a laser power of 210 W, the cooling rate and temperature gradient at a fixed location both increase by increasing the scanning velocity. The increase of cooling rate caused by a faster scanning velocity becomes less significant at locations closer to the bottom of the melt pool, whereas that of temperature gradient is similar at all locations. In addition, a higher scanning velocity generally leads to a larger local variation in cooling rate along L_C . For example, with d increasing from 50 to 90 μm , the cooling rate decreases by 58.6% from 5.65×10^5 to 2.34×10^5 K/s with $v = 200$ mm/s while by 27.0% from 1.85×10^5 to 1.35×10^5 K/s with $v = 50$ mm/s.

With the inputs of thermal variables, the heterogenous sub-grain microstructure in terms of site-specific sub-grain size λ as affected by SLM processing parameters are simulated, as shown in Figure 4.8. In this study, the melt pool area was divided into small discrete regions with dimensions of $20 \times 20 \mu\text{m}^2$, and the average thermal variables of each region were applied as inputs for PF modeling to construct maps showing the λ distribution across the melt pool. Figure 4.8(a) shows the distribution map of λ within the melt pool in SLM-produced Ti-35Nb under a laser power of 210W and a scanning velocity of 50 mm/s. It is found that λ ranges from 0.31 to 1.62 μm , with the minimum and maximum values being at the center and boundary of the melt pool, respectively. When increasing the scanning velocity to 200 mm/s, a lower overall variation in λ (0.24 - 1.32 μm) within a smaller melt pool can be observed, as shown in Figure 4.8(b). Such reduction in the overall variation of λ could also be achieved by reducing the laser power. Note that in this study, the overall variation refers to the variation across the entire melt pool, and the local variation refers to the variation over a small distance of site-specific computational regions.

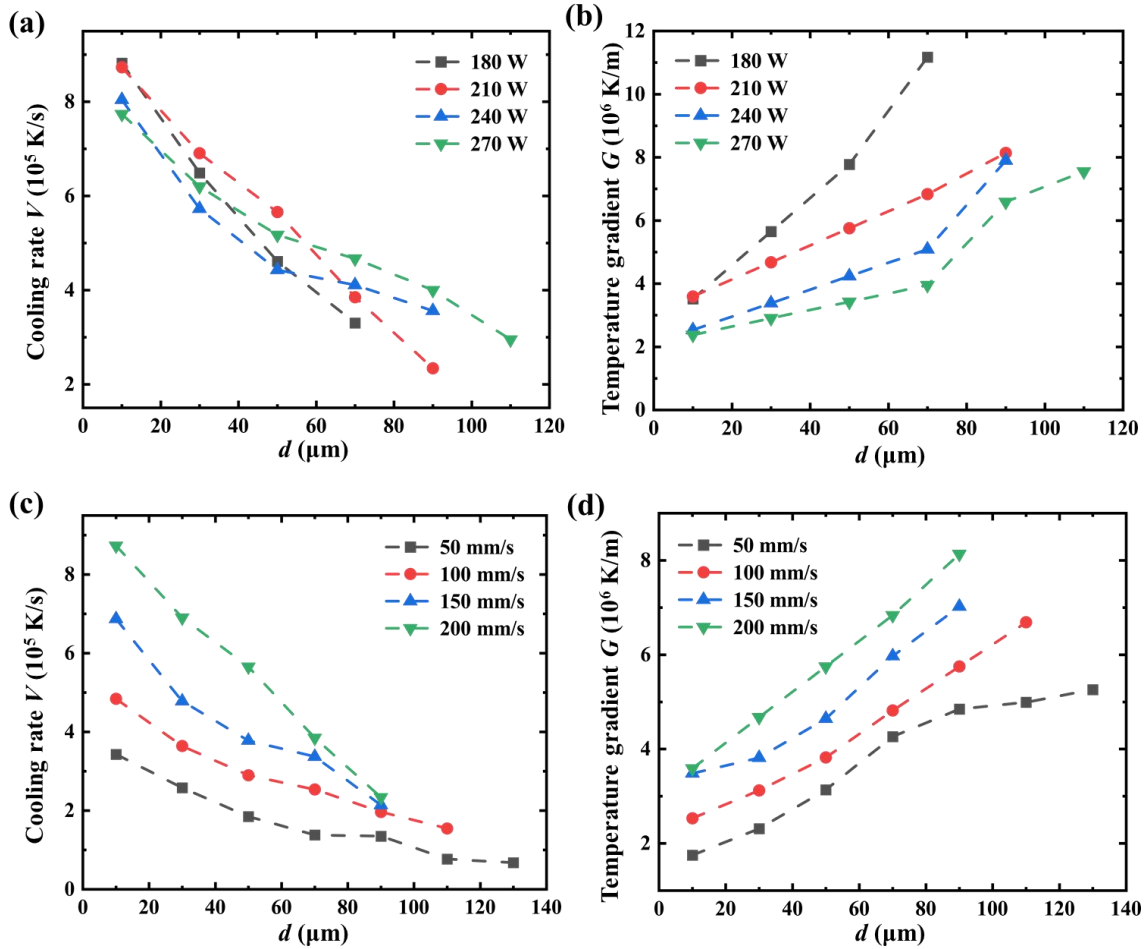


Figure 4.7: The calculated site-specific cooling rate V and temperature gradient G as affected by laser processing parameters during SLM of Ti-35Nb. (a) V and (b) G along the depth direction under various laser power (180 - 270 W) and a fixed scanning velocity of 200 mm/s. (c) V and (d) G along the depth direction under various scanning velocities (50 - 200 mm/s) and a fixed laser power of 210 W.

More details regarding the effects of individual processing parameters on the heterogeneity in the sub-grain size are demonstrated in Figure 4.8(c) and (d). Figure 4.8(c) shows the influence of laser power on the variation in λ along the centerline L_C at a constant scanning velocity of 200 mm/s. It is found that given a fixed location, λ decreases with the increase of laser power. Such reduction in λ becomes more significant at locations closer to the bottom of melt pool. For example, as the laser power increases from 210 to 270 W, λ decreases by 28.6% from 0.56 to 0.40 μm at the location where $d = 50 \mu\text{m}$ while by 40.7% from 0.81 to 0.48 μm at

the location where $d = 70 \mu\text{m}$. These observations are consistent with the temperature gradient variation in Figure 4.7(d), as the cooling rate is less sensitive to the laser power in the selected range as compared to the temperature gradient. Moreover, the local variation of λ over the same distance decreases with the increase of laser power. For instance, given two site locations ($d = 30 \mu\text{m}$ and $d = 70 \mu\text{m}$), λ varies from 0.41 to 0.81 μm (0.4 μm difference) at a laser power of 210 W while from 0.30 to 0.48 μm (0.18 μm difference) at a laser power of 270 W. Similar observations can be found in Figure 4.8(d) showing the influence of scanning velocity on λ at a constant laser power of 210 W. For a fixed location, λ generally decreases with the increase of scanning velocity due to the increases in cooling rate and temperature gradient. Such reduction in λ becomes more significant at locations closer to the bottom of melt pool, which is mainly attributed to the lower temperature gradient (difference in cooling rate becomes smaller). However, the local variation over the same distance only slightly decreases with the increase of scanning velocity. For instance, given two site locations ($d = 30 \mu\text{m}$ and $d = 70 \mu\text{m}$), λ varies from 0.48 to 0.91 μm (0.43 μm difference) at a scanning velocity of 100 mm/s and from 0.41 to 0.81 μm (0.4 μm difference) at a scanning velocity of 200 mm/s. Based on the simulation results from Figure 4.8, it can be concluded that: i) the laser power plays a more significant role in determining heterogeneity as compared to the scanning velocity, i.e., tuning the laser power is more effective in controlling the heterogeneity in sub-grain microstructure than tuning the scanning velocity; ii) a lower laser power or a higher scanning velocity leads to a microstructure with a smaller overall variation in λ across the melt pool, but a larger local variation in λ over the same distance. To further verify the proposed framework in investigating the process-microstructure relationship, experimental measurements and simulation results were compared

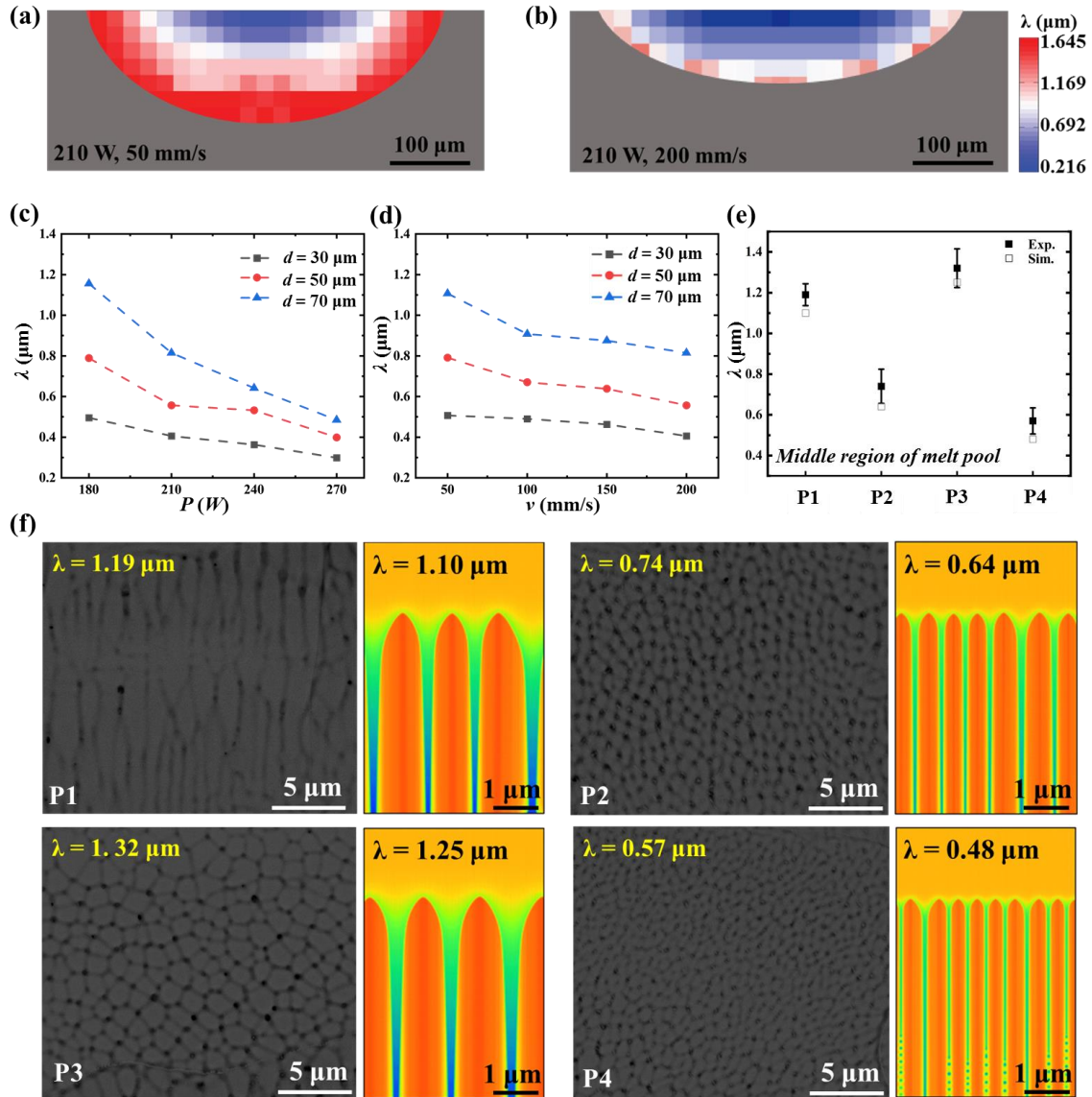


Figure 4.8: Variations in the sub-grain size λ across the melt pool under different SLM parameters: (a, b) the distribution maps of λ under scanning velocities of 50 mm/s and 200 mm/s at a constant laser power of 210 W, respectively; (c, d) the variation in λ as affected by the laser power at a constant scanning velocity of 200 mm/s (c) and by the scanning velocity at a constant laser power of 210 W (d). Comparison between modeling and experimental results for sub-grain cellular structure at the middle region of melt pool under varying processing conditions: (e) comparisons regarding sub-grain size; (f) BSE images and simulated microstructure.

under different laser powers and scanning velocities. Figure 4.8(e) demonstrates the comparison results regarding the sub-grain size near the middle region of melt pool under P1-P4 processing conditions. It is found that the computational framework shows great potentials in predicting the relationship between processing parameters and site-specific sub-grain microstructure evolution.

For instance, given a laser power of 270 W and a scanning velocity of 50 mm/s (P3 condition), the site-specific sub-grain size at the middle region is measured to be 1.32 μm according to the BSE image in Figure 4.8(f), while the PF modeling result under corresponding thermal conditions shows a similar value of 1.25 μm .

Heterogeneity in micromechanical response

To investigate the impact of experimentally observed heterogeneous microstructure on the micromechanical response, we performed Vickers hardness testing on regions with different sub-grain sizes. The microhardness testing was conducted using a low load (25 gf) to obtain small indentation sizes (smaller than 20 μm) within each individual grain, in order to measure the micromechanical response for different sub-grain cellular structure. To investigate the microstructure-property relationship, the as-measured microhardness value as a function of the sub-grain size is depicted in Figure 4.9, showing that the surface strength gradually increases with the decrease of sub-grain size. For instance, the microhardness increases from 325.7 to 302.2 VHN as the sub-grain size increases from 0.9 to 1.5 μm . We also noticed that the center of melt pool under varying processing conditions show similar microhardness values of ~ 350 VHN.

The experimental measurements can be integrated with simulations to reveal the microstructure-property relationship at the sub-grain scale and facilitate the understanding of micromechanical response of SLM-fabricated components. To this end, the CP modeling was firstly employed to investigate the micromechanical response of SLM-produced Ti-35Nb using sub-grain microstructures as the inputs. Prior to the investigation, the CP model was calibrated with monotonic tensile tests using the experimental data from Ref. [41]. The obtained CP parameters were listed in Table 4.3. CP simulations were performed for different sub-grain cellular structures with λ ranging from 0.4 - 1.2 μm . Figure 4.10(a) depicts the calculated stress-

strain curves. It is found that the ultimate tensile strength (UTS) increases with the decrease of sub-grain size λ . For instance, the simulated UTS decreases from 1146 to 889 MPa by increasing λ from 0.4 to 1.2 μm . This phenomenon can be explained by the well-known Hall-Petch law, as shown in Figure 4.10(b). Regression analysis on the strength and sub-grain size yield a linear relation as: $\text{UTS} = 553.58 + 379.31 * \lambda^{-1/2}$.

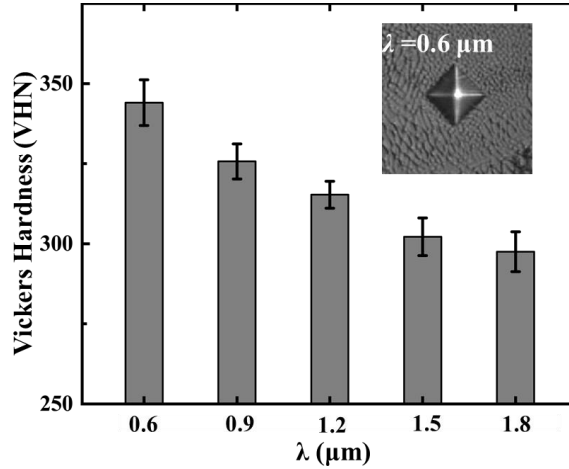


Figure 4.9: Experimental results of microhardness as affected by the sub-grain size.

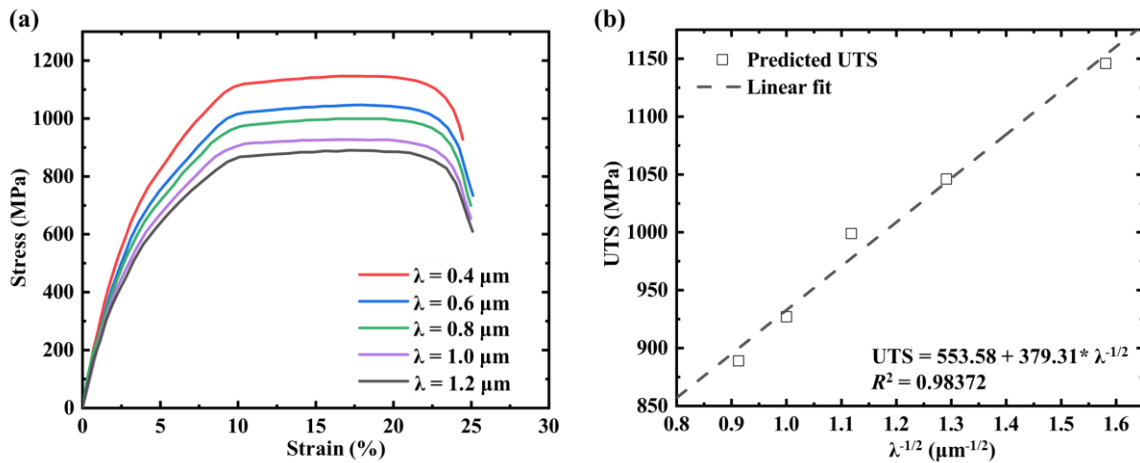


Figure 4.10: Simulated micromechanical response as affected by the sub-grain size λ . (a) Stress-strain curves for λ ranging from 0.4 - 1.2 μm . (b) The linear relation between UTS and the inverse square root of sub-grain size $\lambda^{-1/2}$.

In addition, the micromechanical fields of stress and strain distributions were examined for further understanding of micromechanical response as influenced by the sub-grain cellular

structures (as shown in Figure 4.11). Results indicate that neither the stress concentration at the sub-grain boundaries nor the intergranular deformation is observed, which was attributed to the loads applying along the sub-grain length direction. Similar observation was reported in the work of Liu et al. [42] for a polycrystalline structure of AM-produced Ti-6Al-4V.

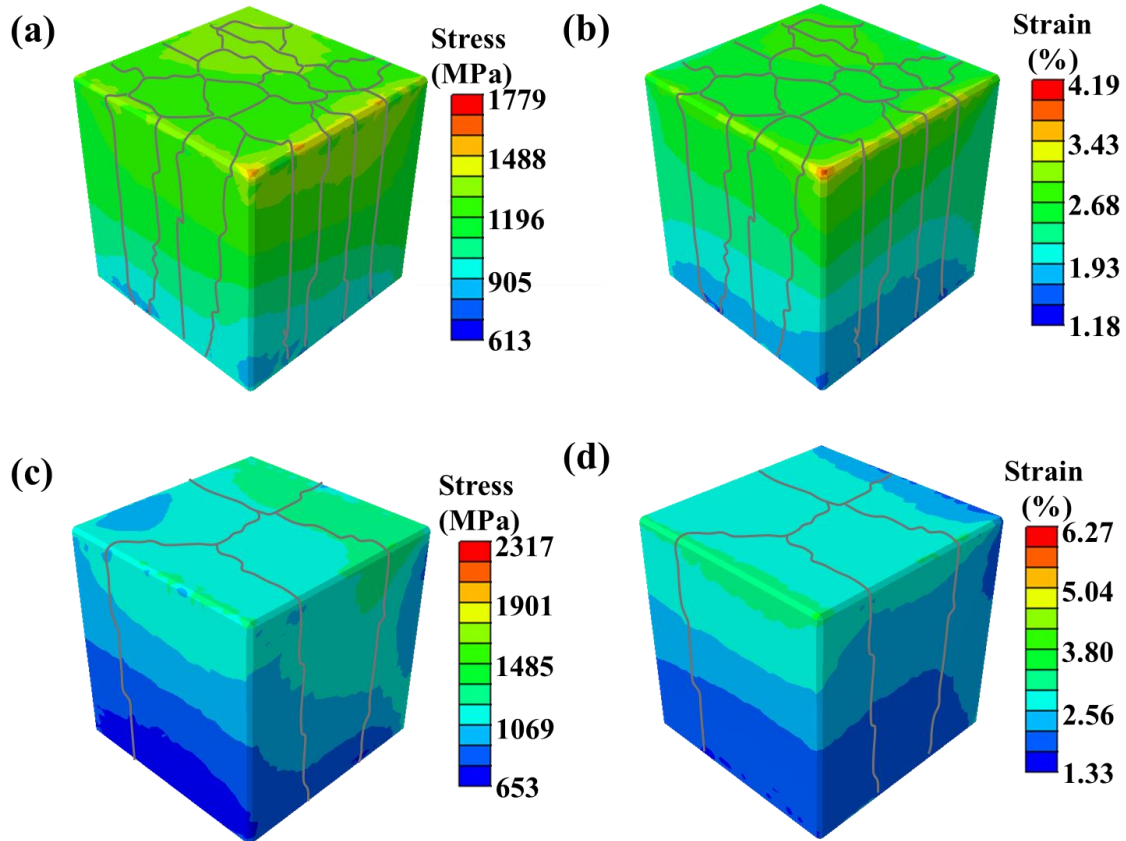


Figure 4.11: Micromechanical fields for different sub-grain cellular structures. (a) Stress and (b) strain fields for the microstructure with a sub-grain size of $0.4 \mu\text{m}$. (c) Stress and (d) strain fields for the microstructure with a sub-grain size of $0.8 \mu\text{m}$.

More importantly, in comparison to the sub-grain cellular structure with $\lambda = 0.8 \mu\text{m}$, the structure with $\lambda = 0.4 \mu\text{m}$ shows less inhomogeneous distributions of stress and deformation. It is noted that the stress or strain gradually decreases inside the structure, exhibiting a layered effect on the micromechanical fields. Such layered effect is found to be more significant with the increase of the sub-grain size. In other words, a finer sub-grain microstructure benefits the load

spreading into a larger volume of the material, hence, more regions bear the stress with smaller deformation. In contrast, a coarser sub-grain microstructure experienced a larger stress and deformation in certain regions. For instance, the maximum stress reaches 1779 MPa and 2317 MPa inside the structures with $\lambda = 0.4 \mu\text{m}$ and $0.8 \mu\text{m}$, respectively. Consequently, a finer sub-grain microstructure leads to a better stress distribution and resistance to the material deformation towards a higher strength.

To further evaluate the micromechanical response across the melt pool, the predicted material strength is correlated to the microhardness H, as shown in Figure 4.12. Figure 4.12(a) demonstrates the correlation between UTS and H using existing experimental data from literatures related to Ti-35Nb or similar alloys [41, 43-50]. Regression analysis of the data points gives a good linear relationship between UTS and H with a high R^2 value, indicating that the estimation of microhardness H for a given UTS can be achieved within a reasonable range. Subsequently, integrated with the simulated correlation between UTS and sub-grain size in Figure 4.10(b), the calculated microhardness as affected by the sub-grain size can be obtained. Figure 4.12(b) compares the experimental (black) and modeling (red) results regarding microstructure-property relationship at the sub-grain scale, represented by the microhardness H as a function of $\lambda^{-1/2}$. A relatively consistent linear relationship can be observed, indicating that the CP model is capable of predicting micromechanical response for Ti-35Nb fabricated by SLM. In addition, it is worth mentioning that the experimental data from both our experiments and existing literatures indicate that the site-specific microhardness increases with the decrease of λ until a saturation point of ~ 350 VHN. The saturated strengthening effect could be attributed to the fact that the linear Hall-Petch relationship does not apply to all sub-grain sizes. In the work of Fu et al. [51] and Kimura et al. [52], it was stated that such linear relationship is generally

found for the grain size larger than $0.5 \mu\text{m}$. Beyond this point, it is often observed that the strength slowly increases or reaches a saturation point with the decrease of grain size. In our simulation, given a cellular structure with $\lambda = 0.5 \mu\text{m}$, the corresponding microhardness is estimated to be $\sim 356 \text{ VHN}$ for Ti-35Nb, which is close to the experimental observed saturation point.

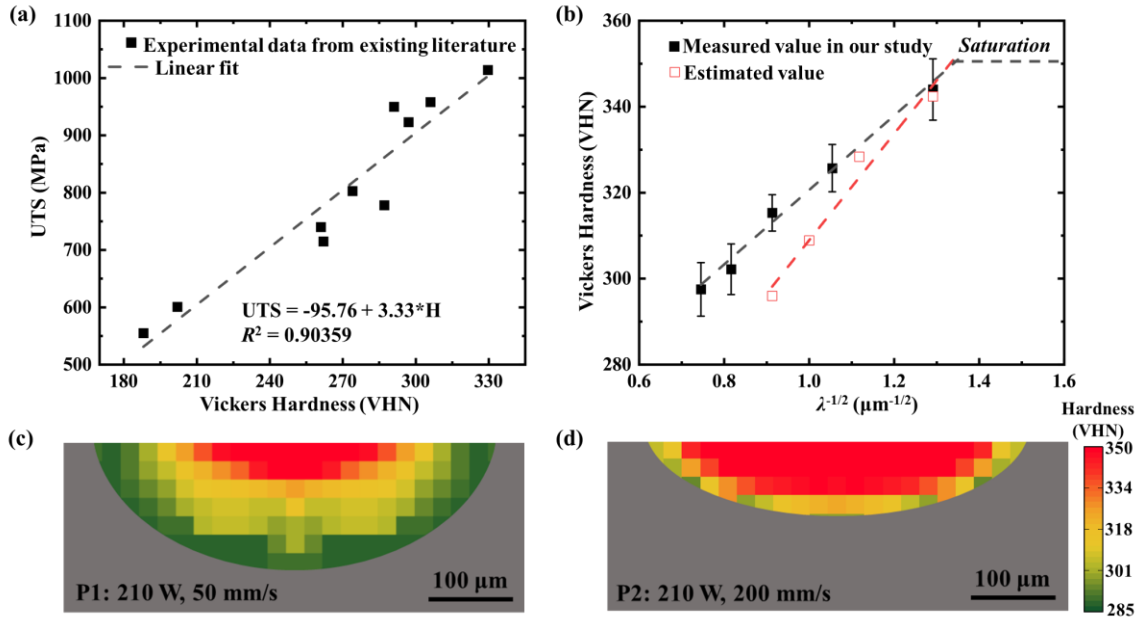


Figure 4.12: Microhardness distribution as affected by processing parameters. (a) The experimental correlation between UTS and microhardness H for Ti-35Nb based on existing data points from literatures. (b) The experimental and modeling correlations between microhardness and square root of sub-grain size $\lambda^{-1/2}$, showing a similar linear relationship. (c, d) The maps of site-specific microhardness across the melt pool under $P = 210 \text{ W}$, $v = 50 \text{ mm/s}$ (c) and $P = 210 \text{ W}$, $v = 200 \text{ mm/s}$ (d).

Figure 4.12(c) and (d) demonstrate the micromechanical response represented by microhardness across the melt pool under varying processing conditions by integrating the correlation between H and λ in Figure 4.12(b) and the distribution map of λ in Figure 4.8. Note that we imposed a microhardness value of 350 VHN for certain discrete regions (generally near the center of the melt pool) where the estimated microhardness is above this value, in consideration of the saturation phenomenon. As observed in Figure 4.12, the microhardness

generally increases when moving towards the center of melt pool until reaches the maximum value, owing to the finer sub-grain microstructure. This was also experimentally observed in SLM of Ti-24Nb-4Zr-8Sn [9]. In addition, it is found that the melt pool produced at a lower scanning velocity (50 mm/s) yields a larger overall variation in microhardness (286 - 350 VHN), as compared to the one produced at a higher scanning velocity (200mm/s, 296 - 350 VHN). This is caused by the sub-grain size distribution and the melt pool dimensions as discussed in Subsection 4.2. The maximum microhardness of each melt pool remains similar values due to the saturation phenomenon, however, the minimum value decreases at a lower scanning velocity due to the larger sub-grain size at the bottom of the melt pool. Moreover, SLM with a higher scanning velocity produces the melt pool with a higher fraction of relatively hard regions and less heterogeneous micromechanical response. On basis of this, it can be deduced that a lower laser power would lead to similar observations. Additionally, in comparison to tuning the scanning velocity, the higher effectiveness of tuning the laser power in tailoring the microstructure could lead to a similar effect in controlling the micromechanical response. It is worth noting that the heterogeneity in micromechanical response could lead to a ‘hard-wrap-soft’ phenomenon that may contribute to a better component performance. To be specific, during tensile test of SLM-produced components, the soft regions plastically deform first but constrained by the hard regions. The plasticity mismatch between the soft and hard regions induces the generation of geometrically necessary dislocations (GNDs) at the soft-hard region interfaces, leading to the formation of long-range back stress. As the strain increases, the back stress increases with GNDs piling-up at the interfaces. It has been reported [2, 53] that such back stress may not only enhance the global strength due to strengthened soft regions, but also improve the ductility due to the enhanced strain hardening. Consequently, it is envisioned that a

better combination of strength and ductility could be achieved by producing the heterogeneity in site-specific microstructure/property. Our investigations on the process-microstructure-property relationship at the sub-grain scale can be applied to thoroughly understand and control the heterogeneity in sub-grain cellular structure and micromechanical response to fabricate high-performance components by AM.

Conclusion

In this study, the heterogeneities in the sub-grain microstructure and micromechanical response in SLM-fabricated Ti-35Nb were investigated through an integrated computational and experimental effort. The underlying mechanism responsible for such heterogeneities were studied. The process-microstructure-property relationship at the sub-grain scale was investigated. The roles of individual processing parameters on the spatial control of these heterogeneities were evaluated. The major findings of this research are summarized as follows:

(1) SLM of Ti-35Nb exhibited considerable heterogeneity in sub-grain cellular structure due to the spatial variations in thermal conditions. Both the sub-grain size and level of microsegregation increased at locations closer to the bottom of melt pool, due to the decreased cooling rate despite the increased temperature gradient. However, results indicated that the sub-grain size showed a more significant variation as compared to the microsegregation. Given a laser power of 210 W and a scanning velocity of 200 mm/s, the sub-grain size varied from 0.24 to 1.32 μm whereas the solute concentration within individual sub-grains ranged from 23.0 to 24.4 at.%.

(2) In comparison to the scanning velocity, the laser power played a more significant role on determining the heterogeneity in sub-grain microstructure in SLM of Ti-35Nb. In addition, a lower laser power or a higher scanning velocity resulted in a larger local variation in the sub-grain size over a small distance, but a smaller overall variation due to the reduced dimensions of the melt pool.

(3) Heterogeneity in micromechanical response was observed for SLM-produced Ti-35Nb, with the maximum material strength being near the melt pool center and the minimum being near the melt pool boundary. This was inherently related to the variations in the sub-grain size.

(4) Given a lower laser power or a higher scanning velocity, the minimum microhardness within the melt pool increased due to the decreased sub-grain size, whereas the maximum microhardness values were the same for all cases due to the saturated strengthening effect (~350 VHN for SLM-fabricated Ti-35Nb). In addition, a lower laser power or a higher scanning velocity led to less heterogeneity in micromechanical response and a higher fraction of harder regions.

This work demonstrates the great potential of the proposed ICME-based framework in comprehensively investigating the process-microstructure-property relationship at the sub-grain scale during SLM of metallic materials. For the future efforts, we will extend the PF model and CP model to the macro grain scale. The PF model will be employed to simulate the columnar grain growth during SLM by considering multiple thermal loading cycles. The CP model will be applied to polycrystalline material with varying sub-grain microstructure to elucidate the influence of hierarchical structure (grains and sub-grains) on the global mechanical performance.

Reference

- [1] P. Kürsteiner, M.B. Wilms, A. Weisheit, B. Gault, E.A. Jägle, D. Raabe. High-strength Damascus steel by additive manufacturing. *Nature*, 582(7813), (2020), pp. 515-519.
- [2] G. Karthik, H.S. Kim. Heterogeneous aspects of additive manufactured metallic parts: a review. *Metals and Materials International*, (2021), pp. 1-39.
- [3] Z. Wang, K. Guan, M. Gao, X. Li, X. Chen, X. Zeng. The microstructure and mechanical properties of deposited-IN718 by selective laser melting. *J. Alloys Compd.*, 513, (2012), pp. 518-523.
- [4] M.-S. Pham, B. Dovgvy, P.A. Hooper, C.M. Gourlay, A. Piglione. The role of side-branching in microstructure development in laser powder-bed fusion. *Nat. Commun.*, 11(1), (2020), pp. 1-12.

- [5] X. Liu, C. Zhao, X. Zhou, Z. Shen, W. Liu. Microstructure of selective laser melted AlSi10Mg alloy. *Mater. Des.*, 168, (2019), p. 107677.
- [6] Y.M. Wang, T. Voisin, J.T. McKeown, J. Ye, N.P. Calta, Z. Li, Z. Zeng, Y. Zhang, W. Chen, T.T. Roehling. Additively manufactured hierarchical stainless steels with high strength and ductility. *Nat. Mater.*, 17(1), (2018), pp. 63-71.
- [7] X. Zhang, D. Li, Y. Liao, Y. Zheng. Three-Dimensional Characterization of Selective Laser Melted Graphene Oxide-Reinforced Ti-48Al-2Cr-2Nb Alloy. *JOM*, (2021), pp. 1-9.
- [8] X. Zhang, B. Mao, L. Mushongera, J. Kundin, Y. Liao. Laser powder bed fusion of titanium aluminides: An investigation on site-specific microstructure evolution mechanism. *Mater. Des.*, 201, (2021), p. 109501.
- [9] C.L. Yang, Z.J. Zhang, S.J. Li, Y.J. Liu, T.B. Sercombe, W.T. Hou, P. Zhang, Y.K. Zhu, Y.L. Hao, Z.F. Zhang, R. Yang. Simultaneous improvement in strength and plasticity of Ti-24Nb-4Zr-8Sn manufactured by selective laser melting. *Materials & Design*, 157, (2018), pp. 52-59.
- [10] Y.J. Liu, Y.S. Zhang, L.C. Zhang. Transformation-induced plasticity and high strength in beta titanium alloy manufactured by selective laser melting. *Materialia*, 6, (2019), p. 100299.
- [11] S.A.H. Motaman, F. Roters, C. Haase. Anisotropic polycrystal plasticity due to microstructural heterogeneity: a multi-scale experimental and numerical study on additively manufactured metallic materials. *Acta Mater.*, 185, (2020), pp. 340-369.
- [12] K. Dai, L. Shaw. Finite element analysis of the effect of volume shrinkage during laser densification. *Acta materialia*, 53(18), (2005), pp. 4743-4754.
- [13] M. Frewin, D. Scott. Finite element model of pulsed laser welding. *WELDING JOURNAL-NEW YORK-*, 78, (1999), pp. 15-s.
- [14] X. Zhang, Y. Liao. A phase-field model for solid-state selective laser sintering of metallic materials. *Powder technology*, 339, (2018), pp. 677-685.
- [15] H. Park, M. Ansari, Numerical investigation and an effective predicting system on the Selective Laser Melting (SLM) process with Ti6Al4V alloy, *IOP Conference Series: Materials Science and Engineering*, IOP Publishing, 2018, p. 042046.
- [16] V. Fallah, A. Khajepour, M. Alimardani, A numerical-experimental investigation on the deposition of Ti-45Nb on mild steel using automated laser fabrication process, *International Congress on Applications of Lasers & Electro-Optics*, Laser Institute of America, 2008, p. 501.
- [17] A. Olleak, Z. Xi. Finite element modeling of the selective laser melting process for Ti-6Al-4V. *Solid freeform fabrication 2018: Proceedings of the 29th Annual International*, (2018), pp. 1710-1720.

- [18] S. Singaravelu, J. Klopff, G. Krafft, M. Kelley. Laser nitriding of niobium for application to superconducting radio-frequency accelerator cavities. *Journal of Vacuum Science & Technology B, Nanotechnology and Microelectronics: Materials, Processing, Measurement, and Phenomena*, 29(6), (2011), p. 061803.
- [19] A. Hussein, L. Hao, C. Yan, R. Everson. Finite element simulation of the temperature and stress fields in single layers built without-support in selective laser melting. *Materials & Design*, 52, (2013), pp. 638-647.
- [20] P. Tan, F. Shen, B. Li, K. Zhou. A thermo-metallurgical-mechanical model for selective laser melting of Ti6Al4V. *Mater. Des.*, 168, (2019), p. 107642.
- [21] J. Kundin, L. Mushongera, H. Emmerich. Phase-field modeling of microstructure formation during rapid solidification in Inconel 718 superalloy. *Acta Materialia*, 95, (2015), pp. 343-356.
- [22] J. Kundin, A. Ramazani, U. Prah, C. Haase. Microstructure Evolution of Binary and Multicomponent Manganese Steels During Selective Laser Melting: Phase-Field Modeling and Experimental Validation. *Metallurgical and Materials Transactions A*, 50(4), (2019), pp. 2022-2040.
- [23] J. Kundin, J.L.L. Rezende, H. Emmerich. Phase-Field Modeling of the Coarsening in Multi-component Systems. *Metall. Mater. Trans. A*, 45(2), (2013), pp. 1068-1084.
- [24] J. Kundin, J.L.L. Rezende, H. Emmerich. Phase-field modeling of the coarsening in multi-component systems. *Metall. Mater. Trans. A*, 45(2), (2014), pp. 1068-1084.
- [25] J. Kundin, I. Steinbach. Comparative study of different anisotropy and potential formulations of phase-field models for dendritic solidification. *Comput. Mater. Sci.*, 170, (2019), p. 109197.
- [26] V. Fallah, M. Amoozraei, N. Provatas, S.F. Corbin, A. Khajepour. Phase-field simulation of solidification morphology in laser powder deposition of Ti-Nb alloys. *Acta Materialia*, 60(4), (2012), pp. 1633-1646.
- [27] M.A. Groeber, M.A. Jackson. DREAM. 3D: a digital representation environment for the analysis of microstructure in 3D. *Integr. Mater. Manuf. Innovation*, 3(1), (2014), pp. 56-72.
- [28] M. Erwig. The graph Voronoi diagram with applications. *Networks: An International Journal*, 36(3), (2000), pp. 156-163.
- [29] E.H. Lee. Elastic-plastic deformation at finite strains. (1969),
- [30] W. Ye, J. Akram, L.T. Mushongera. Fatigue Behavior of Additively Manufactured IN718 with Columnar Grains. *Adv. Eng. Mater.*, 23(3), (2021), p. 2001031.
- [31] R.D. McGinty. Multiscale representation of polycrystalline inelasticity. Georgia institute of technology (2001).

- [32] P.J. Armstrong, C. Frederick. A mathematical representation of the multiaxial Bauschinger effect. Central Electricity Generating Board [and] Berkeley Nuclear Laboratories ... (1966).
- [33] U. Kocks, T. Brown. Latent hardening in aluminum. *Acta Metallurgica*, 14(2), (1966), pp. 87-98.
- [34] P. Jackson, Z. Basinski. Latent hardening and the flow stress in copper single crystals. *Can. J. Phys.*, 45(2), (1967), pp. 707-735.
- [35] C.R. Houck, J. Joines, M.G. Kay. A genetic algorithm for function optimization: a Matlab implementation. *Ncsu-ie tr*, 95(09), (1995), pp. 1-10.
- [36] P. Van Cauwenbergh, V. Samaee, L. Thijs, J. Nejezchlebová, P. Sedlák, A. Iveković, D. Schryvers, B. Van Hooreweder, K. Vanmeensel. Unravelling the multi-scale structure–property relationship of laser powder bed fusion processed and heat-treated AlSi10Mg. *Sci. Rep.*, 11(1), (2021), pp. 1-15.
- [37] J.D. Roehling, A. Perron, J.-L. Fattebert, T. Haxhimali, G. Guss, T.T. Li, D. Bober, A.W. Stokes, A.J. Clarke, P.E. Turchi. Rapid solidification in bulk Ti-Nb alloys by single-track laser melting. *JOM*, 70(8), (2018), pp. 1589-1597.
- [38] K. Karayagiz, L. Johnson, R. Seede, V. Attari, B. Zhang, X. Huang, S. Ghosh, T. Duong, I. Karaman, A. Elwany. Finite interface dissipation phase field modeling of Ni–Nb under additive manufacturing conditions. *Acta Mater.*, 185, (2020), pp. 320-339.
- [39] J. Hunt, Cellular and primary dendrite spacings, *Solidification and Casting of Metals\ Proc. Conf.*, Sheffield, England, July 1977, 1979, pp. 3-9.
- [40] W. Kurz, D. Fisher. Dendrite growth at the limit of stability: tip radius and spacing. *Acta Metallurgica*, 29(1), (1981), pp. 11-20.
- [41] Q. Wang, C. Han, T. Choma, Q. Wei, C. Yan, B. Song, Y. Shi. Effect of Nb content on microstructure, property and in vitro apatite-forming capability of Ti-Nb alloys fabricated via selective laser melting. *Materials & Design*, 126, (2017), pp. 268-277.
- [42] P. Liu, Z. Wang, Y. Xiao, R.A. Lebensohn, Y. Liu, M.F. Horstemeyer, X. Cui, L. Chen. Integration of phase-field model and crystal plasticity for the prediction of process-structure-property relation of additively manufactured metallic materials. *International Journal of Plasticity*, 128, (2020), p. 102670.
- [43] A. Cremasco, I. Ferreira, R. Caram, Effect of heat treatments on mechanical properties and fatigue resistance of Ti-35Nb alloy used as biomaterial, *Mater. Sci. Forum*, Trans Tech Publ, 2010, pp. 68-75.
- [44] J. Wang, Y. Liu, C.D. Rabadia, S.-X. Liang, T.B. Sercombe, L.-C. Zhang. Microstructural homogeneity and mechanical behavior of a selective laser melted Ti-35Nb alloy produced from an elemental powder mixture. *Journal of Materials Science & Technology*, 61, (2021), pp. 221-233.

- [45] Y. Zhang, D. Sun, J. Cheng, J.K.H. Tsoi, J. Chen. Mechanical and biological properties of Ti–(0–25 wt%) Nb alloys for biomedical implants application. *Regenerative biomaterials*, 7(1), (2020), pp. 119-127.
- [46] L. Fikeni, K.A. Annan, K. Mutombo, R. Machaka. Effect of Nb content on the microstructure and mechanical properties of binary Ti-Nb alloys. *Materials Today: Proceedings*, 38, (2021), pp. 913-917.
- [47] J. Wang, W. Xiao, L. Ren, Y. Fu, C. Ma. The roles of oxygen content on microstructural transformation, mechanical properties and corrosion resistance of Ti-Nb-based biomedical alloys with different β stabilities. *Mater. Charact.*, 176, (2021), p. 111122.
- [48] É.S.N. Lopes, C.A.F. Salvador, D.R. Andrade, A. Cremasco, K.N. Campo, R. Caram. Microstructure, mechanical properties, and electrochemical behavior of Ti-Nb-Fe Alloys Applied as Biomaterials. *Metall. Mater. Trans. A*, 47(6), (2016), pp. 3213-3226.
- [49] J. Málek, F. Hnilica, J. Veselý, B. Smola, R. Medlín. The effect of annealing temperature on the properties of powder metallurgy processed Ti-35Nb-2Zr-0.5 O alloy. *J. Mech. Behav. Biomed. Mater.*, 75, (2017), pp. 252-261.
- [50] D. Zhao, C. Han, J. Li, J. Liu, Q. Wei. In situ fabrication of a titanium-niobium alloy with tailored microstructures, enhanced mechanical properties and biocompatibility by using selective laser melting. *Materials Science and Engineering: C*, 111, (2020), p. 110784.
- [51] B. Fu, C. Pei, H. Pan, Y. Guo, L. Fu, A. Shan. Hall-Petch relationship of interstitial-free steel with a wide grain size range processed by asymmetric rolling and subsequent annealing. *Materials Research Express*, 7(11), (2020), p. 116516.
- [52] Y. Kimura, S. Takaki. Microstructural changes during annealing of work-hardened mechanically milled metallic powders (overview). *Mater. Trans. JIM*, 36(2), (1995), pp. 289-296.
- [53] M. Yang, Y. Pan, F. Yuan, Y. Zhu, X. Wu. Back stress strengthening and strain hardening in gradient structure. *Materials Research Letters*, 4(3), (2016), pp. 145-151.

CHAPTER 5. GENERAL CONCLUSION

This study is motivated by the increasing demands in the development of high-performance Ti alloys and the knowledge gap in understanding the process-microstructure-property relationship during SLM. A nanomaterial-mediated approach was proposed to fabricate ultrahigh-strength TMNCs and crack-sensitive γ -TiAl alloys by SLM. The effects of nanomaterials on the microstructure and mechanical properties of SLM-produced TMNCs and on the manufacturability of SLM of γ -TiAl alloys were investigated. Moreover, to facilitate the development of new Ti alloys, a computational framework was developed to fundamentally investigate the process-microstructure-property relationship for SLM, with the consideration of heterogenous sub-grain structure.

In Chapter 2, nano-SiC was identified as an ideal additive for the fabrication of quasi-continuous Ti_5Si_3 reinforced TMNCs by SLM. Material characterization results indicate that nano-SiC promoted the columnar-to-equiaxed grain transition during SLM of Ti and led to significantly refined grain structure. Lamellar structured nano- Ti_5Si_3 was observed at the grain boundary, forming the desired quasi-continuous network. The formation of such microstructure was due to the grain growth restriction by nano-SiC and microsegregation of Si and eutectic reaction between Ti and segregated Si. Moreover, it was found that the nano-SiC addition presented a significantly higher effectiveness in strengthening Ti matrix, as compared to other nano-ceramics such as TiC and TiB_2 . In comparison to SLM-produced reinforcement-free sample, optimized TMNC with quasi-continuous Ti_5Si_3 network exhibits 51.5%, 62.6%, 57.2% improvements in surface hardness, effect indentation modulus and indentation yield strength, respectively, as well as 70% reduction in wear rate. The strengthening mechanism of SLM-

fabricated TMNCs was ascribed to Hall-Petch strengthening, Ti_5Si_3 -induced dislocation strengthening, Ti_5Si_3 -induced load-bearing effect, and solid solution hardening.

In Chapter 3, a facile and effective strategy that uses electrostatic attraction to decorate metal powder with tough GO sheets was developed to fabricate non-printable Ti-48Al-2Cr-2Nb alloy by SLM. It was proved that a minor amount of GO (0.1 wt.%) was sufficient to form crack-free single-tracks. Grain refinement was also achieved in this case due to the pinning effect of GO on grain growth, similar as stated in Chapter 2. The refined microstructure and alleviated laser-matter interaction both contribute to the reduced crack initiation and propagation during SLM of Ti-48Al-2Cr-2Nb. The GO addition also contributed to the enhanced strength until a saturation point was reached with 0.3 wt.% GO. The strengthening effect was ascribed to Hall-Petch mechanism, Orowan looping strengthening and increased dislocation density due to the mismatch in coefficient of thermal expansion between GO and matrix.

In Chapter 4, a multi-scale multi-physics computational framework that integrates a finite element thermal model, a phase-field grain growth model and a crystal plasticity micromechanical model was developed to investigate the process-microstructure-property relationship at the sub-grain scale for SLM of a Ti-35Nb alloy. A specific focus was put on revealing the underlying mechanism responsible for the heterogeneities in site-specific sub-grain cellular structure and associated micromechanical response. Results showed that both the sub-grain size and level of microsegregation increased at locations closer to the bottom of the melt pool, due to the increased cooling rate despite the decreased temperature gradient; however, sub-grain size showed a much more pronounced spatial variation as compared to the microsegregation. As a result, heterogeneity in micromechanical response was also observed, with the maximum material strength being near the melt pool center and the minimum being near

the melt pool boundary. In addition, in comparison to the scanning velocity, the laser power had a more significant impact on determining the heterogeneities in sub-grain cellular structure and micromechanical response in SLM of Ti-35Nb. Moreover, given a lower laser power or a higher scanning velocity, the minimum microhardness within the melt pool increased because of the reduced sub-grain size, whereas the maximum microhardness values remained the same due to the saturated strengthening effect.

In summary, the proposed nanomaterial-mediated strategy has overcome the current existing limits in fabricating quasi-continuous Ti_5Si_3 reinforced TMNCs and crack-free γ -TiAl alloys by SLM. The study has significantly advanced the knowledge on the potential roles of nanomaterials on the microstructure evolution and enhanced mechanical properties for SLM-produced parts and on the improving the manufacturability of SLM of non-printable alloys. Such strategy and acquired knowledge are expected to be applicable to other metal matrix nanocomposites or alloy systems and could provide new solutions to tackle challenges for SLM process. The established computational framework and process-microstructure-property investigations has provided important guidance in understanding the heterogeneities in site-specific sub-grain microstructure and micromechanical response, which is critical for AM process control and optimization. On basis of this, the global mechanical performance could be investigated comprehensively in the future.